Title

An investigation into the rates and processes affecting the atmospheric deposition of organic nitrates and the broader role of deposition in the NOx cycle

Permalink

https://escholarship.org/uc/item/214823wq

Author

Place, Bryan Kristopher

Publication Date

2021

An investigation into the rates and processes affecting the atmospheric deposition of organic nitrates and the broader role of deposition in the NO_x cycle

by

Bryan Kristopher Place

A dissertation submitted in partial satisfaction of the

requirements for the degree of

Doctor of Philosophy

in

Chemistry

in the

Graduate Division

of the

University of California, Berkeley

Committee in charge:

Professor Ronald Cohen, Chair
Professor Kristie Boering
Professor Inez Fung

Fall 2021

An investigation into the rates and processes affecting the atmospheric deposition of organic nitrates and the broader role of deposition in the NO_x cycle

Abstract

An investigation into the rates and processes affecting the atmospheric deposition of organic nitrates and the broader role of deposition in the NO_x cycle

by

Bryan Kristopher Place

Doctor of Philosophy in Chemistry

University of California, Berkeley

Professor Ronald Cohen, Chair

Alkyl and multifunctional nitrates ($RONO_2$) and peroxynitrates (RO_2NO_2) influence the atmosphere through their role in sequestering or recycling atmospheric NO and NO_2 (ie. NO_x). This effect modulates the production of tropospheric ozone (O_3), which has consequences for human and ecosystem health. The chemical processing of $RONO_2$, RO_2NO_2, and NO_x typically leads to the recycling of NO_x, which in most environments leads to higher ozone production. The deposition of these nitrogen oxide compounds, however, leads to the permanent loss of these compounds from the atmosphere. Recent results have indicated that nitrogen oxides can deposit rapidly from the atmosphere, but the rates, mechanisms, and properties that influence deposition are not well understood. Further, an understanding of the impact of nitrogen oxide deposition on the lifetime of nitrogen oxides as well as its role in the NO_x cycle is needed.

Laboratory chamber experiments were run using a variety of $RONO_2$ and RO_2NO_2 compounds and tree species to gain insight into the leaf-level processes driving organic nitrate deposition to vegetation. These experiments revealed that the deposition of $RONO_2$ and RO_2NO_2 occurred solely through leaf stomatal uptake. The deposition of RO_2NO_2 was found to scale linearly with stomatal conductance. The deposition of $RONO_2$ did not scale with stomatal conductance and the deposition rates differed for each $RONO_2$ compound tested. The rates of uptake observed for all $RONO_2$ and RO_2NO_2 studied were too fast to be explained through a dissolution and hydrolysis mechanism within the leaf, suggesting uptake via an alternative mechanism. Scaling the observed RO_2NO_2 deposition rates to the canopy-level indicated that the deposition of these organic nitrates from the atmosphere could compete with their thermochemical losses. Scaled canopy deposition rates for $RONO_2$ led to the conclusion that deposition was unlikely to be an important atmospheric loss of these compounds.

In parallel with these laboratory experiments, a remote sensing canopy conductance model was developed to estimate the stomatal uptake of atmospheric nitrogen oxides on a regional scale. The model was shown to accurately capture real-time canopy stomatal conductance diffusion rates across the continental United States using satellite retrievals of solar-induced fluorescence. The model was able to successfully reproduce the spatial distribution of nitrogen oxide fluxes that were estimated from leading chemical transport models. A key advantage of the canopy conductance model was its ability to capture real changes in deposition over the growing season driven by environmental factors such as drought. The canopy conductance model was used to estimate the lifetime of PAN and NO_2 over the USA and indicated that the lifetime to deposition of these compounds was shortest in heavily forested coastal regions.

Contents

List of Figures

List of Tables

Acknowledgments

I would like to thank Ronald Cohen for all his guidance and supervision throughout my time at UC Berkeley. Thank you for not only inspiring me to have confidence in my research and myself, but for also constantly reminding me of the importance of the bigger picture when conducting scientific research. I hope that we can continue to work together in the future to help push the field of atmospheric chemistry forward. I would also like to thank Paul Wooldridge for all his help and support in the completion of my PhD research. Thank you so much for all your assistance in lab and for being such a great teammate during our aircraft flux campaign.

Thank you to Dr. Richard Saykally, Dr. Daniel Neumark, Dr. Evan Williams, and Dr. Inez Fung for serving on my qualifying exam committee. Although it was one of the most stressful experiences in my life, your examination showed me that I had acquired enough skills and knowledge to critically think my way through difficult problems in the fields of physical and atmospheric chemistry. In addition, I would like to thank Dr. Kristie Boering, Dr. Inez Fung and Dr. Ron Cohen for serving on my dissertation committee. Thank you for all the feedback and questions that you raised that not only helped improve my thesis, but also gave me thoughts to ponder about for the future of some of these research investigations.

I would have never survived my PhD program if it hadn't been for all the other members of the Cohen group as well. Helen and Hannah, thanks for being such goofy office mates and gifted scientists that I could come and bother with questions at any time. Qindan, you were also such an amazing help throughout my time at UC Berkeley and a great colleague and friend. Hopefully things are peaceful enough now without me there for you to get work done. Clara, you were there for too short of a time but still were very influential in my time at Berkeley both in and outside of the office. Alex and Xiaomeng thank you both for all your research support and guidance in seeing the Gc-SIF project through to completion. And Amy thank you for all of your help with my APN deposition work. I had a blast working with you in lab and really wish we would have had a chance to work on more projects together. Alex, Helen and Hannah, I can't wait until we all meet up together again and properly celebrate Alex's new position at the University of Washington!

Thank you to Erin, and yes you get singled out, because you were that important and influential in my life during my time at UC Berkeley. Mentor, teacher, labmate, best friend, adventure buddy, running partner, and quarantine buddy are only just a few of the roles you played in my life over the last four years. Without your guidance and support, and all the shenanigans we got up to together, I truly would not have made it through this program. Truly. You were and will continue to be a very important person in my life.

Thank you so much to all the friends I made at my time at UC Berkeley. A shout out to Abdul, David, Jonathan, Josie, Jenna and Zach for all the great scientific discussions we had and at the same time distractions you gave me from day to day life. I could not have asked for better friends and a better chemistry cohort. Finally I have to thank my family for being such an unbelievable source of support throughout my entire graduate career. Thanks for being so encouraging, and really being my cheerleaders, as I pursued all of my degrees. We are so close now to being a family full of doctors!

Chapter 1

Introduction

Human-derived emissions of NO_x (NO_x = NO + NO_2) today far exceed natural and biogenic emissions of NO_x into our atmosphere. The chemistry of atmospheric NO_x leads to the formation of both toxic and phytotoxic atmospheric products. Therefore, studying the emission processes, chemical processing, and loss process of atmospheric NO_x is essential for assessing the current (and future) risk that NO_x emissions impose on human health and our ecosystem. The objectives in this first chapter of the dissertation are to i) describe the sources of NO_x to our atmosphere and discuss how they have changed over time, ii) give an overview of the chemistry of atmospheric NO_x and its role in forming air pollutants, and iii) introduce the loss process of atmospheric deposition and how it influences the NO_x cycle.

1.1 Historical perspective on atmospheric NO_x emissions

Sources of atmospheric NO_x

Before the industrial revolution, NO_x was primarily introduced into the atmosphere through bacterial processing, and lightning and wildfire events (Finlayson-Pitts and Pitts Jr., 2000; Galloway et al., 2004). Atmospheric emissions of soil NO_x from bacteria result from the intermediate production of NO during the processes of bacterial nitrification and denitrification. During nitrification (R1.1), nitrifying bacteria generate energy by oxidizing ammonia (NH_3) to nitrate (NO_3^-) through the intermediate production of hydroxylamine (NH_4OH), nitric oxide (NO) and nitrite (NO_2^-) under aerobic conditions (Pilegaard, 2013; Caranto and Lancaster, 2017). The reduction of nitrate (NO_3^-) back to N_2 by denitrfying bacteria (R1.2), primarily under anaerobic conditions, also leads to intermediate NO production and NO emissions (Pilegaard, 2013).

$$NH_3 \longrightarrow NH_2OH \longrightarrow NO \longrightarrow {NO_2}^- \longrightarrow {NO_3}^- \tag{R 1.1}$$

$$ {NO_3}^- \longrightarrow {NO_2}^- \longrightarrow NO \longrightarrow N_2O \longrightarrow N_2 \tag{R 1.2}$$

Lightning and wildfires form NO_x by generating enough energy to dissociate molecular oxygen, which can react with N_2 to form NO_x through Reactions 1.3-1.5 (Jacob, 1999). High temperatures shift the equilibria of these reactions to the right favoring NO_x formation. In addition to this formation pathway, fuel-bound nitrogen may also be released in the form of radicals during wildfire events to form NO_x (Jacob, 1999).

$$O_2 \longleftrightarrow O + O \tag{R 1.3}$$

$$O + N_2 \longleftrightarrow NO + N \tag{R 1.4}$$

$$N + O_2 \longleftrightarrow NO + O \tag{R 1.5}$$

With the advent of high temperature combustion processes, anthropogenic activity has now become the dominant source of NO_x emissions to the atmosphere (Galloway et al., 2004). These processes emit NO_x into the atmosphere by generating NO following the same thermal pathway as lightning and wildfires. Currently, the dominant global sources of anthropogenic NO_x emissions are the vehicle/transportation sectors, power generation sectors and industrial sectors (Finlayson-Pitts and Pitts Jr., 2000; Huang et al., 2017). The breakdown of source contributions to total anthropogenic NO_x emissions by region is varied. For example, in East Asia it is estimated that industrial NO_x emissions dominate the emission budget, while in North America vehicle emissions represent the largest fraction (Huang et al., 2017). Thus, controlling regional emissions of NO_x requires knowledge of the predominant sources of local emissions.

Decadal trends in anthropogenic NO_x emissions

Globally, NO_x emissions have been continuously increasing since the 1800's and are projected to increase at least until the mid 21st century (Galloway et al., 2004). In the last few decades, however, the rate of increase has slowed due to reductions in NO_x emissions in many developed nations (Huang et al., 2017). Controls on anthropogenic-derived NO_x emissions were first put in place in the USA with the Clean Air Act in 1970 (USEPA). The enactment of air quality standards was largely in response to smog events resulting from NO_x and volatile organic carbon (VOC) emissions, which led to the generation and build up of particulate matter and ozone at the surface. These events that started in the 1950's not only impacted visibility, but over time were shown to have serious consequences on human health. For example, the oxidizing ability of ozone (O_3) leads to the damaging of cells and lining fluids of airways, and has been strongly associated with asthma development and premature deaths (Lippmann, 1989; Zhang et al., 2019). Increased levels of ambient ozone has also been linked to toxicity in plants and has been shown to reduce crop yields (Hill et al.; Sandermann Jr, 1996). In addition, particulate matter has been linked to the onset of cardiovasucalar and respiratory diseases (Anderson et al., 2012). The role of NO_x in ozone and particulate matter formation is further discussed in Sect 1.2.

In response to the Clean Air Act, NO_x emissions in the USA have decreased significantly (by about a factor of 3) from 1970 to 2020 (Figure 1.2). The regulation of emissions coupled

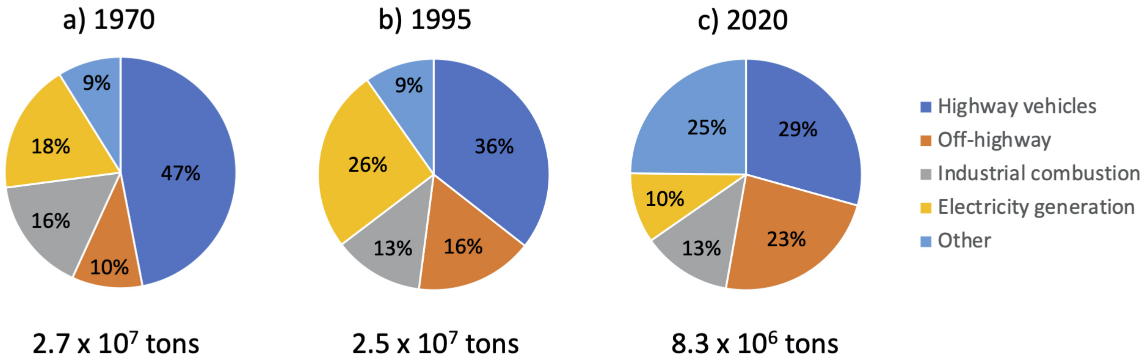

Figure 1.1: Changes in the distribution and magnitude of NO_x fluxes in the USA from 1990 to 2005 to 2020. Data sourced from the United States Environmental Protection Agency (USEPA).

with the incorporation of NO_x reducing technologies, have led to the observed decadal trend in emissions (Huang et al., 2017). The relative contribution of emissions from each sector has also changed over time in the USA (Figure 1.2). From 1970 to 1995 to 2020 there is a clear decrease in the relative contribution from highway vehicles to total emissions. This highlights the successes of improvements in catalytic converters in vehicles over time, which have been installed in vehicles to reduce NO_x emissions back to molecular oxygen and nitrogen.

1.2 The atmospheric chemistry of NO_x

The atmospheric NO_x cycle

The radical nature of both NO and NO_2 makes both of these molecules highly reactive towards other molecules in the atmosphere. This high reactivity also leads to an atmospheric lifetime for NO_x on the timescale of hours and maintains atmospheric NO_x concentrations at trace-levels in the atmosphere (on the order of parts-per-billion by volume) (Jacob, 1999). The suite of daytime photochemical reactions and processing that NO_x undergoes in the atmosphere is collectively known as the NO_x cycle and is depicted in Figure 1.2. Once NO_x has been emitted into the atmosphere it enters a rapid photochemical cycle driven by sunlight (hν) and reactive atmospheric oxidants (ie. O_3, HO_2, RO_2) that interconvert NO and NO_2 on the timescale of minutes in both urban and remote atmospheres (Jacob, 1999; Finlayson-Pitts and Pitts Jr., 2000). During this rapid cyclization process a fraction (α) of the NO and RO_2 reaction channel will go on to form an alkyl nitrates ($RONO_2$). The branching ratio (ie. α) of the NO + RO_2 reaction channel that goes on to produce an

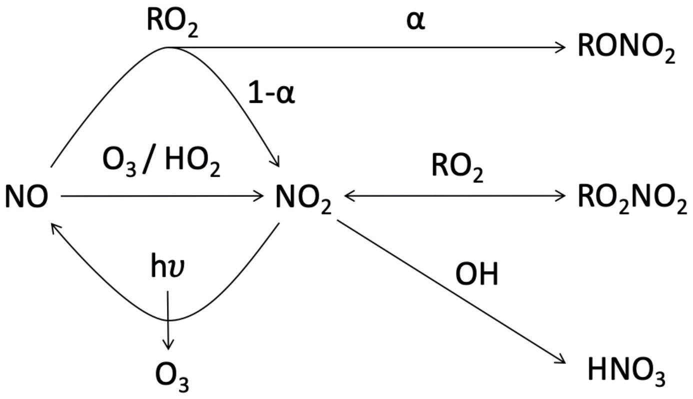

Figure 1.2: Radical propagation and termination reactions leading to the production of ozone and loss of NO_x in the troposphere.

$RONO_2$ varies between 0.1 to 40% and is largely dependent upon the identity of the R-group (Perring et al., 2013). Atmospheric RO_2 is the family of volatile organic compound (VOC) oxidation products originating from both anthropogenic and biogenic emission sources, and as such the RO_2 family consists of molecules with a wide range of functionalities (Jacob, 1999; Finlayson-Pitts and Pitts Jr., 2000). RO_2 molecules are formed through the reaction of a VOC with the hydroxyl radical (OH), which then reacts with O_2 to form RO_2 (Jacob, 1999; Finlayson-Pitts and Pitts Jr., 2000). Yields of $RONO_2$ tend to be higher between the reaction of NO with RO_2 derived from larger and more saturated molecules (Perring et al., 2013). Larger molecules have higher vibrational degrees of freedom able to stabilize the intermediate, whereas unsaturated bonds tend to weaken the peroxy bond formed in the intermediate product, leading to dissociation (O'Brien et al., 1998; Atkinson et al., 1983).

Peroxy radicals (RO_2) can also react with NO_2 to form peroxynitrates (RO_2NO_2) at similar rates to $RONO_2$ formation (Roberts, 1990). However, in the lower atmosphere most RO_2NO_2 species are unstable and thermally dissociate to reform NO_2 in seconds, with the exception of the associaton of acyl peroxy ($R(O)O_2$) radicals with NO_2 (Singh and Hanst, 1981; Roberts, 1990). Acyl peroxynitrates ($R(O)O_2NO_2$) have been shown to be thermally stable on the timescale of hours at moderate surface temperatures (Singh and Hanst, 1981; Roberts, 1990). Lastly, NO_2 can react with hydroxyl radicals (OH) in the atmopshere to form Nitric acid (HNO_3). The pathway to form HNO_3 is the dominant chemical loss pathway of NO_x in urban areas where NO_x and OH concentrations are highest and RO_2 concentrations are typically lower (Finlayson-Pitts and Pitts Jr., 2000). The formation of HNO_3 represents a permanent loss pathway of the NO_x from the atmosphere because it rapidly deposits to Earth's surface before it can react further (Finlayson-Pitts and Pitts Jr., 2000). The formation of $RONO_2$ and RO_2NO_2, however, may not lead to the permanent removal of atmospheric NO_x. The role of $RONO_2$ and RO_2NO_2 will be further discussed later in the section.

The role of NO_x in tropospheric ozone formation

As shown in Figure 1.2 the NO_x cycle leads to both the production and destruction of ozone and is the dominant factor in determining surface ozone levels. It is estimated that the reactions of NO_x with volatile organic carbons (VOCs) are responsible for a surface ozone production of 4000 Tg yr^{-1} (Jacob, 1999). Transport of ozone down from the stratosphere, on the other hand, is only estimated to contribute 800 Tg yr^{-1} of ozone to the surface budget (Jacob, 1999). The rate of ozone production generated from the NO_x cycle has a non-linear dependence on NO_x concentration and is influenced by the concentrations and reactivity of atmospheric VOCs (Figure 1.3). The non-linear dependence of ozone production on NO_x concentration is a consequence of the different fates of the OH and peroxy radicals under high-NO_x (NO_x saturated) and low-NO_x (NO_x limited) regimes (Jacob, 1999). Under NO_x saturated conditions the dominant fate of the OH radical is reaction with NO_2 (R1.6).

$$\mathrm{OH} + \mathrm{NO_2} \longrightarrow \mathrm{HNO_3} \tag{R 1.6}$$

$$\mathrm{OH} + \mathrm{R} + \mathrm{O_2} \longrightarrow \mathrm{RO_2} \tag{R 1.7}$$

$$\mathrm{RO_2} + \mathrm{RO_2} \longleftrightarrow \mathrm{ROOR} + \mathrm{O_2} \tag{R 1.8}$$

In this scenario, the production of ozone is limited by the availability of OH to generate RO_2 and HO_2 radicals. Under NO_x limited conditions, there is an abundance of peroxy radicals generated from Reaction 1.7. This abundance leads to the self-reaction of peroxy radicals instead of the participation of peroxy radicals in the NO_x cycle (R1.8). There is a balance between these two effects that lead to optimal conditions for ozone production.

Ozone production is also affected by the presence of high atmospheric concentrations of VOC's and the reactivities of VOCs towards the OH radical. Figure 1.3 shows the impact of a low VOC scenario (ie. low concentrations/reactivities of VOCs) and high VOC scenario (ie. high concentrations/reactivities of VOCs) on ozone production (Jacob, 1999). In these scenarios the shape of the curve is unchanged, however in a high VOC regime the ozone production curve will shift upward, leading to higher ozone production under similar NO_x concentrations. Figure 1.3 also highlights the importance of understanding which NO_x chemical regime a region is in and how ozone pollution may be impacted by reductions in NO_x or VOCs.

Role of organic nitrates in the NO_x cycle

Organic nitrates exert their influence on the oxidation capacity of the atmosphere by mediating the NO_x that is available to participate in chemistry. The formation of alkyl nitrates ($RONO_2$) can either lead to the permanent loss or recycling of NO_x in the atmosphere depending on the fate of the $RONO_2$ species formed (Perring et al., 2013). The fate of $RONO_2$

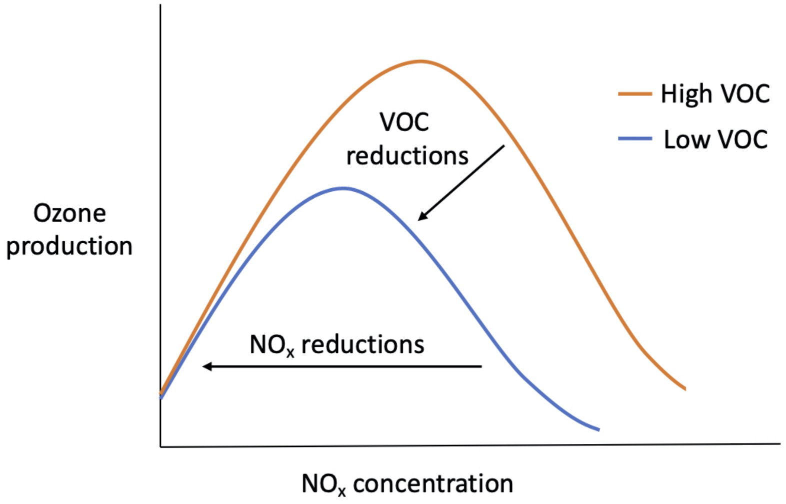

Figure 1.3: The change in ozone production as a function of NO_x concentration under a low VOC (blue trace) and high VOC (orange trace) regime.

in the atmosphere is primarily determined by its structure. Larger and more functionalized organic nitrates tend to deposit out of the atmosphere or react or partition into aerosols, leading to the removal of atmospheric NO_X (Perring et al., 2013). Recent work has also shown that tertiary nitrates (ie. nitrate group is attached to a tertiary carbon), can partition and hydrolyze quickly in aerosols, and thus be removed efficiently from the atmosphere. Smaller and less functionalized $RONO_2$ will likely undergo additional oxidation reactions before depositing out of the atmosphere (Perring et al., 2013). In this scenario, NO_x can be re-released to participate in ozone production downwind from the $RONO_2$ formation. The exact properties and processes governing the fate of atmospheric $RONO_2$, particularly with respect to its deposition to Earth's surface, still remain uncertain. The understanding of the relative loss of $RONO_2$ via particle formation is particularly important to understand, given the impact of airborne particles on human health (Sect 1.1).

Atmospheric peroxynitrates (RO_2NO_2) also act as temporary NO_x reservoirs due to their thermochemical properties (Singh and Hanst, 1981; Finlayson-Pitts and Pitts Jr., 2000). In particular, acyl peroxynitrates have been shown to transport and re-release NO_x in areas far away from source regions due to their stability in the upper atmosphere (Singh and Hanst, 1981; Fischer et al., 2014). The atmospheric fate of these species has often been assumed to depend on its thermochemical loss, however recent work has shown that they can deposit to vegetation rapidly (Sparks et al., 2003; Teklemariam and Sparks, 2004). The results from these studies imply that the deposition of acyl peroxynitrates could be competitive with thermochemical decomposition, leading to the permanent loss of atmospheric NO_x through this pathway. More studies on the depositional fate of RO_2NO_2 are needed.

1.3 Dry deposition of organic nitrates to vegetation

Model and mechanisms describing the dry deposition of trace gases

Dry deposition is the process in which gases and particles settle out of the atmosphere and either deposit to surfaces or get absorbed by plant tissues. Within the atmospheric community, the dry deposition of trace gases is most commonly described using the Wesely resistance model (Baldocchi et al., 1987; Wesely, 1989). The Wesely model describes the deposition rate of a trace gas through a set of 'resistances', or inverses of rates, that occur either in series or in parallel. Figure 1.4 outlines the deposition pathways for a trace gas (X) depositing to vegetation following the Wesely model.

The deposition of a trace gas (X) first undergoes aerodynamic transport (R_a) through the atmosphere to the stagnant air (or quasi-laminar sublayer) adjacent to the depositing surface (Figure 1.4). The deposition of the trace gas then proceeds through molecular diffusion of the gas (R_b) through the quasi-laminar sublayer formed at the leaf/branch surface. Once through the sublayer, the gas (X) can deposit to branch/cuticle surfaces (R_c), diffuse through leaf stomata (R_s) and be processed within the leaf mesophyll (R_m), or the deposition of X can proceed through a combination of both these pathways. In the case of deposition to a non-vegetation, deposition will only proceed through the R_c pathway. Using Figure 1.4 the total deposition rate, described as a deposition velocity (V_d), for trace gas X to vegetation can then be represented through Equation 1.1.

$$V_d(X) = \frac{1}{R_a + R_b + (\frac{1}{R_c} + \frac{1}{R_s+R_m})^{-1}} \tag{1.1}$$

During the daytime when aerodynamic transport is fast and the quasi-laminar layer is disturbed, R_a and R_b do not typically limit the deposition of a trace gas, and thus surface uptake is the rate limiting step in deposition. Trace gases with high solubilities or high tendencies to react with surface components deposit to surfaces at fast rates (Wesely, 1989; Hill, 1971). For example, Nitric acid (HNO_3) has a very high solubility ($H > 10^5$ M atm^{-1}), and has been shown to readily 'stick' on plant surfaces, leading to fast rates of deposition (Wesely, 1989; Sander, 2015). Ozone, which has a high reactivity, has also been shown to deposit to vegetation surfaces at high rates (Wesely, 1989). Due to its high reactivity it is also processed quickly in the leaf mesophyll and it is estimated that the R_c and $R_s + R_m$ pathways contribute equally to its deposition rate (Clifton et al., 2020). In cases where the solubility and reactivity of a trace gas is low, deposition may be slow and is likely limited by the leaf mesophyll processing rate (R_m). Nitric oxide (NO) is an example of a trace gas

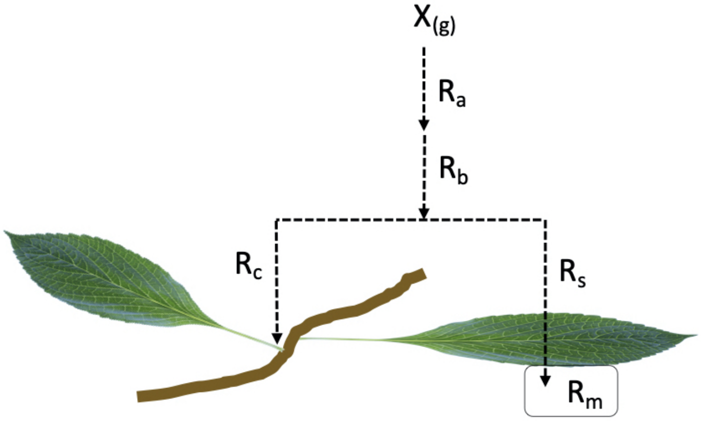

Figure 1.4: Pathways of deposition of trace gas (X) to vegetation described through the Wesely resistance model.

with a low solubility, low reactivity and as a result has a very low deposition rate (ie. low mesophyll rate) (Wesely, 1989).

Dry deposition of NO_x, $RONO_2$, and RO_2NO_2 to vegetation

The current understanding of NO_x deposition is that all deposition occurs via NO_2 and that NO_2 deposition mainly proceeds through a stomatal pathway (Chaparro-Suarez et al., 2011; Breuninger et al., 2012; Delaria et al., 2018, 2020). In general, the deposition rates reported by these studies scaled directly with stomatal conductance, however Breuninger et al. (2012) reported lower rates and attributed it to mesophyllic resistance. Emissions of NO_x at low ambient concentrations have also been reported previously (Gessler et al., 2000; Sparks et al., 2001; Hereid and Monson, 2001). Delaria et al. (2020) conducted the most comprehensive NO_x deposition study to date and found that NO_2 deposition to ten tree species scaled directly with stomatal conductance, with minimal contribution from the mesophylic rate. The authors of this study found no evidence of NO_2 emission (Delaria et al., 2020). The deposition rates implied by the studies that observed NO_x deposition scaling directly with stomatal conductance, suggest that deposition can account for up to 20% of the NO_x loss in a forest canopy (Delaria et al., 2018).

Fewer studies to date have investigated the atmospheric removal of $RONO_2$ and RO_2NO_2 through deposition. In a study by Lockwood et al (2008), the deposition of $RONO_2$ to Quaking aspen leaves was studied by dosing the tree leaves with high concentrations of methylbutyl nitrate (Lockwood et al., 2008). From these experiments, it was determined that all methylbutyl nitrate deposition occurred through stomatal uptake and that the mesophylic rate (R_m) was rate-limiting. From the average uptake rate measured in this study the authors proposed that hydrolysis initiated reactions in the leaf mesophyl could be responsible for the observed levels of deposition. Nighttime measurements of C_1-C_5 alkyl nitrates in Colorado and New Hampshire revealed moderate nighttime deposition velocities for these compounds (Russo et al., 2010; Abeleira et al., 2018). These deposition velocities were attributed to uptake on tree/soil surfaces, since leaf stomata are typically closed at night. Measurements of multifunctional alkyl nitrates during the Southern Oxidant and Aerosol Study have shown that highly functionalized nitrates deposit rapidly from the atmosphere, at similar rates as nitric acid (Nguyen et al., 2015). Leaf-level studies investigating RO_2NO_2 deposition have found that deposition scales with leaf stomatal conductance, and that R_m begins to limit the deposition rate at high levels of stomatal conductance (Sparks et al., 2003; Teklemariam and Sparks, 2004; Sun et al., 2016a,b). Sparks et al. (2003) also presented evidence that R_m may vary between coniferous trees, deciduous trees and crops. The deposition of RO_2NO_2 to cuticular surfaces has also been reported as a minor pathway, but still remains under debate (Sun et al., 2016a). All leaf-level deposition measurements to date have only studied the deposition of peroxyacetyl nitrate (PAN) to vegetation. The deposition of speciated RO_2NO and ΣRO_2NO_2 has been studied at the canopy-level as well (Farmer et al., 2006; Wolfe et al., 2009; Min et al., 2012). The fluxes measured from these studies were consistent with a stomatal uptake pathway of RO_2NO_2. The stomatal uptake of PAN was estimated to represent up to 50% of the PAN loss in a forest canopy by Wolfe et al. (2009). In the same study the deposition fluxes of PAN and peroxypropionic nitrate (PPN) had different rates, implying there could be differences in deposition between these RO_2NO_2. These past studies highlight the need for studying the deposition rates and processes for a range of $RONO_2$ and RO_2NO_2 compounds.

1.4 Dissertation objectives

Chapter 2: A study on the deposition of acyl peroxynitrates to trees

The objective of this chapter was to gain more insight into the process of acyl peroxynitrate deposition to vegetation and understand the role deposition plays as an atmospheric loss of peroxynitrates. The study presented in this chapter was designed to address the following research questions: 1) What are the rates and mechanisms that govern acyl peroxynitrate deposition to trees? 2) What factors (eg. biological, environmental) influence the deposition rates and processes? and 3) Do the rates measured in the study imply that the deposition of peroxynitrates will be a competitive atmospheric loss process?

Chapter 3: A study on the deposition of alkyl nitrates to trees

The objective of this chapter was to probe the underlying processes that influence the deposition of different alkyl nitrate species to vegetation. The study was designed to address the following research questions: 1) What are the rates and mechanisms that govern short-chain alkyl nitrate deposition to trees? 2) What alkyl nitrate properties drive the deposition to trees? and 3) Is the deposition of alkyl nitrates competitive with the atmospheric chemical losses of these species?

Chapter 4: Estimating regional NO_x and PAN deposition using a canopy conductance model

The objective of this chapter was to extend laboratory measurements of NO_x and PAN deposition to estimate deposition on a regional scale across the continental USA. The study was designed to address the following research questions: 1) Can we develop a model to estimate the deposition of nitrogen oxides on a large spatial scale? 2) Will this model accurately reflect the understanding of deposition gleaned from laboratory measurements 3) How will this model compare to other estimates of deposition from large-scale models? and 4) Can the model be used to learn more about the atmospheric fate of nitrogen oxides?

1.5 References

Abeleira, A., Sive, B., Swarthout, R. F., Fischer, E. V., Zhou, Y., and Farmer, D. K.: Seasonality, sources and sinks of C1–C5 alkyl nitrates in the Colorado Front Range, Elementa: Science of the Anthropocene, 6, https://doi.org/10.1525/elementa.299, URL https://doi.org/10.1525/elementa.299, 45, 2018.

Anderson, J. O., Thundiyil, J. G., and Stolbach, A.: Clearing the air: A review of the effects of particulate matter air pollution on human health, Journal of Medical Toxicology, 8, 166–175, https://doi.org/10.1007/s13181-011-0203-1, 2012.

Atkinson, R., Carter, W. P. L., and Winer, A. M.: Effects of temperature and pressure on alkyl nitrate yields in the nitrogen oxide (NOx) photooxidations of n-pentane and n-heptane, The Journal of Physical Chemistry, 87, 2012–2018, https://doi.org/10.1021/j100234a034, URL https://doi.org/10.1021/j100234a034, 1983.

Baldocchi, D. D., Hicks, B. B., and Camara, P.: A canopy stomatal resistance model for gaseous deposition to vegetated surfaces, Atmospheric Environment (1967), 21, 91–101, https://doi.org/https://doi.org/10.1016/0004-6981(87)90274-5, URL https://www.sciencedirect.com/science/article/pii/0004698187902745, 1987.

Breuninger, C., Oswald, R., Kesselmeier, J., and Meixner, F. X.: The dynamic chamber method: trace gas exchange fluxes (NO, NO_2, O_3) between plants and the atmosphere in the laboratory and in the field, Atmospheric Measurement Techniques, 5, 955–989, https://doi.org/10.5194/amt-5-955-2012, URL https://amt.copernicus.org/articles/5/955/2012/, 2012.

Caranto, J. D. and Lancaster, K. M.: Nitric oxide is an obligate bacterial nitrification intermediate produced by hydroxylamine oxidoreductase, Proceedings of the National Academy of Sciences, 114, 8217–8222, https://doi.org/10.1073/pnas.1704504114, URL https://www.pnas.org/content/114/31/8217, 2017.

Chaparro-Suarez, I., Meixner, F., and Kesselmeier, J.: Nitrogen dioxide (NO2) uptake by vegetation controlled by atmospheric concentrations and plant stomatal aperture, Atmospheric Environment, 45, 5742 – 5750, https://doi.org/https://doi.org/10.1016/j.atmosenv.2011.07.021, URL http://www.sciencedirect.com/science/article/pii/S1352231011007461, 2011.

Clifton, O. E., Paulot, F., Fiore, A. M., Horowitz, L. W., Correa, G., Baublitz, C. B., Fares, S., Goded, I., Goldstein, A. H., Gruening, C., Hogg, A. J., Loubet, B., Mammarella, I., Munger, J. W., Neil, L., Stella, P., Uddling, J., Vesala, T., and Weng, E.: Influence of Dynamic Ozone Dry Deposition on Ozone Pollution, Journal of Geophysical Research: Atmospheres, 125, e2020JD032 398, https://doi.org/https://doi.org/10.1029/2020JD032398, URL https://agupubs.onlinelibrary.wiley.com/doi/abs/10.1029/2020JD032398, e2020JD032398 10.1029/2020JD032398, 2020.

Delaria, E. R., Vieira, M., Cremieux, J., and Cohen, R. C.: Measurements of NO and NO_2 exchange between the atmosphere and *Quercus agrifolia*, Atmospheric Chemistry and Physics, 18, 14 161–14 173, https://doi.org/10.5194/acp-18-14161-2018, URL https://acp.copernicus.org/articles/18/14161/2018/, 2018.

Delaria, E. R., Place, B. K., Liu, A. X., and Cohen, R. C.: Laboratory measurements of stomatal NO_2 deposition to native California trees and the role of forests in the NO_x cycle, Atmospheric Chemistry and Physics, 20, 14 023–14 041, https://doi.org/10.5194/acp-20-14023-2020, URL https://acp.copernicus.org/articles/20/14023/2020/, 2020.

Farmer, D. K., Wooldridge, P. J., and Cohen, R. C.: Application of thermal-dissociation laser induced fluorescence (TD-LIF) to measurement of HNO_3, Sigma;alkyl nitrates, Sigma;peroxy nitrates, and NO_2 fluxes using eddy covariance, Atmospheric Chemistry and Physics, 6, 3471–3486, https://doi.org/10.5194/acp-6-3471-2006, URL https://acp.copernicus.org/articles/6/3471/2006/, 2006.

Finlayson-Pitts, B. J. and Pitts Jr., J. N.: Chemistry of the Upper and Lower Atmosphere, Academic Press, 2000.

Fischer, E. V., Jacob, D. J., Yantosca, R. M., Sulprizio, M. P., Millet, D. B., Mao, J., Paulot, F., Singh, H. B., Roiger, A., Ries, L., Talbot, R. W., Dzepina, K., and Pandey Deolal, S.: Atmospheric peroxyacetyl nitrate (PAN): a global budget and source attribution, Atmospheric Chemistry and Physics, 14, 2679–2698, https://doi.org/10.5194/acp-14-2679-2014, URL https://acp.copernicus.org/articles/14/2679/2014/, 2014.

Galloway, D. J., Dentener, F. J., Capone, D. G., Boyer, E. W., Howarth, R. W., Seitzinger, S. P., Asner, G. P., Cleveland, C. C., Green, P. A., Holland, E. A., Karl, D. M., Michaels, A. F., Porter, J. H., Townsend, A. R., and Voosmarty, C. J.: Nitrogen cycles: Past, present, and future, Biogeochemistry, 70, 153–226, https://doi.org/10.1007/s10533-004-0370-0, 2004.

Gessler, A., Rienks, M., and Rennenberg, H.: NH3 and NO2 fluxes between beech trees and the atmosphere – correlation with climatic and physiological parameters, New Phytologist, 147, 539–560, https://doi.org/10.1046/j.1469-8137.2000.00712.x, 2000.

Hereid, D. and Monson, R.: Nitrogen Oxide Fluxes between Corn (Zea mays L.) Leaves and the Atmosphere, Atmospheric Environment, 35, 975–983, https://doi.org/10.1016/S1352-2310(00)00342-3, 2001.

Hill, A. C.: Vegetation: A Sink for Atmospheric Pollutants, Journal of the Air Pollution Control Association, 21, 341–346, https://doi.org/10.1080/00022470.1971.10469535, URL https://doi.org/10.1080/00022470.1971.10469535, 1971.

Hill, A. C., Pack, M. R., Treshow, M., Downs, R. J., and Transtrum, L. G.: Plant injury induced by ozone, Phytopathology; (United States), URL https://www.osti.gov/biblio/5518148.

Huang, T., Zhu, X., Zhong, Q., Yun, X., Meng, W., Li, B., Ma, J., Zeng, E. Y., and Tao, S.: Spatial and Temporal Trends in Global Emissions of Nitrogen Oxides from 1960 to 2014, Environmental Science & Technology, 51, 7992–8000, https://doi.org/10.1021/acs.est.7b02235, URL https://doi.org/10.1021/acs.est.7b02235, pMID: 28613845, 2017.

Jacob, D. J.: Introduction to Atmospheric Chemistry, Princeton University Press, 1999.

Lippmann, M.: Health effects of ozone a critical Review, JAPCA, 39, 672–695, https://doi.org/10.1080/08940630.1989.10466554, URL https://doi.org/10.1080/08940630.1989.10466554, pMID: 2659744, 1989.

Lockwood, A. L., Filley, T. R., Rhodes, D., and Shepson, P. B.: Foliar uptake of atmospheric organic nitrates, Geophysical Research Letters, 35, https://doi.org/https://doi.org/10.1029/2008GL034714, URL https://agupubs.onlinelibrary.wiley.com/doi/abs/10.1029/2008GL034714, 2008.

Min, K.-E., Pusede, S. E., Browne, E. C., LaFranchi, B. W., Wooldridge, P. J., Wolfe, G. M., Harrold, S. A., Thornton, J. A., and Cohen, R. C.: Observations of atmosphere-biosphere exchange of total and speciated peroxynitrates: nitrogen fluxes and biogenic sources of peroxynitrates, Atmospheric Chemistry and Physics, 12, 9763–9773, https://doi.org/10.5194/acp-12-9763-2012, URL https://acp.copernicus.org/articles/12/9763/2012/, 2012.

Nguyen, T. B., Crounse, J. D., Teng, A. P., St. Clair, J. M., Paulot, F., Wolfe, G. M., and Wennberg, P. O.: Rapid deposition of oxidized biogenic compounds to a temperate forest, Proceedings of the National Academy of Sciences, 112, E392–E401, https://doi.org/10.1073/pnas.1418702112, URL https://www.pnas.org/content/112/5/E392, 2015.

O'Brien, J. M., Czuba, E., Hastie, D. R., Francisco, J. S., and Shepson, P. B.: Determination of the Hydroxy Nitrate Yields from the Reaction of C2C6 Alkenes with OH in the Presence of NO, The Journal of Physical Chemistry A, 102, 8903–8908, https://doi.org/10.1021/jp982320z, URL https://doi.org/10.1021/jp982320z, 1998.

Perring, A. E., Pusede, S. E., and Cohen, R. C.: An observational perspective on the atmospheric impacts of alkyl and multifunctional nitrates on ozone and secondary organic aerosol, Chemical Reviews, 10, 5848–5870, https://doi.org/10.1021/cr300520x, 2013.

Pilegaard, K.: Processes regulating nitrix oxide emissions from soils, Philosophical Transactions of The Royal Society B, 368, 1621, https://doi.org/10.1098/rstb.2013.0126, 2013.

Roberts, J. M.: The atmospheric chemistry of organic nitrates, Atmospheric Environment. Part A. General Topics, 24, 243–287, https://doi.org/https://doi.org/10.1016/0960-1686(90)90108-Y, URL https://www.sciencedirect.com/science/article/pii/096016869090108Y, 1990.

Russo, R. S., Zhou, Y., Haase, K. B., Wingenter, O. W., Frinak, E. K., Mao, H., Talbot, R. W., and Sive, B. C.: Temporal variability, sources, and sinks of C_1-C_5 alkyl nitrates in coastal New England, Atmospheric Chemistry and Physics, 10, 1865–1883, https://doi.org/10.5194/acp-10-1865-2010, URL https://acp.copernicus.org/articles/10/1865/2010/, 2010.

Sander, R.: Compilation of Henry's law constants (version 4.0) for water as solvent, Atmospheric Chemistry and Physics, 15, 4399–4981, https://doi.org/10.5194/acp-15-4399-2015, URL https://acp.copernicus.org/articles/15/4399/2015/, 2015.

Sandermann Jr, H.: Ozone and plant health, Annual Review of Phytopathology, 34, 347–366, https://doi.org/10.1146/annurev.phyto.34.1.347, URL https://doi.org/10.1146/annurev.phyto.34.1.347, pMID: 15012547, 1996.

Singh, H. B. and Hanst, P. L.: Peroxyacetyl nitrate (PAN) in the unpolluted atmosphere: An important reservoir for nitrogen oxides, , 8, 941–944, https://doi.org/10.1029/GL008i008p00941, 1981.

Sparks, J., Monson, R., Sparks, K., and Lerdau, M.: Leaf uptake of nitrogen dioxide (NO2) in a tropical wet forest: Implications for tropospheric chemistry, Oecologia, 127, 214–221, https://doi.org/10.1007/s004420000594, 2001.

Sparks, J. P., Roberts, J. M., and Monson, R. K.: The uptake of gaseous organic nitrogen by leaves: A significant global nitrogen transfer process, Geophysical Research Letters, 30, https://doi.org/https://doi.org/10.1029/2003GL018578, URL https://agupubs.onlinelibrary.wiley.com/doi/abs/10.1029/2003GL018578, 2003.

Sun, S., Moravek, A., Trebs, I., Kesselmeier, J., and Sörgel, M.: Investigation of the influence of liquid surface films on O3 and PAN deposition to plant leaves coated with organic/inorganic solution, Journal of Geophysical Research: Atmospheres, 121, 14,239–14,256, https://doi.org/https://doi.org/10.1002/2016JD025519, URL https://agupubs.onlinelibrary.wiley.com/doi/abs/10.1002/2016JD025519, 2016a.

Sun, S., Moravek, A., von der Heyden, L., Held, A., Sörgel, M., and Kesselmeier, J.: Twin-cuvette measurement technique for investigation of dry deposition of O_3 and PAN to plant leaves under controlled humidity conditions, Atmospheric Measurement Techniques, 9, 599–617, https://doi.org/10.5194/amt-9-599-2016, URL https://amt.copernicus.org/articles/9/599/2016/, 2016b.

Teklemariam, T. A. and Sparks, J. P.: Gaseous fluxes of peroxyacetyl nitrate (PAN) into plant leaves, Plant, Cell & Environment, 27, 1149–1158, https://doi.org/https://doi.org/10.1111/j.1365-3040.2004.01220.x, URL https://onlinelibrary.wiley.com/doi/abs/10.1111/j.1365-3040.2004.01220.x, 2004.

USEPA: Overview of the Clean Air Act and Air Pollution, URL https://www.epa.gov/clean-air-act-overview.

Wesely, M.: Parameterization of surface resistances to gaseous dry deposition in regional-scale numerical models, Atmospheric Environment, 23, 1293–1304, https://doi.org/10.1016/0004-6981(89)90153-4, 1989.

Wolfe, G. M., Thornton, J. A., Yatavelli, R. L. N., McKay, M., Goldstein, A. H., LaFranchi, B., Min, K.-E., and Cohen, R. C.: Eddy covariance fluxes of acyl peroxy nitrates (PAN, PPN and MPAN) above a Ponderosa pine forest, Atmospheric Chemistry and Physics, 9, 615–634, https://doi.org/10.5194/acp-9-615-2009, URL https://acp.copernicus.org/articles/9/615/2009/, 2009.

Zhang, J. J., Wei, Y., and Fang, Z.: Ozone Pollution: A Major Health Hazard Worldwide, Frontiers in Immunology, 10, 2518, https://doi.org/10.3389/fimmu.2019.02518, URL https://www.frontiersin.org/article/10.3389/fimmu.2019.02518, 2019.

Chapter 2

Leaf stomatal control of acyl peroxynitrate deposition

Adapted from B. K. Place et al., Leaf stomatal control over acyl peroxynitrate dry deposition to trees, *ACS Earth Space Chem.*, 4, 2162—2170, https://dx.doi.org/10.1021/acsearthspacechem.0c00152, 2020.

2.1 Abstract

Acyl peroxynitrates are formed in the atmosphere through the oxidation of NO_x and are treated as temporary NO_x sinks because they typically decompose to re-release NO_x on the timescale of a few hours. Canopy and leaf level measurements of acyl peroxynitrate deposition to vegetation, however, have revealed that this removal process is rapid and may compete with chemical decomposition. In an effort to learn more about the dry deposition of acyl peroxynitrates we designed experiments to measure the deposition of peroxyacetyl nitrate and peroxypropionic nitrate to ten California-native tree species. The deposition of these two organic nitrate compounds was driven by leaf stomatal uptake. No surface deposition of either nitrate was observed. Maximum deposition velocities ranged from 0.09 – 0.3 cm s^{-1}, and correlated strongly with maximum leaf stomatal conductance. The stomatal-uptake of peroxyacetyl nitrate and peroxypropionic nitrate scaled with factors of 0.73 + 0.03 and 0.95 + 0.07, respectively, of the stomatal limit independent of water and nitrogen status of the trees. These measurements suggest that the uptake of acyl peroxynitrates by leaf stomata can be a dominant loss process in areas of high tree cover and moderate temperature.

2.2 Introduction

The distribution of tropospheric nitrogen oxides affects the oxidative capacity of the atmosphere, and abundances of ozone and aerosol. Nitrogen oxides are introduced into the atmosphere through emissions of NO_x ($NO_x = NO + NO_2$) and are typically oxidized to HNO_3 and deposited within 100 km of the emission source (Finlayson-Pitts and Pitts Jr., 2000). However a small fraction of urban emissions and a large fraction of rural emissions react to form acyl peroxynitrates (APNs = $R(O)O_2NO_2$) and alkyl- and multifunctional nitrates (ANs = $RONO_2$) (Finlayson-Pitts and Pitts Jr., 2000; Perring et al., 2013; Fischer et al., 2014). Under warm conditions, APNs are in steady state with NO_2, effectively acting as a buffer to the amount of NO_x available for chemistry (Singh and Hanst, 1981; Roberts and Bertman, 1992; Romer et al., 2016). At lower temperatures, APNs are thermally stable and their lifetime becomes decoupled from NO_x. This thermochemical property of APNs allows them to be transported long distances and act as a new source of nitrogen oxides to remote regions (Moxim et al., 1996; Fischer et al., 2014). Upon oxidation, ANs produce either HNO_3 or NO_x, depending on the identity of attached R-group (Darer et al., 2011; Perring et al., 2013; Lee et al., 2014; Romer et al., 2016). These chemical pathways affecting APNs and ANs can lead to the recycling of NO_x. In contrast, the dry deposition of these organic nitrates to the earth's surface, is a permanent loss of NO_x, and may be an important pathway for NO_x removal from the atmosphere.

Delaria et al. recently described laboratory observations and canopy scale modeling of the role that deposition to trees plays in the lifetime of NO_x (Delaria et al., 2018; Delaria and Cohen, 2020; Delaria et al., 2020). They show that NO_2 uptake to the forest ecosystems explored is nearly exclusively through leaf stomata with deposition to surfaces unmeasureably small. This deposition is sufficient to provide a mechanistic explanation for the ad hoc canopy reduction factor commonly employed to remove soil NO_x emissions within a plant canopy (Yienger and Levy, 1995; Hudman et al., 2012). The deposition rate of NO_2 was estimated to be on the order 10% of the total removal rate of NO_x over forests (Delaria and Cohen, 2020). Since APNs are coupled to NO_x, a full accounting of the factors affecting the distribution and lifetime of NO_x must include a description of the lifetime of APNs with respect to deposition.

Canopy-level measurements of APN fluxes indicate that APNs are removed from the atmosphere rapidly in forests (Farmer et al., 2006; Turnipseed et al., 2006; Wolfe et al., 2009; Min et al., 2012). The convolution of multiple in-canopy loss processes, however, has made it difficult to ascribe the fluxes observed in the field to specific processes such as surface deposition, stomatal uptake, and thermochemical decomposition. Leaf-level studies investigating peroxyacetyl nitrate (PAN) deposition to vegetation have found that deposition occurs primarily through stomatal uptake and at rates sufficiently large to explain canopy-level observations (Sparks et al., 2003; Teklemariam and Sparks, 2004; Sun et al., 2016a,b). However, the roles of both the leaf mesophyllic rate and cuticle deposition rate in PAN deposition are less well constrained by measurements (Sparks et al., 2003; Teklemariam and Sparks, 2004; Sun et al., 2016a,b). Sparks et al. (2003) observed no cuticular deposition of PAN to select trees and crops and found that the mesophyllic rates differed by vegetation type and contributed to overall deposition only at higher levels of stomatal opening (Sparks et al., 2003). Leaf-level studies of PAN deposition to *Quercus ilex* conducted by Sun et al. (2016a,b) suggested that non-stomatal deposition can account for up to 20% of the total PAN deposition and found a constant mesophyllic rate across all measurements (Sun et al., 2016a,b). More studies looking at leaf-level APN deposition to trees are needed to provide a complete understanding of the mechanisms and rates governing this process.

Here we describe laboratory observations of the deposition of peroxyacetyl nitrate (PAN) and peroxypropionic nitrate (PPN) to a series of California trees, assessing the role of surfaces, stomata, nutrient and water status and evaluating whether there is a leaf mesophyll component influencing the uptake of APNs. We conclude with a discussion of the implications of our branch-level APN deposition rates for larger canopy scales.

2.3 Materials and methods

A detailed description of the instruments and methods used in these experiments can be found in Delaria et al. (2018) and (2020). A brief summary is given below.

2.3.1 California-native tree species and growth conditions

Tree saplings of coast redwood (*Sequoia sempervirens*), blue oak (*Quercus douglasii*), coast live oak (*Quercus agrifolia*) bigleaf maple (*Acer macrophyllum*), Pacific madrone (*Arbutus menziesii*), ponderosa pine (*Pinus ponderosa*), Douglas fir (*Pseudotsuga menziesii*), lodgepole pine (*Pinus contorta*), incense cedar (*Calocedrus decurrens*), and digger pine (*Pinus sabiniana*) were purchased from Native Here Nursery (Berkeley, CA) or forestfarm at Pacifica (Williams, OR). Trees were re-potted in 20 − 40L pots with a commercial mixture of fertilized soil (Sun Gro Sunshine 4 and Supersoil), and were grown outside in a lath house at the Oxford Facility in Berkeley, CA. All trees were watered daily except for individuals of the tree species used to carry out the drought-stress and nitrogen fertilization studies (see Section 2.3.4). Descriptions of the tree species and a list of the regions where each tree species can be found in California are noted in Table 2.A1. Detailed maps showing the tree counts in California for each species can be found in Delaria et al. (2020).

2.3.2 PAN and PPN synthesis

Peroxyacetyl nitrate (PAN) and peroxypropionic nitrate (PPN) were synthesized in real-time via the photolysis of excess acetone or 3-pentanone, respectively, in the presence of O_2 and NO_2 (R2.1 and R2.2) (Furgeson et al., 2011; Rider et al., 2015).

$$\mathrm{CH_3COCH_3} + \mathrm{h}\nu(\lambda{=}\,275\,\mathrm{nm}) \longrightarrow \mathrm{CH_3CO} + \mathrm{NO_2} + \mathrm{O_2} \longrightarrow \mathrm{CH_3C(O)O_2NO_2} \quad (\mathrm{R\,2.1})$$

$$\mathrm{C_2H_5COC_2H_5} + \mathrm{h}\nu(\lambda{=}\,275\,\mathrm{nm}) \longrightarrow \mathrm{C_2H_5CO} + \mathrm{NO_2} + \mathrm{O_2} \longrightarrow \mathrm{C_2H_5C(O)O_2NO_2} \quad (\mathrm{R\,2.2})$$

The APN photolysis source consisted of a ketone diffusion tube and a photolysis chamber (Figure 2.1a). The diffusion tube used to facilitate acetone diffusion was made from a piece of PFA tubing (5 cm, 1/4”) with a small PFA tubing insert (1 cm, 1/8”) placed inside to

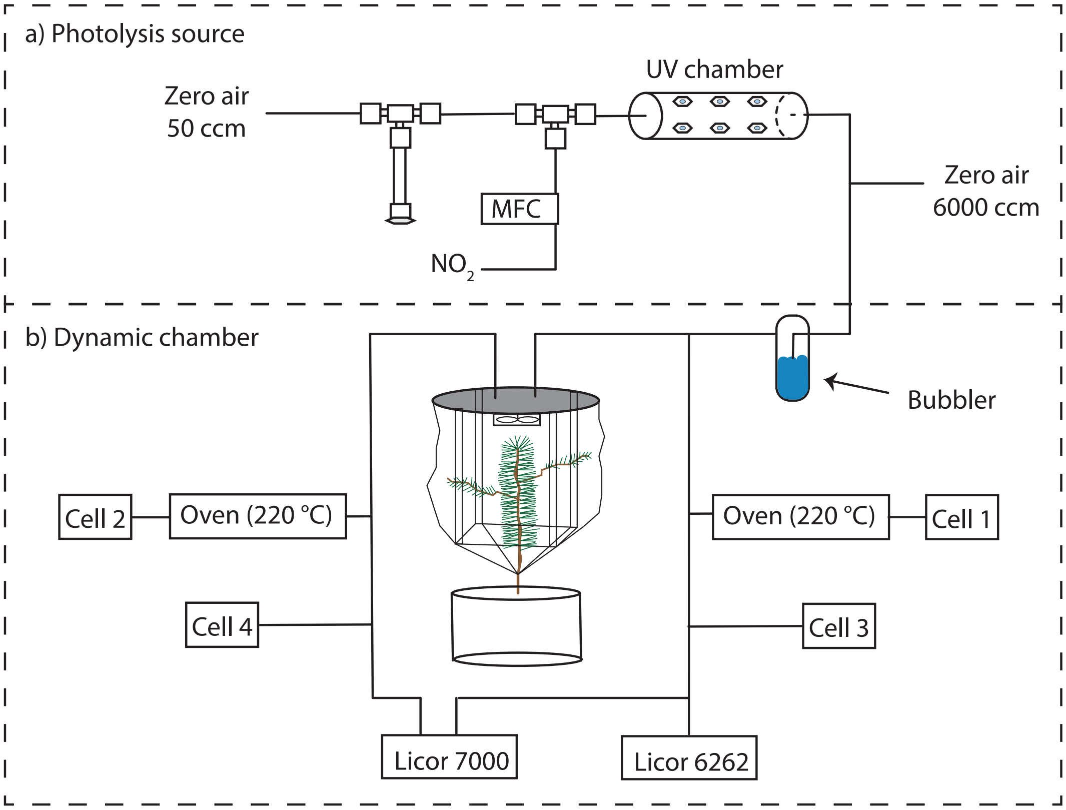

Figure 2.1: Illustration of a) the photolysis source used to synthesize PAN and PPN and b) the dynamic chamber setup for determining the branch-level peroxynitrate deposition to trees. Gas-phase peroxynitrates were monitored using TD-LIF in cells 1 and 2, and NO_2 concentrations were monitored with LIF in cells 3 and 4 throughout an experiment. Two Licor instruments were used to measure ingoing and outgoing CO_2 and H_2O concentrations.

limit the acetone diffusion rate. The 3-pentanone diffusion tube was made from a single piece of PFA tubing (4 cm, 1/4"). Approximately 1-2 ml of the desired ketone ($> 99.9\%$ purity, Sigma Aldrich) was placed in a Teflon cap at the bottom of the tube before each experiment was run. A 50 ± 5 ccm flow of zero air (room air scrubbed of reactive gases and H_2O) was used to carry the volatilized ketone towards the photolysis chamber. Before the gaseous ketone reached the chamber it was mixed with a set flow (1 – 7 ccm) of NO_2 ($\approx$5ppmv, Praxair), resulting in NO_2 ambient mixing ratios between 100 and 700 parts per billion by volume (ppbv). The cylindrical photolysis chamber was constructed out of fused quartz tubes and 6 UVC-LEDs ($\lambda = 275 \pm 10$ nm) were installed equidistantly around the chamber. The total volume of the photolysis chamber was 330 cm^3, giving a gas residence time of $\approx$6 minutes at a flow of 50 ccm.

The experimental yield of both PAN and PPN under these conditions was approximately 90-95% for NO_2 mixing ratios in the range of 100 - 700 ppbv. Typically, $\approx$5% of NO_2

remained unreacted, and ≈5% was converted into ANs and HNO_3. The presence of these higher nitrogen oxide species was confirmed via thermal dissociation and NO_2 detection (see Section 2.3.3 for more details). Unreacted NO_2 was corrected for during flux measurements. Upon exiting the photolysis chamber, the flow was diluted with a flow of 6500 ccm zero air to give final APN mixing ratios between 0.5 and 7 ppbv.

2.3.3 Branch-level peroxynitrate deposition experiments

Deposition experiments were conducted by dosing a tree sapling branch enclosed in a 10L Teflon bag with a humidified flow containing PAN or PPN (Figure 2.1b). A typical experiment consisted of stepping through 8 – 10 mixing ratios of an APN (0 – 7 ppbv), with an equilibration time of 40 minutes at each concentration. The total flow of APN into the chamber ranged from 5000 - 5200 ccm resulting in a chamber residence time of approximately 2 minutes. For simulated daylight, an LED diode array (Apollo horticulture) was used to provide photosynthetically active radiation with a photon flux set to 1200 μmol m^{-2} s^{-1}. Ingoing water vapor pressure was varied between 0 and 1.7 kPa using an in-line glass bubbler filled with deionized water and was maintained within ± 0.1kPa during a given experiment. Chamber temperatures were monitored using a thermocouple and fell within the range of 20 ± 3 °C, with a variability of ± 2 °C in a single experiment. Gaseous PAN and PPN concentrations at the inlet and outlet of the chamber were measured by thermal dissociation to NO_2 followed by laser-induced fluorescence (LIF) detection of the product NO_2 molecules (Day et al., 2002). The product NO_2 molecules were excited with a diode laser (Z-Laser ZM183H, λ = 405 nm), and the resulting red-shifted fluorescence was measured using a photomultiplier (Hamamatsu H7421). The ingoing and outgoing chamber concentrations of gaseous NO_2 were measured simultaneously. Calibrations using a NO_2 standard (≈5ppmv, Praxair) were performed at 1-2 hour intervals.

Ingoing and outgoing chamber concentrations of CO_2 and H_2O vapor were monitored using LI-6262 and LI-7000 CO_2/H_2O gas analyzers (LI-COR Biosciences). The LI-6262 was operated in absolute mode and was used to determine ingoing [CO_2] and [H_2O] with N_2 used as the reference gas. The LI-6262 was calibrated weekly using a CO_2 cylinder (450 ppmv, Praxair) and LI-610 Dew Point Generator (LICOR Biosciences). The LI-7000 was operated in differential mode to determine the changes in [CO_2] and [H_2O] and was calibrated daily. LI-7000 calibrations were performed using the LI-610 and a lower concentration CO_2 cylinder (380 ppmv, Praxair).

2.3.4 Nitrogen fertilization and drought stress studies

Six Douglas fir (*Pseudotsuga menziesii*) and six coast live oak (*Quercus agrifolia*) saplings were split into two groups: a control group watered with deionized water and a fertilized group watered with 20 mM ammonium nitrate. *P. menziesii* and *Q. agrifolia* were selected for the fertilization study because of their high prevalence and large distribution across California and to test if any tree-type (ie. conifer vs broadleaf) differences existed (Delaria et al., 2020). The saplings were watered with a volume of 250 ml of their respective treatment three times a week for a period of four months before deposition experiments began. Soil NH_4^+ and NO_3^- concentrations were determined from soil cores using a colorimetric synthesis followed by an absorbance analysis (Sims et al., 1995; Decina et al., 2017). In addition to soil nitrogen availability, the percent leaf nitrogen of each tree was measured using an ICP Optima 7000 DV instrument. Drought-stress experiments were conducted on *Pinus ponderosa* and *Calocedrus decurrens*, two species known for their drought-tolerance (FEIS). Three individuals of each species were used for the control group and drought-stress group, respectively. The control group was watered everyday and the drought-stressed trees were watered with 250 mL once every four weeks. The trees underwent the drought stress process 60 days before deposition experiments were run. PAN and PPN deposition rates were then measured for approximately 40 days. During this time, the control group was watered daily and the experimental group was watered every two weeks with 50 mL of tap water. The water potential (Ψ_p) of all 12 trees were monitored using leaf cuttings and a Scholander pressure chamber (PMS Instrument Company Model 670) to determine the water-status of the trees while deposition experiments were run. Additional details are presented in Delaria et al. (2020).

2.3.5 Calculations of deposition parameters

2.3.5.1 Calculation of peroxynitrate deposition fluxes and deposition velocities

The total APN flux through the Teflon chamber is a function of the APN deposition to the tree branches, exchange with the chamber walls, and thermal decomposition to NO_2. In order to isolate the branch deposition flux, empty chamber experiments with PAN and PPN under varying conditions (RH = 0 - 90%, T = 18 - 24 °C) were conducted. These experiments showed no evidence of a chamber wall effect. Approximately 3% of the APN concentration was observed to undergo thermal decomposition to NO_2, varying slightly with ambient temperature. This is negligible compared to other uncertainties in the analysis. The deposition flux was calculated using Equation 2.1, using the ingoing APN concentration ($C_{APN,in}$; nmol m^{-3}), the outgoing APN concentration ($C_{APN,out}$; nmol m^{-3}), the flow rate into the chamber (Q; m s^{-1}), and the one-sided leaf area (A; m^2) (Breuninger et al., 2012).

$$Deposition flux = \frac{Q(C_{APN,in} - C_{APN,out})}{A} \tag{2.1}$$

In order to determine the ingoing and outgoing concentrations of APN an average of the fluorescence signal from each LIF cell was calculated for the final 20 minutes of each concentration time step. The final values of $C_{APN,in}$ and $C_{APN,out}$ were calculated by taking the total fluorescence signals measured in cells 1 and 2 and correcting for the ingoing and outgoing NO_2 signals measured in cells 3 and 4 (Figure 2.1b). The computed standard deviation in each signal was propagated as the uncertainty in the measurement. The chamber flow rate was measured before and after each experiment and varied by less than 50 ccm

(< 1% uncertainty). The leaf area for each tree sapling was estimated by using computer software (ImageJ) to analyze scans of tree leaf traces. This method yielded variability in leaf area; a 10% uncertainty was assigned to each leaf area calculation (Schneider et al., 2012). The uncertainty in the APN fluxes was determined by propagating the individual uncertainties in A, Q, $C_{APN,in}$, and $C_{APN,out}$. Traces of sample deposition experiments are presented in Figure S1 to show the relative changes in $C_{APN,in}$ and $C_{APN,out}$ and magnitude of the observed fluxes for a single high and a single low deposition experiment. For the sample high deposition experiment in Figure 2.A1 there was an observed change of 75% between $C_{APN,in}$ and $C_{APN,out}$. The APN deposition fluxes were used to calculate an overall deposition velocity (V_d) for each experiment following Equation 2.2.

$$Deposition\,flux = V_d\,C_{APN,out} \tag{2.2}$$

Deposition velocities (V_d) were calculated by plotting the measured deposition fluxes in a single experiment against their corresponding chamber concentration ($C_{APN,out}$) and determining the slope of the line of best fit, weighted by the uncertainties in each variable. The uncertainty in V_d was taken to be the uncertainty in the fitted slope. During a large number of APN deposition experiments there were simultaneous experiments conducted that investigated NO_2 deposition to the trees (see Delaria et al. (2020)). Quantitative comparison of APN, H_2O and CO_2 gas exchange fluxes between experiments with and without NO_2 showed that there were no interferences from running concurrent NO_2 deposition experiments. The total number of deposition experiments run on each tree species can be found in Table 2.1 in Section 2.4.1.

2.3.5.2 Calculation of stomatal conductances and stomatal limit fluxes

Stomatal conductances to PAN ($g_{s,PAN}$) and PPN ($g_{s,PPN}$) were calculated by scaling measurements of stomatal conductance to water vapor ($g_{s,H2O}$) by the ratio of PAN/PPN diffusivity to H_2O diffusivity. Diffusivity scaling factors of 0.41 and 0.36 were calculated for PAN and PPN, respectively, using the Wilke-Lee diffusivity model (Wilke and Lee, 1955). Stomatal conductance to water vapor ($g_{s,H2O}$) was calculated following the method outlined in von Caemmerer and Farquhar (1981). Briefly, a transpiration rate (E) is calculated via equation 2.3 using measurements of the molar flow rate into the chamber (Q), the total one sided leaf area (A), the mole fraction of water vapor entering the chamber (w_{in}) and the mole fraction of vapor leaving the chamber (w_{out}). The total conductance to water vapor ($g_{t,H2O}$) is then calculated using Equation 2.4, where w_l is the mole fraction of water vapor inside the leaf and is assumed as the saturation vapor pressure at the measured leaf temperature. Finally, $g_{s,H2O}$ was calculated from $g_{t,H2O}$ via equation 2.5, which describes $g_{t,H2O}$ as a function of stomatal conductance ($g_{s,H2O}$) and the leaf boundary layer conductance ($g_{b,H2O}$).

$$E = \frac{Q(w_{out} - w_{in})}{A(1 - w_{out})} \tag{2.3}$$

$$g_{t,H2O} = \frac{E(1 - \frac{w_l + w_{out}}{2})}{(w_l - w_{out})} \tag{2.4}$$

$$\frac{1}{g_{s,H2O}} = \frac{1}{g_{t,H2O}} - \frac{1}{g_{b,H2O}} \tag{2.5}$$

A lower bound on $g_{b,H2O}$ for the empty chamber was determined to be 1.7 cm s^{-1} from previously reported experiments (Delaria et al., 2018). This value of $g_{b,H2O}$ is expected to be higher with a branch in the chamber with an increase in surface roughness (Pape et al., 2009). As a result, the contribution from $g_{b,H2O}$ to equation 2.5 was assumed to be negligible and $g_{s,H2O}$ was equated to $g_{t,H2O}$ in all calculations. Leaf temperatures varied along a single branch during an experiment and as a consequence resulted in the greatest uncertainty in stomatal conductance calculations. To account for this, uncertainty was propagated in w_l assuming leaf temperatures fluctuated between ± 2 °C during a given experiment. This uncertainty was minimized by keeping the chamber humidity below 80%. Stomatal limit fluxes were predicted using stomatal conductance measurements ($g_{s,PAN}$ or $g_{s,PPN}$) and ambient chamber concentrations ($C_{PAN,out}$ or $C_{PPN,out}$) following Equation 2.6. The stomatal limit fluxes describe an upper limit on stomatal APN deposition by assuming APN uptake is driven solely by stomatal diffusion and that there is no contribution from mesophyll processes (ie. the APN concentration in the substomatal cavity is essentially zero).

$$Stomatal\,limit\,flux = g_{s,PAN}\,C_{PAN,out} \;\; or \;\; g_{s,PPN}C_{PPN,out} \tag{2.6}$$

Stomatal limit fluxes were plotted against measured fluxes for each experiment and a stomatal scaling factor was determined by using a least squares weighted fit. An overall stomatal scaling factor was then calculated for each tree species by taking the weighted mean and weighted error of all slopes from the total number of experiments. A Tietjen-Moore outlier test was applied to the final dataset to remove suspected outliers most likely caused by uncertainty in the leaf temperature or daily drift in the Licor measurements (Tietjen and Moore, 1972).

2.4 Results

2.4.1 PAN deposition to California-native species

Figure 2.2 shows deposition fluxes measured to an *Acer macrophyllum* sapling branch under light and dark conditions. A linear relationship was observed between the deposition flux of PAN and the PAN mixing ratio during light experiments for all tree species.

The maximum deposition velocities (V_d) and stomatal conductances to water vapor ($g_{s,H2O}$) observed over all sets of experiments for each California-native tree species are summarized in Table 2.1. The highest observed deposition of PAN was to Pinus sabiniana

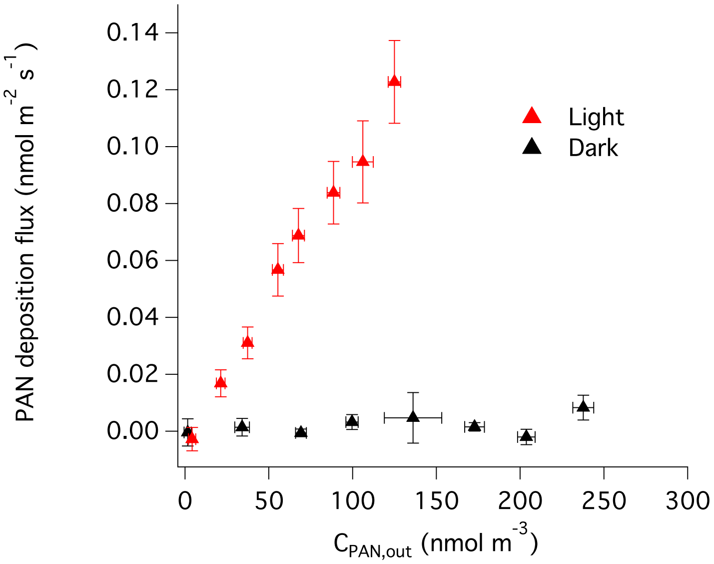

Figure 2.2: The measured deposition fluxes versus ambient chamber peroxyacetyl nitrate (PAN) concentrations during a light and dark deposition experiment run during a 24-hour period on a single *Acer macrophyllum* branch

(V_d = 0.30 ± 0.02 cm s^{-1}). The highest rates of stomatal conductance under these conditions were also measured for *Pinus sabiniana* ($g_{s,H2O}$ = 0.9 ± 0.3 cm s^{-1}). A high maximum deposition velocity (V_d = 0.21 ± 0.02 cm s^{-1}) and maximum stomatal conductance ($g_{s,H2O}$ = 0.5 ± 0.1 cm s^{-1}) were also observed for *Acer macrophyllum*. The other California-native tree species investigated had comparably lower maximum deposition velocities (V_d range = 0.12 – 0.15 cm s^{-1}) and maximum stomatal conductances ($g_{s,H2O}$ = 0.26 – 0.53 cm s^{-1}).

The largest deposition velocity measured during dark experiments was recorded for *Pinus sabiniana* (V_d = 0.095 ± 0.009 cm s^{-1}) and coincided with the highest measurement of stomatal conductance ($g_{s,H2O}$ = 0.36 ± 0.05 cm s^{-1}) during experiments run in the dark. Non-negligible PAN deposition was also measured to *Acer macrophyllum* (V_d = 0.071 ± 0.007 cm s^{-1}) and *Arbutus menziesii* (Vd = 0.042 ± 0.004 cm s^{-1}) during dark experiments. These measurements were also related to leaf stomatal-opening in the dark. No significant PAN deposition or stomatal-opening was observed in the dark for *Quercus douglasii*, *Pinus contorta*, or *Sequoia sempervirens*. These experiments show that the branch-level deposition of PAN occurred proportionally with leaf stomatal conductance and that at near stomatal closure ($g_{s,H2O}$ < 0.03 cm s^{-1}) there was no observed PAN deposition in any of the tree species.

Table 2.1: Observations of maximum PAN V_d and $g_{s,H2O}$ values for California-native tree species.

Tree species	Max light Vd	Max light gs,H2O	Max dark Vd	Max dark gs,H2O	Number of experiments
A. menziesii	0.15 ± 0.01	0.5 ± 0.1	0.042 ± 0.004	0.13 ± 0.02	14
A. macrophyllum	0.21 ± 0.02	0.5 ± 0.1	0.071 ± 0.007	0.14 ± 0.02	10
Q. douglasii	0.14 ± 0.01	0.4 ± 0.1	0.003 ± 0.003	0.016 ± 0.002	17
Q. agrifolia	0.09 ± 0.01	0.26 ± 0.05	—	—	13
S. sempervirens	0.15 ± 0.02	0.53 ± 0.09	0.002 ± 0.002	0.03 ± 0.01	17
P. ponderosa	0.11 ± 0.01	0.37 ± 0.07	—	—	9
P. sabiniana	0.3 ± 0.02	0.9 ± 0.2	0.095 ± 0.009	0.36 ± 0.05	20
P. contorta	0.12 ± 0.02	0.44 ± 0.07	0.007 ± 0.007	0.007 ± 0.001	9
P. menziesii	0.11 ± 0.02	0.44 ± 0.06	—	—	7
C. decurrens	0.12 ± 0.02	0.44 ± 0.06	—	—	7

2.4.2 Role of stomatal diffusion in PAN uptake

Figure 2.3 shows the relationship between stomatal limited PAN fluxes and experimentally measured PAN fluxes for *Pinus sabiniana.* A strong linear relationship between the predicted fluxes and measured PAN fluxes was observed both for individual experiments and across the amalgamation of experiments (n = 20). The measured flux was 70% of the stomatal limit when compared to measurements of $g_{s,PAN}$, indicating that another process inside the leaf mesophyll is limiting PAN uptake. Similar linear relationships between the maximum stomatal flux and the observed flux were observed for all trees we studied (Table 2.2). An overall weighted average stomatal scaling factor of 0.73 ± 0.03 was calculated for the California-native tree species investigated. A wide range of stomatal scaling factors observed during the experiments, but the variability appears random and reasonable given uncertainties in calculations of $g_{s,PAN}$ (± 30%).

Deposition scaling factors correlated directly with measurements of $g_{s,H2O}$ are also presented in Table 2, and on average scale at about 30% with $g_{s,H2O}$ measurements. The weighted fits for all tree species yielded intercepts that were either not statistically significant from zero or were within the instrument detection limit. This result also suggests that PAN deposition does not occur when leaf stomata are closed.

2.4.3 Effects of tree nitrogen status on PAN uptake

The 0 mM and 20 mM NH_4NO_3 water treatments given to *Quercus agrifolia* and *Pseudotsuga menziesii* resulted in a wide range of soil nitrogen availability (0-1000 μg/g N) and leaf nitrogen quantities (10-50 leaf C/N) across the 12 *Quercus agrifolia* and *Pseudotsuga menziesii* saplings used in the investigation (Figure S2). Although the fertilization treatment

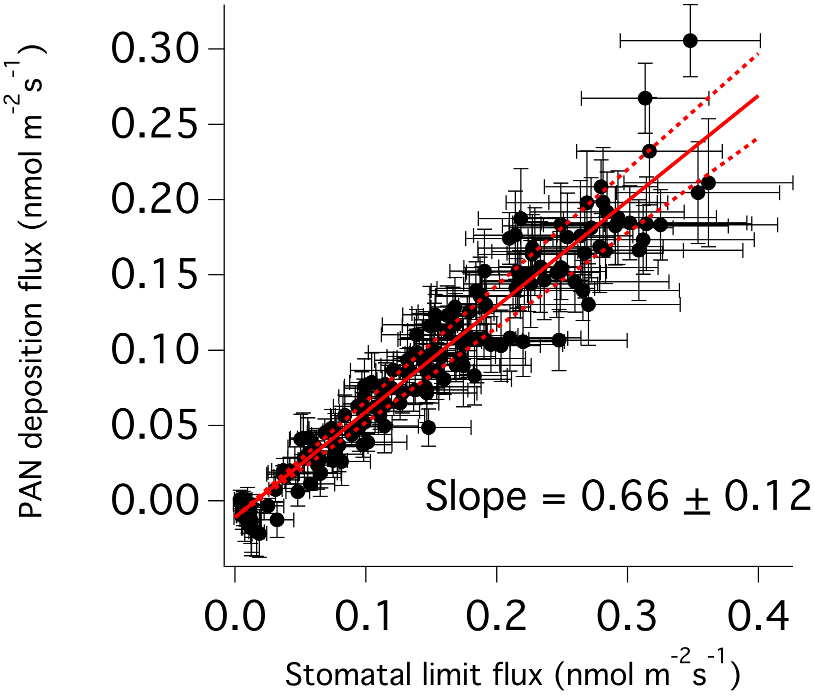

Figure 2.3: The relationship between measured peroxyacetyl nitrate (PAN) fluxes and the stomatal limit fluxes for *Pinus sabiniana* across n = 20 experiments

.

Table 2.2: Average weighted stomatal scaling factors and range of stomatal scaling factors to both $g_{s,PAN}$ and $g_{s,H2O}$ for PAN.

Tree species	Average stomatal scaling factor to $g_{s,PAN}$	Range of $g_{s,PAN}$ scaling factors	Average stomatal scaling factor to $g_{s,H2O}$
A. menziesii	0.76 ± 0.14	0.65 - 1.12	0.31 ± 0.06
A. macrophyllum	0.75 ± 0.13	0.46 - 1.03	0.31 ± 0.05
Q. douglasii	0.75 ± 0.11	0.45 - 1.06	0.31 ± 0.04
Q. agrifolia	0.72 ± 0.1	0.54 - 0.95	0.30 ± 0.04
S. sempervirens	0.68 ± 0.14	0.36 - 0.97	0.28 ± 0.06
P. ponderosa	0.76 ± 0.07	0.66 - 0.89	0.31 ± 0.03
P. sabiniana	0.66 ± 0.12	0.38 - 0.82	0.27 ± 0.05
P. contorta	0.76 ± 0.12	0.61 - 1.05	0.31 ± 0.05
P. menziesii	0.66 ± 0.09	0.57 - 0.83	0.27 ± 0.04
C. decurrens	0.66 ± 0.07	0.51 - 0.84	0.27 ± 0.03

resulted in differences in nitrogen assimilation, there was no significant trend or change in the measured stomatal scaling factors (Figure 2.A2). The average stomatal scaling factors for the experiments run with *Quercus agrifolia* saplings were determined to be 0.72 ± 0.1 and 0.71 ± 0.12 for the 0mM and 20mM treatment groups, respectively. Similarly PAN uptake scaled on average with a factor of 0.66 ± 0.09 for the control treatment and 0.71 ± 0.14 for the experimental treatment for the *Pseudotsuga menziesii* trees. Average V_d rates measured between the control and experimental groups were different because of changes in the stomatal responses in the saplings. In *Quercus agrifolia* the average stomatal conductance to H_2O across the saplings that received the 0mM treatment was 0.4 ± 0.2 cm s^{-1} versus 0.08 ± 0.07 cm s^{-1} measured for the saplings receiving the 20mM treatment. This difference was not as pronounced for *Pseudostuga menziesii* with an average stomatal conductance to H_2O of 0.2 ± 0.1 cm s^{-1} for the 0mM treatment and 0.15 ± 0.1 cm s^{-1} for the 20mM treatment.

2.4.4 Effects of tree water status on PAN uptake

The drought-stress study conducted on *Calocedrus decurrens* and *Pinus ponderosa* resulted in saplings with varying degrees of tree water status as evident by a wide range of leaf water potential measurements (Figure 2.A3). Tree water status did not significantly impact the stomatal scaling factors in either of the tree species. The average scaling factors calculated for the *Calocedrus decurrens* control and experimental saplings were 0.66 ± 0.09 and 0.67 ± 0.11, respectively. The average scaling factor for the *Pinus ponderosa* control group was 0.76 ± 0.07 and was 0.68 ± 0.14 for the experimental group. The water status of the saplings did have an effect on stomatal opening and consequentially the deposition rate of PAN. The average stomatal conductances were a factor of 2-3 lower in the drought-stress group than the control group for both *Calocedrus decurrens* (0.30 ± 0.09 cm s^{-1} vs 0.16 ± 0.03 cm s^{-1}) and *Pinus ponderosa* (0.29 ± 0.05 cm s^{-1} vs 0.1 ± 0.1 cm s^{-1}).

2.4.5 PPN deposition to *Quercus douglasii* and *Acer macrophyllum*

Figure 2.4 shows the stomatal limit fluxes versus the measured fluxes for PPN deposition experiments to Quercus douglasii and Acer macrophyllum under light conditions. PPN deposition stomatal scaling factors were calculated as 0.97 ± 0.08 and 0.92 ± 0.15 for *Quercus douglasii* and *Acer macrophyllum*, respectively. These calculated scaling factors were not statistically different from 1 for both tree species, implying that stomatal diffusion is rate limiting for PPN. A maximum V_d of 0.12 ± 0.02 cm s^{-1} was measured for *Quercus douglasii* and of 0.19 ± 0.02 cm s^{-1} for *Acer macrophyllum.* The maximum PPN deposition velocities observed to these species were not statistically different from observations of maximum PAN velocities.

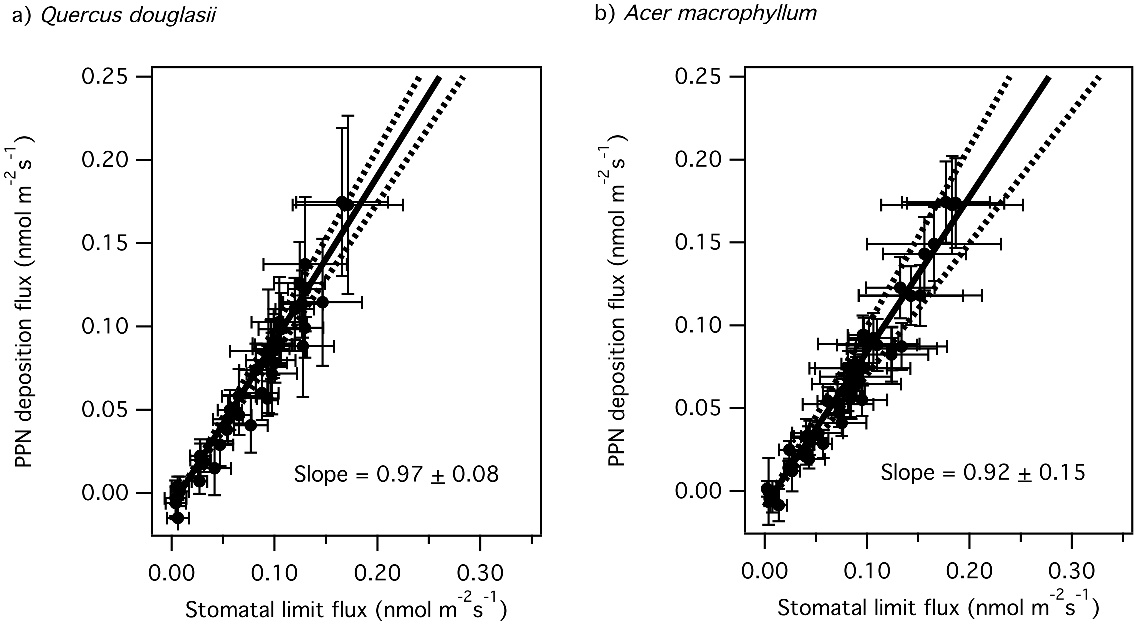

Figure 2.4: The relationship between measured peroxypropionic nitrate (PPN) fluxes and stomatal limit fluxes for a) *Quercus douglasii* and b) *Acer macrophyllum*

.

2.5 Discussion

2.5.1 Discussion of branch-level APN deposition

The stomatal control in APN uptake we observe is largely consistent with previous leaf-level deposition measurements of PAN to conifer and broadleaf tree species, and other types of vegetation (Okano et al., 1990; Sparks et al., 2003; Teklemariam and Sparks, 2004; Sun et al., 2016a,b) In all of these studies PAN deposition was governed mainly by leaf stomatal uptake. Teklemariam and Sparks (2004) and Sun et al. (2016) did attribute some PAN deposition to crops to surface deposition processes in their experiments, however this was observed as a minor deposition pathway (Teklemariam and Sparks, 2004; Sun et al., 2016b). The maximum PAN V_d that we measured during this study to a tree sapling branch was a factor of five lower than previous maximum V_d measurements implied by leaf-level deposition experiments to North American broadleaf and conifer species (0.3 cm s^{-1} vs. 1.5 cm s^{-1}) (Sparks et al., 2003). However, this narrower range in our V_d measurements was consistent with the lower stomatal conductances observed during our experiments. The influence of mesophyllic processing of PAN in coniferous and broadleaf trees has been noted in previous leaf-level tree studies (Sparks et al., 2003; Sun et al., 2016b). A similar stomatal scaling factor (0.64 ± 0.02) to the ones determined during our study was measured for *Quercus ilex*, an oak species native to the Mediterranean region (Sun et al., 2016b). Measurements from the leaf-level investigation of PAN deposition to North American tree species suggested a scaling factor of ≈1 at low stomatal conductances, but this slope showed a decrease and eventual leveling-off as higher levels of stomatal conductances were reached (Sparks et al., 2003). This mesophyllic rate limit approached in the Sparks et al. (2003) study was not observed in our investigation, a discrepancy that could be the result of the smaller stomatal conductance during our experiments (Sparks et al., 2003). The fate of APNs once they've diffused through the leaf stomata and into the mesophyll still remains uncertain. The solubilities of these peroxynitrates are low and their hydrolysis reactions are slow so dissolution and reaction of APNs with water in the leaf apoplastic fluid are unlikely given the high rates of observed deposition (Kames et al., 1991). It is more likely that APNs are taken up in the leaf-mesophyll via a secondary reaction or via an enzymatic process. An isotopic labeling or gene-expression study investigating the fate of PAN once in the mesophyll would compliment both this work and previous studies that have investigated the mesophyllic uptake of PAN.

The presence of excess nitrogen in the trees did not cause any significant changes in the overall APN stomatal scaling rates. This result implies that the build-up and assimilation of NO_3^- and NH_4^+ in the leaf mesophyll does not rate-limit PAN uptake. Thus, it is likely that either the dissolution or breakdown of PAN in the leaf apoplastic fluid is contributing to the mesophyllic limit to the PAN deposition rate. A similar conclusion was drawn from leaf-level deposition experiments to North American crop species, where the authors determined there was no relationship between leaf N and PAN deposition (Teklemariam and Sparks, 2004). The water status of the tree also had no noticeable impact on the mesophyllic PAN uptake rate, indicating that any changes in the leaf internal environment brought on by drought-stress did not influence PAN processing. The changes we observed in stomatal conductances between the differing nitrogen fertilization and water treatment groups were likely due to salt and water stress in the tree saplings, which have been shown to reduce plant transpiration (Chaves et al., 2008). This was evident by the onset of leaf senescence and browning in some of the tree saplings towards the end of experimentation.

Our measurements of PPN deposition showed that PPN uptake scales nearly 1:1 with stomatal conductance. To our knowledge, these are the first laboratory measurements of PPN deposition to vegetation. The observed stomatal scaling implies that the diffusion of PPN through stomata is the rate-limiting step in leaf uptake. Further support for this hypothesis comes from the consideration of the stomatal scaling factors directly with $g_{s,H2O}$, which were determined to be 0.35 ± 0.03 for *Quercus douglasii* and 0.32 ± 0.05 for *Acer macrophyllum*. Since there were no statistical differences between these factors for PAN vs. PPN in all tree species, this highlights that the slower diffusion of PPN is more rate limiting than the mesophyllic processing of PPN during uptake. Therefore, given that PAN and PPN deposition scale comparably with $g_{s,H2O}$, it is likely that the mesophyllic processing proceeds in the same mechanistic way and rate for both peroxynitrates.

2.5.2 Implications for canopy-level deposition

To explore the impact that our findings have on the loss of atmospheric PAN we constructed a simple model of PAN stomatal and thermochemical loss in the atmospheric boundary layer. We use mechanisms with the thermal decomposition rate (R2.3) and the reactive loss of the peroxyacetyl radical (R2.4 and R2.5).

$$\mathrm{CH_3C(O)O_2 + NO_2 \longleftrightarrow CH_3C(O)O_2NO_2} \qquad \text{(R 2.3)}$$

$$\mathrm{CH_3C(O)O_2 + NO \longrightarrow CH_3C(O)O + NO_2} \qquad \text{(R 2.4)}$$

$$\mathrm{CH_3C(O)O_2 + RO_2 \longrightarrow products} \qquad \text{(R 2.5)}$$

The total thermochemical flux in the boundary layer can then be determined by integrating over the boundary layer height following Equation 2.7 (Doskey et al., 2004; Wolfe et al., 2009). The stomatal flux in the boundary layer can be approximated by scaling up laboratory V$_d$ observations through Equation 2.8 by assigning a representative leaf area index (LAI) for the forest canopy. This approach to calculating a canopy deposition flux ignores the effects of vertical transport in the boundary layer and in-canopy effects but provides an estimation of the effect of canopy deposition on the APN flux.

$$Thermochemical\,flux = \int_z^{z_0} \frac{k_{-3}[CH_3C(O)O_2NO_2]}{1 + \frac{k_4[NO]}{k_3[NO_2]} + \frac{k_5[RO_2]}{k_3[NO_2]}} - k_{-3}[CH_3C(O)O_2NO_2]\,dz \qquad (2.7)$$

$$Stomatal\,flux = \int_z^{z_0} V_d[CH_3C(O)O_2NO_2](LAI)\,dz \qquad (2.8)$$

We ran simulations using V$_d$ values in the range of 0.1 – 0.4 cm s^{-1} to encompass the range of max g$_{s,PAN}$ observations in our study. The values for the rate constants were prescribed from the NASA JPL Chemical Kinetics and Photochemical Data Evaluation 18 (Burkholder et al., 2015). Calculations were performed assuming all RO$_2$ was in the form of HO$_2$, giving an upper bound on the thermochemical flux. Concentrations of the gaseous species were prescribed using the median noon mixing ratios of the species measured during the BEARPEX field campaign over a Ponderosa Pine forest in California, and are as follows: [NO] = 100 pptv, [NO2] = 400 pptv, [PAN] = 400 pptv, [HO2] = 100 pptv (Wolfe et al., 2009) The boundary layer height was fixed at 1000 meters. Temperature was varied with height in the model using a 6.5 °C/km lapse rate. LAI was prescribed as 5 m^2 m^{-2} for all model simulations. Figure 5 shows the fractional loss of PAN to deposition at noon versus noontime temperature for the highest and lowest prescribed values of V$_d$. The graph shows that there is a strong correlation between temperature and the amount of PAN lost to deposition, with less than 30% PAN lost to deposition when temperatures were greater than 20 °C. At higher rates of deposition (V$_d$ = 0.3 or 0.4 cm s^{-1}) PAN deposition exceeds its thermochemical loss at temperatures below 15 °C.

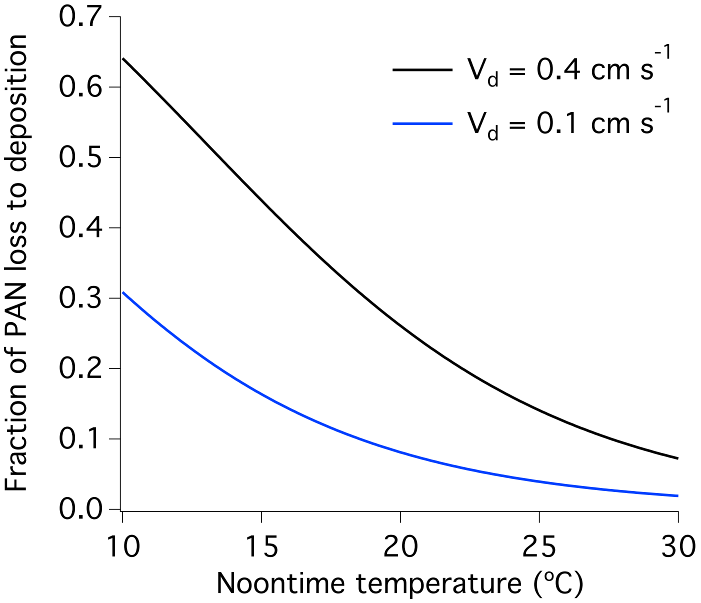

Figure 2.5: The effects of deposition velocity and temperature on PAN loss at noon in a 1000m boundary layer.

.

2.6 Conclusions

Laboratory investigation of the rates and processes controlling APN deposition to California-native trees shows that APN deposition to branch and cuticle surfaces is slow and that deposition is dominated by stomatal opening. The deposition of PAN and PPN to the tree saplings scaled proportionally to the stomatal limit with factors of 0.7 ± 0.03 and 0.95 ± 0.07 for PAN and PPN, respectively. A day-to-day variability in stomatal-scaling factors may indicate that the mesophyllic processing changes in response to certain environmental and biological factors, however we were not able to determine the direct cause. Tree nitrogen-status and water-status had no significant effect on stomatal-scaling factors, but did impact the overall deposition rate via changes in leaf stomatal response. The measurements we made at the branch-level imply that the stomatal deposition of APNs can be the primary loss of APNs in the boundary layer and adds to the growing body of knowledge that the dry deposition of NO_x and APNs to vegetation is primarily driven by stomatal-diffusion (Delaria et al., 2018, 2020; Sparks et al., 2003; Teklemariam and Sparks, 2004; Sun et al., 2016a,b). As a result, APNs may act as a NO_x sink rather than a NO_x reservoir in rural and remote forested regions when ambient temperature is low and the levels of stomatal uptake are high.

2.7 References

Breuninger, C., Oswald, R., Kesselmeier, J., and Meixner, F. X.: The dynamic chamber method: trace gas exchange fluxes (NO, NO_2, O_3) between plants and the atmosphere in the laboratory and in the field, Atmospheric Measurement Techniques, 5, 955–989, https://doi.org/10.5194/amt-5-955-2012, URL https://amt.copernicus.org/articles/5/955/2012/, 2012.

Burkholder, J. B., Sander, S. P., Abbatt, J., Barker, J. R., Huie, R. E., Kolb, C. E., Kurylo, M. J., Orkin, V. L., Wilmouth, D. M., and Wine, P. H.: Chemical Kinetics and Photochemical Data for Use in Atmospheric Studies, Tech. rep. 18, NASA Jet Propulsion Laboratory, Pasadena, CA, USA, 2015.

Chaves, M. M., Flexas, J., and Pinheiro, C.: Photosynthesis under drought and salt stress: regulation mechanisms from whole plant to cell, Annals of Botany, 103, 551–560, https://doi.org/10.1093/aob/mcn125, URL https://doi.org/10.1093/aob/mcn125, 2008.

Darer, A. I., Cole-Filipiak, N. C., O'Connor, A. E., and Elrod, M. J.: Formation and Stability of Atmospherically Relevant Isoprene-Derived Organosulfates and Organonitrates, Environmental Science & Technology, 45, 1895–1902, https://doi.org/10.1021/es103797z, URL https://doi.org/10.1021/es103797z, pMID: 21291229, 2011.

Day, D. A., Wooldridge, P. J., Dillon, M. B., Thornton, J. A., and Cohen, R. C.: A thermal dissociation laser-induced fluorescence instrument for in situ detection of NO2, peroxy nitrates, alkyl nitrates, and HNO3, Journal of Geophysical Research: Atmospheres, 107, ACH 4–1–ACH 4–14, https://doi.org/https://doi.org/10.1029/2001JD000779, URL https://agupubs.onlinelibrary.wiley.com/doi/abs/10.1029/2001JD000779, 2002.

Decina, D. M., Templer, P. H., Hutyra, L. R., Gately, C. K., and Rao, P.: Variability, drivers, and effects of atmopsheric nitrogen inputs across an urban area: Emerging patterns among human activities, the atmosphere, and soils, Science of the Total Environment, 609, 1524–1534, https://doi.org/10.1016/j.scitotenv.2017.07.166, 2017.

Delaria, E. R. and Cohen, R. C.: A model-based analysis of foliar NO_x deposition, Atmospheric Chemistry and Physics, 20, 2123–2141, https://doi.org/10.5194/acp-20-2123-2020, URL https://acp.copernicus.org/articles/20/2123/2020/, 2020.

Delaria, E. R., Vieira, M., Cremieux, J., and Cohen, R. C.: Measurements of NO and NO_2 exchange between the atmosphere and *Quercus agrifolia*, Atmospheric Chemistry and Physics, 18, 14 161–14 173, https://doi.org/10.5194/acp-18-14161-2018, URL https://acp.copernicus.org/articles/18/14161/2018/, 2018.

Delaria, E. R., Place, B. K., Liu, A. X., and Cohen, R. C.: Laboratory measurements of stomatal NO_2 deposition to native California trees and the role of forests in the NO_x cycle, Atmospheric Chemistry and Physics, 20, 14 023–14 041, https://doi.org/10.5194/acp-20-14023-2020, URL https://acp.copernicus.org/articles/20/14023/2020/, 2020.

Doskey, P. V., Kotamarthi, V. R., Fukui, Y., Cook, D. R., Breitbeil III, F. W., and Wesely, M. L.: Air-surface exchange of peroxyacetyl nitrate at a grassland site, Journal of Geophysical Research: Atmospheres, 109, https://doi.org/https://doi.org/10.1029/2004JD004533, URL https://agupubs.onlinelibrary.wiley.com/doi/abs/10.1029/2004JD004533, 2004.

Farmer, D. K., Wooldridge, P. J., and Cohen, R. C.: Application of thermal-dissociation laser induced fluorescence (TD-LIF) to measurement of HNO_3, Sigma;alkyl nitrates, Sigma;peroxy nitrates, and NO_2 fluxes using eddy covariance, Atmospheric Chemistry and Physics, 6, 3471–3486, https://doi.org/10.5194/acp-6-3471-2006, URL https://acp.copernicus.org/articles/6/3471/2006/, 2006.

FEIS: Fire Effects Information System, URL https://www.feis-crs.org/feis/.

Finlayson-Pitts, B. J. and Pitts Jr., J. N.: Chemistry of the Upper and Lower Atmosphere, Academic Press, 2000.

Fischer, E. V., Jacob, D. J., Yantosca, R. M., Sulprizio, M. P., Millet, D. B., Mao, J., Paulot, F., Singh, H. B., Roiger, A., Ries, L., Talbot, R. W., Dzepina, K., and Pandey Deolal, S.: Atmospheric peroxyacetyl nitrate (PAN): a global budget and source attribution, Atmospheric Chemistry and Physics, 14, 2679–2698, https://doi.org/10.5194/acp-14-2679-2014, URL https://acp.copernicus.org/articles/14/2679/2014/, 2014.

Furgeson, A., Mielke, L. H., Paul, D., and Osthoff, H. D.: A photochemical source of peroxypropionic and peroxyisobutanoic nitric anhydride, Atmospheric Environment, 45, 5025–5032, https://doi.org/https://doi.org/10.1016/j.atmosenv.2011.03.072, URL https://www.sciencedirect.com/science/article/pii/S1352231011003438, 2011.

Hudman, R. C., Moore, N. E., Mebust, A. K., Martin, R. V., Russell, A. R., Valin, L. C., and Cohen, R. C.: Steps towards a mechanistic model of global soil nitric oxide emissions: implementation and space based-constraints, Atmospheric Chemistry and Physics, 12, 7779–7795, https://doi.org/10.5194/acp-12-7779-2012, URL https://acp.copernicus.org/articles/12/7779/2012/, 2012.

Kames, J., Schweighoefer, S., and Schurath, U.: Henry's law constant and hydrolysis of peroxyacetyl nitrate (PAN), Journal of Atmospheric Chemistry, 12, 169–180, https://doi.org/10.1007/BF00115778, 1991.

Lee, L., Teng, A. P., Wennberg, P. O., Crounse, J. D., and Cohen, R. C.: On Rates and Mechanisms of OH and O3 Reactions with Isoprene-Derived Hydroxy Nitrates, The Journal of Physical Chemistry A, 118, 1622–1637, https://doi.org/10.1021/jp4107603, URL https://doi.org/10.1021/jp4107603, pMID: 24555928, 2014.

Min, K.-E., Pusede, S. E., Browne, E. C., LaFranchi, B. W., Wooldridge, P. J., Wolfe, G. M., Harrold, S. A., Thornton, J. A., and Cohen, R. C.: Observations of atmosphere-biosphere exchange of total and speciated peroxynitrates: nitrogen fluxes and biogenic sources of peroxynitrates, Atmospheric Chemistry and Physics, 12, 9763–9773, https://doi.org/10.5194/acp-12-9763-2012, URL https://acp.copernicus.org/articles/12/9763/2012/, 2012.

Moxim, W. J., Levy II, H., and Kasibhatla, P. S.: Simulated global tropospheric PAN: Its transport and impact on NO x, Journal of Geophysical Research: Atmospheres, 101, 12 621–12 638, https://doi.org/https://doi.org/10.1029/96JD00338, URL https://agupubs.onlinelibrary.wiley.com/doi/abs/10.1029/96JD00338, 1996.

Okano, K., Tobe, K., and Furukawa, A.: Foliar uptake of peroxyacetyl nitrate (PAN) by herbaceous species varying in susceptibility to this pollutant, New Phytologist, 114, 139–145, https://doi.org/10.1111/j.1469-8137.1990.tb00384.x, 1990.

Pape, L., Ammann, C., Nyfeler-Brunner, A., Spirig, C., Hens, K., and Meixner, F. X.: An automated dynamic chamber system for surface exchange measurement of non-reactive and reactive trace gases of grassland ecosystems, Biogeosciences, 6, 405–429, https://doi.org/10.5194/bg-6-405-2009, URL https://bg.copernicus.org/articles/6/405/2009/, 2009.

Perring, A. E., Pusede, S. E., and Cohen, R. C.: An observational perspective on the atmospheric impacts of alkyl and multifunctional nitrates on ozone and secondary organic aerosol, Chemical Reviews, 10, 5848–5870, https://doi.org/10.1021/cr300520x, 2013.

Rider, N. D., Taha, Y. M., Odame-Ankrah, C. A., Huo, J. A., Tokarek, T. W., Cairns, E., Moussa, S. G., Liggio, J., and Osthoff, H. D.: Efficient photochemical generation of peroxycarboxylic nitric anhydrides with ultraviolet light-emitting diodes, Atmospheric Measurement Techniques, 8, 2737–2748, https://doi.org/10.5194/amt-8-2737-2015, URL https://amt.copernicus.org/articles/8/2737/2015/, 2015.

Roberts, J. M. and Bertman, S. B.: The thermal decomposition of peroxyacetic nitric anhydride (PAN) and peroxymethacrylic nitric anhydride (MPAN), International Journal of Chemical Kinetics, 24, 297–307, https://doi.org/https://doi.org/10.1002/kin.550240307, URL https://onlinelibrary.wiley.com/doi/abs/10.1002/kin.550240307, 1992.

Romer, P. S., Duffey, K. C., Wooldridge, P. J., Allen, H. M., Ayres, B. R., Brown, S. S., Brune, W. H., Crounse, J. D., de Gouw, J., Draper, D. C., Feiner, P. A., Fry, J. L., Goldstein, A. H., Koss, A., Misztal, P. K., Nguyen, T. B., Olson, K., Teng, A. P., Wennberg, P. O., Wild, R. J., Zhang, L., and Cohen, R. C.: The lifetime of nitrogen oxides in an isoprene-dominated forest, Atmospheric Chemistry and Physics, 16, 7623–7637, https://doi.org/10.5194/acp-16-7623-2016, URL https://acp.copernicus.org/articles/16/7623/2016/, 2016.

Schneider, C. A., Rasband, W. S., and Eliceiri, K. W.: NIH Image to ImageJ: 25 years of image analysis, Nature Methods, 9, 671–675, https://doi.org/10.1038/nmeth.2089, 2012.

Sims, G. K., Ellsworth, T. R., and Mulvaney, R. L.: Microscale determination of inorganic nitrogen in water and soil extracts, Communications in Soil Science and Plant Analysis, 26, 303–316, https://doi.org/10.1080/00103629509369298, URL https://doi.org/10.1080/00103629509369298, 1995.

Singh, H. B. and Hanst, P. L.: Peroxyacetyl nitrate (PAN) in the unpolluted atmosphere: An important reservoir for nitrogen oxides, , 8, 941–944, https://doi.org/10.1029/GL008i008p00941, 1981.

Sparks, J. P., Roberts, J. M., and Monson, R. K.: The uptake of gaseous organic nitrogen by leaves: A significant global nitrogen transfer process, Geophysical Research Letters, 30, https://doi.org/https://doi.org/10.1029/2003GL018578, URL https://agupubs.onlinelibrary.wiley.com/doi/abs/10.1029/2003GL018578, 2003.

Sun, S., Moravek, A., Trebs, I., Kesselmeier, J., and Sörgel, M.: Investigation of the influence of liquid surface films on O3 and PAN deposition to plant leaves coated with organic/inorganic solution, Journal of Geophysical Research: Atmospheres, 121, 14,239–14,256, https://doi.org/https://doi.org/10.1002/2016JD025519, URL https://agupubs.onlinelibrary.wiley.com/doi/abs/10.1002/2016JD025519, 2016a.

Sun, S., Moravek, A., von der Heyden, L., Held, A., Sörgel, M., and Kesselmeier, J.: Twin-cuvette measurement technique for investigation of dry deposition of O_3 and PAN to plant leaves under controlled humidity conditions, Atmospheric Measurement Techniques, 9, 599–617, https://doi.org/10.5194/amt-9-599-2016, URL https://amt.copernicus.org/articles/9/599/2016/, 2016b.

Teklemariam, T. A. and Sparks, J. P.: Gaseous fluxes of peroxyacetyl nitrate (PAN) into plant leaves, Plant, Cell & Environment, 27, 1149–1158, https://doi.org/https://doi.org/10.1111/j.1365-3040.2004.01220.x, URL https://onlinelibrary.wiley.com/doi/abs/10.1111/j.1365-3040.2004.01220.x, 2004.

Tietjen, G. L. and Moore, R. H.: Some Grubbs-Type Statistics for the Detection of Several Outliers, Technometrics, 14, 583–597, https://doi.org/10.1080/00401706.1972.10488948, URL https://www.tandfonline.com/doi/abs/10.1080/00401706.1972.10488948, 1972.

Turnipseed, A. A., Huey, L. G., Nemitz, E., Stickel, R., Higgs, J., Tanner, D. J., Slusher, D. L., Sparks, J. P., Flocke, F., and Guenther, A.: Eddy covariance fluxes of peroxyacetyl nitrates (PANs) and NOy to a coniferous forest, Journal of Geophysical Research: Atmospheres, 111, https://doi.org/https://doi.org/10.1029/2005JD006631, URL https://agupubs.onlinelibrary.wiley.com/doi/abs/10.1029/2005JD006631, 2006.

Wilke, C. R. and Lee, C. Y.: Estimation of Diffusion Coefficients for Gases and Vapors, Industrial & Engineering Chemistry, 47, 1253–1257, https://doi.org/10.1021/ie50546a056, URL https://doi.org/10.1021/ie50546a056, 1955.

Wolfe, G. M., Thornton, J. A., Yatavelli, R. L. N., McKay, M., Goldstein, A. H., LaFranchi, B., Min, K.-E., and Cohen, R. C.: Eddy covariance fluxes of acyl peroxy nitrates (PAN, PPN and MPAN) above a Ponderosa pine forest, Atmospheric Chemistry and Physics, 9, 615–634, https://doi.org/10.5194/acp-9-615-2009, URL https://acp.copernicus.org/articles/9/615/2009/, 2009.

Yienger, J. J. and Levy, H.: Empirical model of global soil-biogenic NO emissions, Journal of Geophysical Research: Atmospheres, 100, 11 447–11 464, https://doi.org/https://doi.org/10.1029/95JD00370, URL https://agupubs.onlinelibrary.wiley.com/doi/abs/10.1029/95JD00370, 1995.

2.8 Appendix

Table 2.A1: Description of trees used in this study and geographical disribution of each species in California

Tree species	Tree type	Geographic distribution in California
A. menziesii	Broadleaf - Evergreen	North coast, Bay/Delta, Sierra, Central coast
A. macrophyllum	Broadleaf - Deciduous	North coast, Bay/Delta, Sierra, Central coast
Q. douglasii	Broadleaf - Deciduous	North coast, Bay/Delta, Sierra, Central coast
Q. agrifolia	Broadleaf - Evergreen	North coast, Bay/Delta, Central coast, South coast
S. sempervirens	Needleleaf - Evergreen	North coast, Bay/Delta, Central coast
P. ponderosa	Needleleaf - Evergreen	North coast, Bay/Delta, Modoc, Sierra
P. sabiniana	Needleleaf - Evergreen	North coast, Bay/Delta, Sierra, Modoc, Central coast
P. contorta	Needleleaf - Evergreen	North coast, Modoc, Sierra
P. menziesii	Needleleaf - Evergreen	North coast, Bay/Delta, Modoc, Sierra
C. decurrens	Needleleaf - Evergreen	North coast, Modoc, Sierra

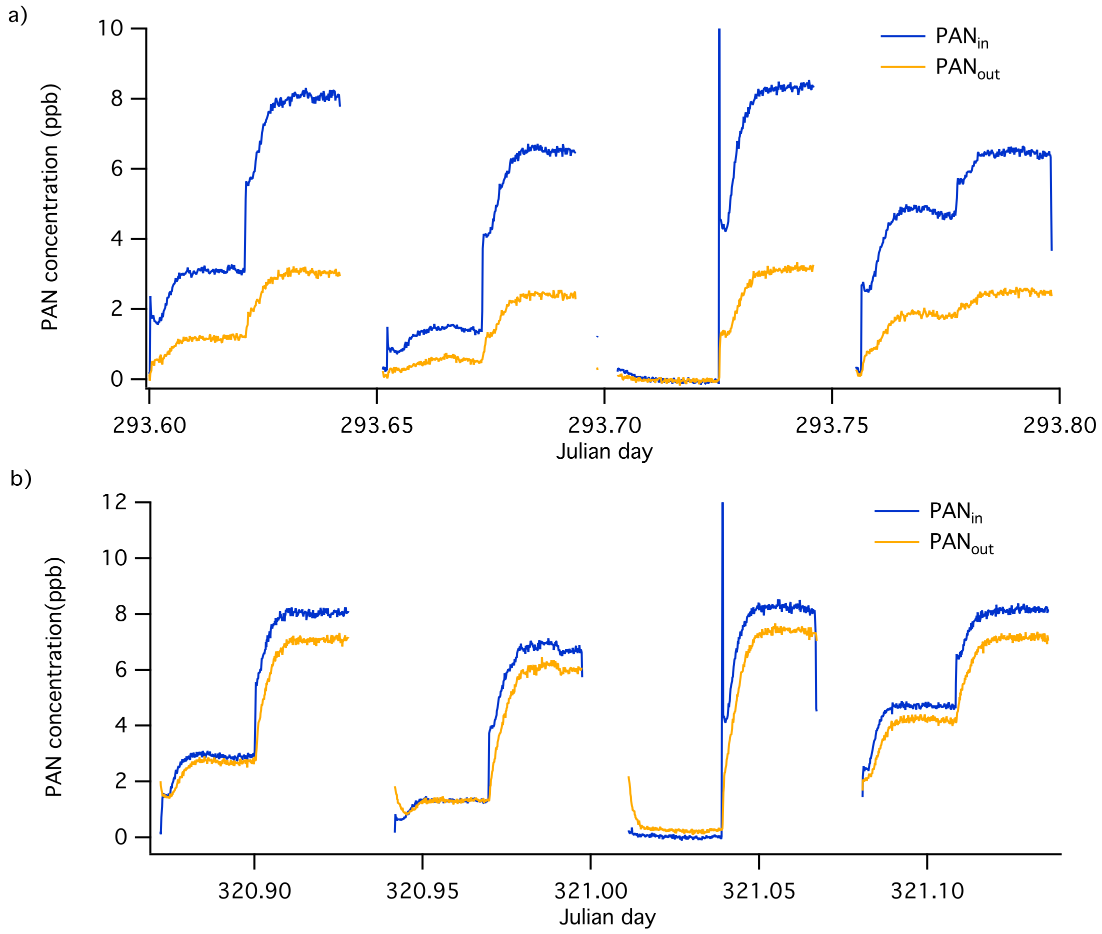

Figure 2.A1: a) A sample deposition experiment to *P. sabiniana* with a high measured deposition velocity (0.23 ± 0.02 cm s^{-1}) and high calculated stomatal conductance to H_2O (0.9 ± 0.2 cm s^{-1}) and b) A sample deposition experiment to *P. contorta* where the measured deposition velocity (0.03 ± 0.01 cm s^{-1}) and stomatal conductance to H_2O (0.13 ± 0.02 cm s^{-1}) were low

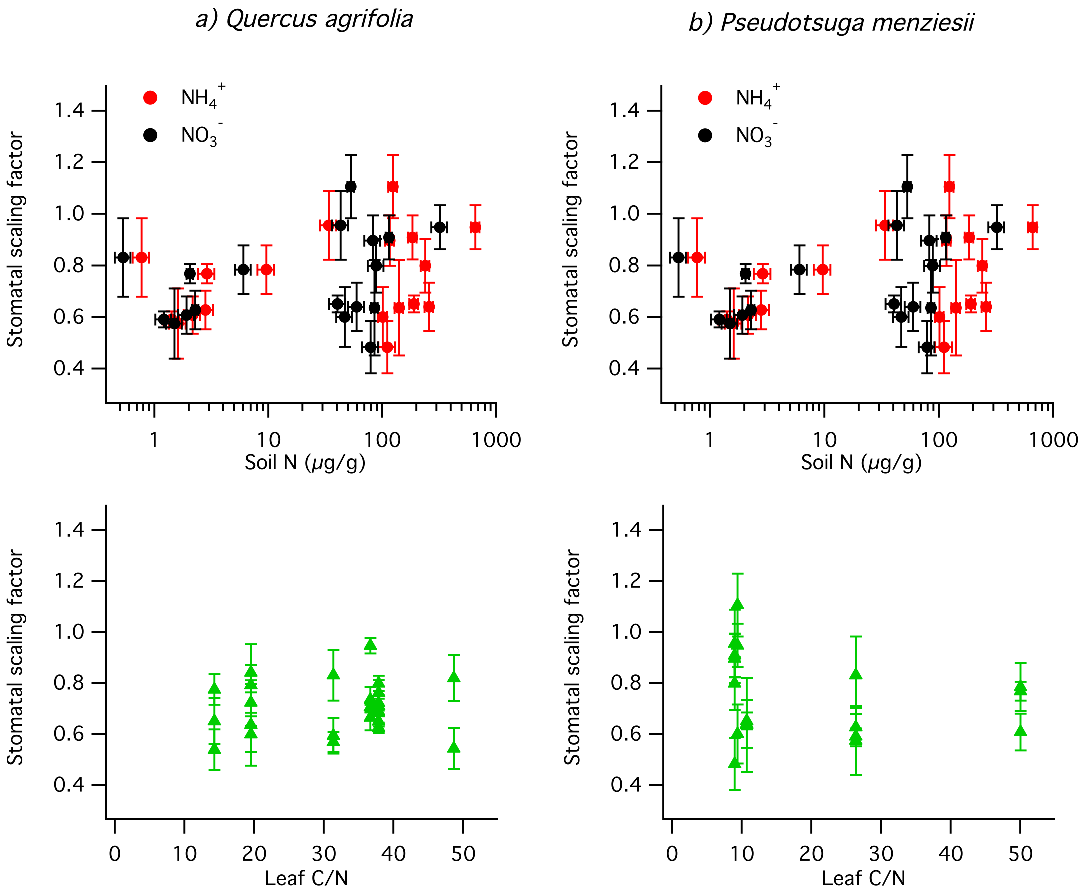

Figure 2.A2: The impact of soil nitrogen availability and leaf nitrogen status on the calculated stomatal scaling factors for a) *Q. agrifolia* and b) *P. mensiesii*

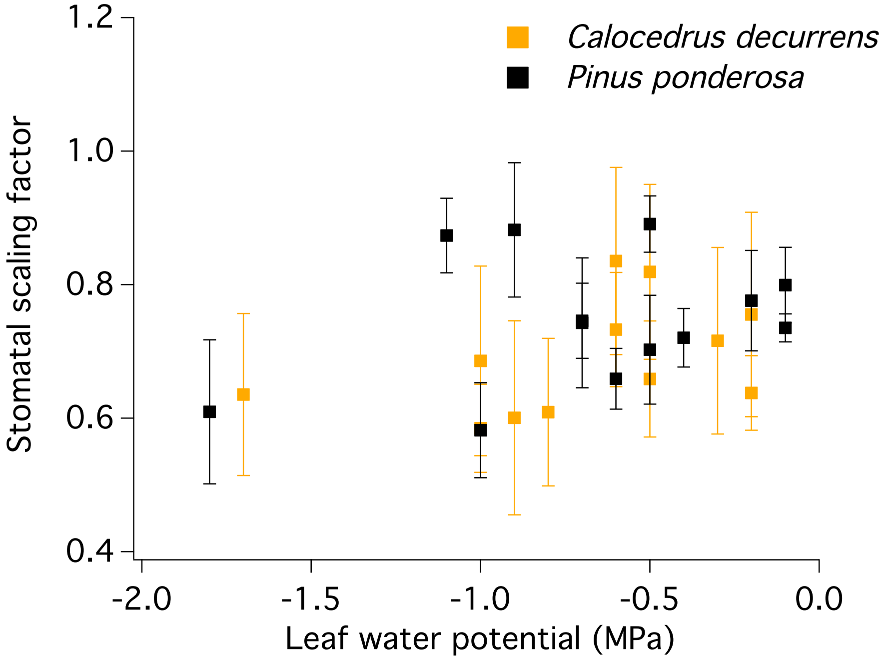

Figure 2.A3: The impact of tree water status, determined using leaf water potential, on the stomatal scaled PAN uptake rate for *C. decurrens* and *P. ponderosa*

Chapter 3

Leaf stomatal uptake of alkyl nitrates

Adapted from B. K. Place et al., Leaf stomatal uptake of alkyl nitrates, *Earth Sci. Technol. Lett.*, accepted.

3.1 Abstract

The relative role of the formation of atmospheric multifunctional and alkyl nitrates ($RONO_2$) is expected to increase as anthropogenic emissions of NO and NO_2 continue to decrease. A more complete understanding of the chemistry and fate of $RONO_2$ will therefore be needed in order to describe the composition of our atmosphere. In this study we investigate the atmospheric loss of short-chain alkyl nitrates via deposition to tree branches. Using a dynamic chamber we measure deposition fluxes of isopropyl nitrate (IPN), methylbutyl nitrate (MBN) and ethylhexyl nitrate (EHN) to *Pinus sabiniana* branches. Flux measurements showed a linear relationship between the stomatal uptake of EHN and MBN and their respective ambient chamber concentration and that deposition occurred solely through a leaf stomatal pathway. The observed rates of IPN, MBN, and EHN deposition were too fast to be described by a dissolution/hydrolysis mechanism, indicating that uptake was likely driven by an alternative process. We compared our measurements of maximum deposition rates of IPN, MBN and EHN with their photochemical losses and conclude that the stomatal uptake of these compounds accounts for no more than 20% of their total atmospheric losses.

3.2 Introduction

The chemistry and cycling of NO_x ($NO_x = NO + NO_2$) regulates the concentrations of key air pollutants and oxidants in our atmosphere. In highly polluted environments the NO_x cycle is typically terminated via the reaction of NO_2 with OH to form HNO_3, which then deposits rapidly to Earth's surface Finlayson-Pitts and Pitts Jr. (2000). In areas with lower NO_x concentrations, and a larger relative contribution from the reactivity of volatile organic compounds (VOCs), the formation of alkyl and multifunctional nitrates ($RONO_2$) can be the dominant NO_x sink (Browne and Cohen, 2012; Romer et al., 2016; Sobanski et al., 2017). For example, model simulations over the Eastern and Southern United States domain estimate that the fraction of NO_x lost to $RONO_2$ formation exceeds 50 percent (Fisher et al., 2016; Zare et al., 2018; Romer Present et al., 2020). As controls on anthropogenic NO_x emissions continue to tighten, it is predicted that the fractional NO_x loss to $RONO_2$ will continue to increase over time (Romer Present et al., 2020). The $RONO_2$ family is broad and consists of molecules with a range of chemical functionality (Perring et al., 2013). The chemical transformations and fate of atmospheric $RONO_2$ will largely depend on the properties of the attached organic chain (R). Alkyl nitrates, formed from the reaction of NO_x with alkanes, are the least reactive members of the $RONO_2$ family (Perring et al., 2013). The long lifetimes of alkyl nitrates ($\tau > 1$ day) has led to the ubiquitous detection of these species in urban, rural and remote environments (Atlas, 1988; Kastler et al., 2000; Blake et al., 2003). In contrast, hydroxynitrates and dinitrates have typically been measured nearer to source locations due to their relatively higher rates of photochemical loss and lower vapor pressures (Perring et al., 2013).

To date many investigations have focused on understanding the chemistry of atmospheric $RONO_2$ but less attention has been given to the role deposition plays in regulating the concentrations of these compounds. The deposition of alkyl nitrates to surfaces is typically not considered as an important loss process due to the high vapor pressures and low solubilities of many of these compounds (Sander, 2015; Kames and Schurath, 1992; Rumble, 2021). Field measurements have however measured morning minimums in C_1 - C_5 alkyl nitrate concentrations indicating that deposition could be occurring in the nighttime when the chemical losses of these nitrates are negligible (Russo et al., 2010; Abeleira et al., 2018). In the study conducted by Abeleira et al. (2018), they show that by including observed nighttime depositional losses for methyl nitrate in a mass balance model they were able to more accurately reproduce ambient measurements. During the SOAS campaign in the southeast United States, measurements of isoprene nitrate and propanone nitrate indicated that hydroxynitrates are lost rapidly from the atmosphere to surface deposition (Nguyen et al., 2015). The deposition fluxes of these compounds exhibited a midday maximum and were of comparable magnitude to the deposition of HNO_3. The controlled deposition of alkyl nitrates has also been measured using a leaf chamber (Lockwood et al., 2008). The authors of this investigation showed that methylbutyl nitrate (MBN) was taken up and utilized by the foliage. The estimated stomatal uptake rate from this study implies that the stomatal uptake of MBN could be competitive with its photochemical losses from the atmosphere.

To gain a better understanding of the processes and rates governing $RONO_2$ deposition we investigated the branch-level deposition of isopropyl nitrate (IPN), methylbutyl nitrate (MBN) and ethylhexyl nitrate (EHN) using a dynamic branch chamber (Delaria et al., 2018, 2020; Place et al., 2020). We manipulate the ambient environment in the chamber to determine the stomatal and non-stomatal deposition fluxes of these nitrates. Using the observations of the maximum deposition rates we describe a mechanism for uptake and compare the role of deposition of these nitrates with their respective photochemical losses.

3.3 Methods

3.3.1 Materials

Three *Pinus sabiniana* tree saplings were purchased from Forestfarm at Pacifica (Williams, OR) and were re-potted and grown in a lath house at the Berkeley Oxford facility. The trees were kept watered to saturation before and during experimentation. Isopropyl nitrate (IPN; 96%; Sigma Aldrich), methylbutyl nitrate (MBN; 97%; Sigma Aldrich) and ethylhexyl nitrate (EHN; 97%; Sigma Aldrich) were diluted by pipetting a small volume (4 - 20 µL) of each nitrate into separate 8.7 L aluminum cylinders. The cylinders were filled with N_2 to a pressure of approximately 700 psi to give final $RONO_2$ mixing ratios ranging from 1-5 ppmv.

3.3.2 Flux measurements

Deposition experiments were conducted by placing selected tree branches from the *Pinus sabiniana* saplings in a custom-built Teflon chamber and dosing them with 4-6 concentrations of each $RONO_2$ gas at concentrations ranging from 1-100 ppbv. A complete description of the dynamic chamber and $RONO_2$ measurement technique can be found elsewhere (Day et al., 2002; Delaria et al., 2020; Place et al., 2020). Deposition fluxes were calculated by multiplying the total flow rate (Q) by the difference in concentration of $RONO_2$ entering and exiting the chamber ($[RONO_2]_{in}$ - $[RONO_2]_{out}$) and dividing by branch leaf area (A) following equation 3.1.

$$Flux = \frac{Q}{A}([RONO_2]_{in} - [RONO_2]_{out}) \tag{3.1}$$

Nitrate deposition experiments run before the introduction of tree branches into the chamber showed evidence of adsorption and desorption of IPN, MBN and EHN to the chamber walls (Figures 3.A1 - 3.A3) and resulted in a 3-4 percent loss of the ingoing concentration of each alkyl nitrate. To account for these effects a zero air flow step was added between each flow step of $RONO_2$ into the chamber and branch deposition fluxes were corrected for these losses before being reported.

3.3.3 Measurements of stomatal conductance

Two LICOR gas analyzers (LI-6262/LI-7000) provided continuous measurements of water vapor during each experiment. Calculations of leaf stomatal conductance (g_s) were performed following the methods of von Caemerer and Farquhar (1981) using the difference in water vapor concentration entering and exiting the chamber. Previous chamber deposition experiments indicated that the aerodynamic and leaf boundary layer resistances contributed negligibly to the calculation of g_s and as such were not used in the determination of g_s in the present study. A complete description of the stomatal conductance methods, experiments and assumptions used are described in Place et al. (2020) and Delaria et al. (2020). We scale measurements of g_s using the molecular weights of each $RONO_2$ following Graham's law of Diffusion to account for differences in the stomatal diffusion rates between H_2O and the $RONO_2$ compound of interest and only report the scaled stomatal conductances to $RONO_2$. Stomatal conductance was varied between experiments by changing the concentration of water vapour or level of light exposure.

3.4 Results

Sample IPN, MBN and EHN deposition experiments run under conditions of high stomatal conductance ($g_s > 1$ cm s^{-1}) and low stomatal conductance ($g_s < 0.05$ cm s^{-1}) are shown in Figure 3.1. At levels of near stomatal closure ($g_s < 0.05$ cm s^{-1}) there was no observed deposition of any of the three nitrates to the *Pinus sabiniana* saplings. No significant deposition of IPN, MBN and EHN was observed for experiments run under both low humidity and dark conditions when g_s was low. Deposition of MBN and EHN to the trees was observed at higher levels of stomatal conductance ($g_s > 1$ cm s^{-1}). The observed stomatal uptake of EHN and MBN exhibited a linear relationship with the ambient chamber concentration and the measured deposition fluxes of EHN were typically 10 times higher than those of MBN at the same ambient chamber concentrations and under similar conditions of stomatal conductance (Figure 3.1). We saw no significant correlation between IPN deposition and stomatal opening, even at high ambient chamber concentrations of IPN (1000 - 2500 nnmol m^{-3}).

The slope of the linear relationship between the ambient alkyl nitrate concentrations and measured deposition fluxes represents the deposition velocity (V_d) of each species. The deposition velocities for IPN, MBN and EHN were calculated using weighted fits and are plotted in Figure 3.2 against average calculated stomatal conductances to IPN, MBN and EHN for each deposition experiment run. Figure 3.2 shows that there is some dependence of V_d on g_s for EHN, a very low dependence of V_d on g_s for MBN, and seemingly no relationship between these two measurements for IPN. The maximum observed deposition for EHN ($V_d = 0.047$ cm s^{-1}) was 7 times larger than the maximum observed deposition of MBN ($V_d = 0.0066$ cm s^{-1}), and 25 times larger than the maximum observed deposition of IPN ($V_d = 0.0019$ cm s^{-1}). Deposition experiments were briefly run with blue oak (*Quercus douglasii* saplings before the seasonal onset of senescence and a similar trend in the maximum deposition velocities between MBN and EHN was observed (Fig 3.A4).

The deposition trends in figure 3.2 can be represented by the Wesely model of stomatal uptake (Equation 3.2), where r_m is the mesophylic resistance and r_s is the resistance to stomatal diffusion or inverse of stomatal conductance (g_s)(Wesely, 1989).

$$V_d = \frac{1}{r_m + r_s} \tag{3.2}$$

Fitting the Wesely model (Eq. 3.2) to the data presented in Figure 3.2 gave r_m values of 17 ± 4 cm^{-1} s and 190 ± 30 cm^{-1} s for EHN and MBN, respectively. The order of magni-

a) IPN

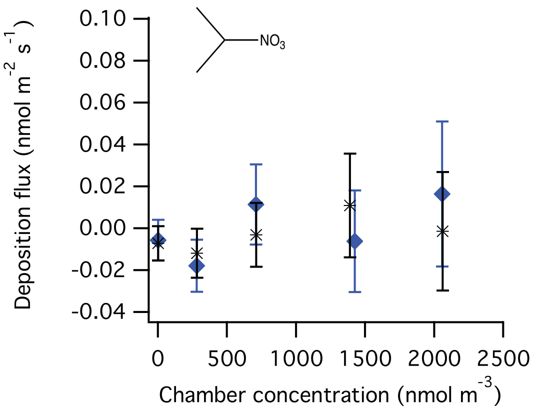

b) MBN

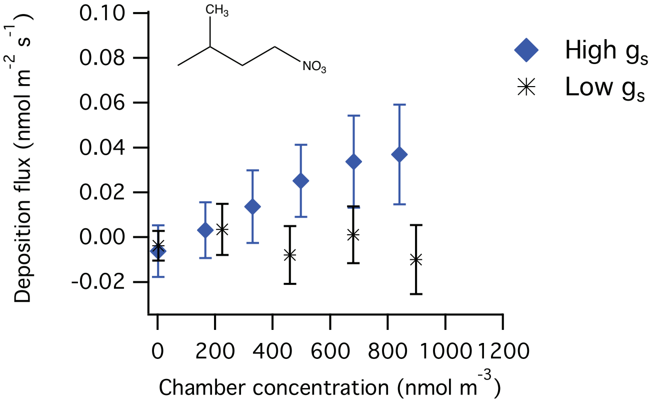

c) EHN

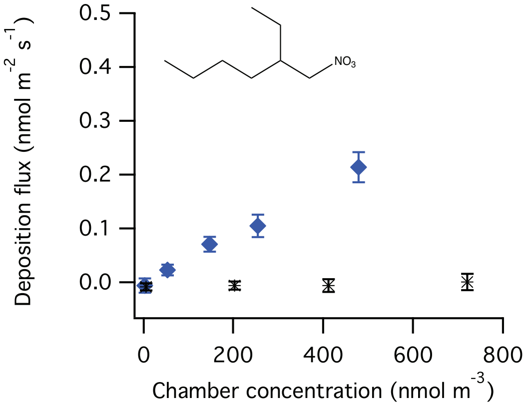

Figure 3.1: Sample deposition experiments of a) IPN, b) MBN, and c) EHN to the Pinus sabiniana saplings. Blue traces indicate experiments run with levels of high stomatal conductance ($g_s > 1$ cm s^{-1}) and black traces indicate expriments run under conditions of low stomatal conductance ($g_s < 0.05$ cm s^{-1}).

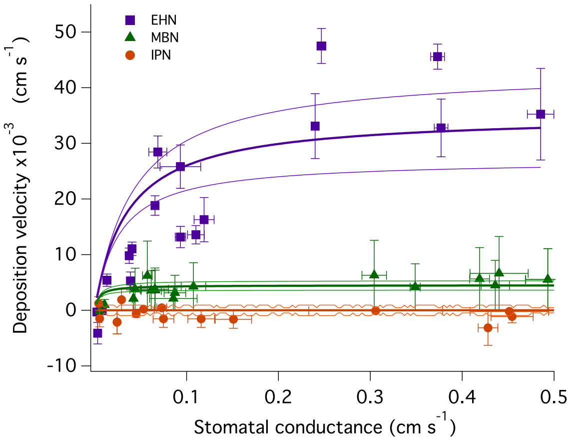

Figure 3.2: Relationship between the observed deposition velocities of IPN, MBN and EHN to the *Pinus sabiniana* and average measured leaf stomatal conductance across all experiments. The error in stomatal conductance was reported as the standard deviation in stomatal conductance across each experiment.

tude difference between these mesophyllic rates were consistent with the order of magnitude difference in deposition velocities for the two nitrates. A value of r_m could not be determined for IPN due to uncertainty in the data and levels of observed deposition that were near the limits of detection of the instrument. Fits were also performed under the assumption that there may be surface deposition occurring in parallel, described through a cuticular/branch resistance term (r_c). These fits returned large estimates of surface resistances (r_c >1000 cm^{-1} s), further supporting the hypothesis that deposition occurs solely through stomatal uptake.

3.5 Discussion

3.5.1 Leaf-level alkyl nitrate deposition

To our knowledge, the deposition of alkyl nitrates has been explored at the leaf-level in only one other study (Lockwood et al., 2008). In this previous study the researchers fumigated leaves of *Populus tremuloides* (trembling aspen) seedlings with a concentration of 350 - 700 ppbv of MBN over an 8-hour period. From their measurements Lockwood et al. (2008) calculated an MBN uptake rate of 0.012 $\pm$ 0.011 nmol N m^{-2} s^{-1} ppb^{-1} under conditions of moderate-high stomatal conductance (g_s = 100 - 300 mmol m^{-2} s^{-1}). They attributed all MBN deposition to stomatal uptake and proposed that deposition was limited by the processing of MBN inside the leaves. Through the use of isotopically labeled MBN, Lockwood et al. (2008) also showed that MBN was incoporated into leaf amino acids. The average

MBN uptake rate that we measured under conditions of high stomatal conductance (g_s = 450 - 600 mmol m^{-2} s^{-1}) was 0.002 ± 0.001 nmol N m^{-2} s^{-1} ppb^{-1}. This value falls within the uncertainty of the rate calculated by Lockwood et al. (2008) and similarly in our study, we attribute the deposition of $RONO_2$ to a stomatal pathway and find deposition is limited by the mesophyllic rate.

The processing mechanism within the leaf mesophyll that converts alkyl nitrates into a usable form of nitrogen remains unknown. Lockwood and colleagues proposed a dissolution/hydrolysis mechanism to explain the low integrated deposition rate they observed given that the solubilities of alkyl nitrates are low (H < 2 M atm^{-1}) and the neutral hydrolysis rates are slow (k_{hyd} < 1 x 10^{-5} s^{-1}) (Hu et al., 2011; Darer et al., 2011; Robertson et al., 1982; Baker and Easty, 1950; Kames and Schurath, 1992). A dissolution/hydrolysis model has previously been used to describe the deposition of peroxyacetyl nitrate to water surfaces, where the observed deposition rates were also low (V_d < 0.01 cm s^{-1}) (Kames et al., 1990). To test whether our measured deposition velocities could be explained by a hydrolysis mechanism we employ the same model used by Kames et al. (1990), which uses a steady-state flux balance approach incorporating the air-surface-bulk liquid interfaces to describe the deposition velocity of a compound via dissolution/hydrolysis. The model (Equation 3.3) describes hydrolysis-driven deposition using the Henry's law constant (H; unitless), neutral hydrolysis rate (k; s^{-1}) and the diffusion coefficient in water (D; cm^2 s^{-1}) of a depositing gas. The hydrolysis-driven deposition velocities for IPN, MBN and EHN calculated using this model (Equation 3.3) are presented in Table 1 alongside the maximum observed experimental velocities we measured for each compound. A detailed description of the methods and parameters used for the calculations can be found in the supplement.

$$V_d = H\sqrt{kD} \tag{3.3}$$

The hydrolysis modeled deposition velocities that we calculate (Table 3.1) are approximately two orders of magnitude lower than the measured velocities. This result suggests that deposition is not consistent with a dissolution/hydrolysis mechanisms. Further, the stomatal deposition rates for EHN that we measured were faster than those measured for peroxyacetyl nitrate to liquid water, despite EHN having a lower solubility and a slower hydrolysis rate, lending support to the idea of uptake via an alternative mechanism. Assuming that the uptake of alkyl nitrates in the leaf mesophyll still begins through dissolution and diffusion into the bulk liquid we can estimate the required reaction rates needed to explain our maximum measured V_d values for IPN, MBN and EHN. To do this, we calculate a required bulk-liquid reaction rate by substituting our maximum measured V_d into equation 3.3 and solving for k, where k now represents the unknown bulk-liquid reaction rate. We calculate that a bulk-liquid reactivity (Table 3.1) on the timescale of seconds to hours (0.001-1.5 hrs) is required to explain the observed deposition rates. This required reactivity is much faster than the rate of hydrolysis for the alkyl nitrates, which occurs on a timescale of days (7-300 days). There is also a possibility that a surface reaction or enzymatic process involving the alkyl nitrates may be occurring. These alternative modes of uptake have been suggested in

Table 3.1: Comparison of measured maximum deposition velocities with hydrolysis-mechanism modeled parameters for IPN, MBN and EHN.

Alkyl nitrate	Neutral hydrolysis rate (s^{-1})	Maximum observed V_d (cm s^{-1})	Hydrolysis modeled V_d (cm s^{-1})	Required reaction rate (s^{-1})
IPN	2.5 x 10^{-8}	1.9 x 10^{-3}	2 x 10^{-5}	2 x 10^{-4}
MBN	6 x 10^{-8}	6.6 x 10^{-3}	3 x 10^{-5}	3 x 10^{-3}
EHN	2 x 10^{-6}	4.7 x 10^{-2}	2 x 10^{-4}	2 x 10^{-1}

studies that explored the stomatal uptake of peroxyacetyl nitrate in tree leaves (Place et al., 2020; Sparks et al., 2003).

3.5.2 Canopy-level alkyl nitrate deposition

Measurements of ambient C_1 - C_5 alkyl nitrate mixing ratios at nighttime in the Colorado and New Hampshire have been used to estimate V_d for short-chain alkyl nitrate species (Abeleira et al., 2018; Russo et al., 2010). The estimated deposition velocities ranged from 0.04 cm s^{-1} for methyl nitrate to 0.21 cm s^{-1} for 3-pentyl nitrate. Since leaf stomata typically close during the night, it is likely that these calculated V_d values are representative of non-stomatal deposition processes. During our experiments we did not see any evidence of cuticulur or branch deposition to the *Pinus sabiniana* saplings under both light and dark conditions and low humidity and high humidity conditions, suggesting that the $RONO_2$ species may be depositing to other surfaces at night.

In Figure 3.3 we compare the stomatal losses of IPN, MBN, and EHN to their photochemical losses to determine if the deposition rates we measured could influence their atmospheric lifetimes. To make this comparison we assumed a daytime boundary layer of 1 km and that the maximum observed V_d for each nitrate from our experiments at the branch-level will scale proportionally with leaf cover (ie. leaf area index) at the canopy-level. This approach treats a canopy as one 'big-leaf' and ignores effects of canopy morphology and in-canopy transport, but is a good first-order estimate of the role of deposition in $RONO_2$ loss. We chose photochemical lifetimes of IPN (2 x 10^{-6} s^{-1}) and MBN (10 x 10^{-6} s^{-1}) to match summertime photochemical lifetimes for propyl nitrate and pentyl nitrate measured in the Colorado Front Range (Abeleira et al., 2018). We were unable to find reported photochemical lifetimes for EHN so we set a lifetime of 20 x 10^{-6} following the observed increasing trend in C_1 - C_5 photochemical loss observations. Figure 3.3 shows that even in areas of high tree cover, stomatal deposition will represent at most 20 percent of the loss for IPN, MBN, and EHN. The stomatal deposition of EHN could be a more important relative loss, however this may not be the case given the uncertainty in the assigned photochemical lifetime of EHN. The fractional deposition loss of alkyl nitrates would be larger than the estimates in Figure 3.3 if there are additional alkyl nitrate surface deposition pathways during the daytime.

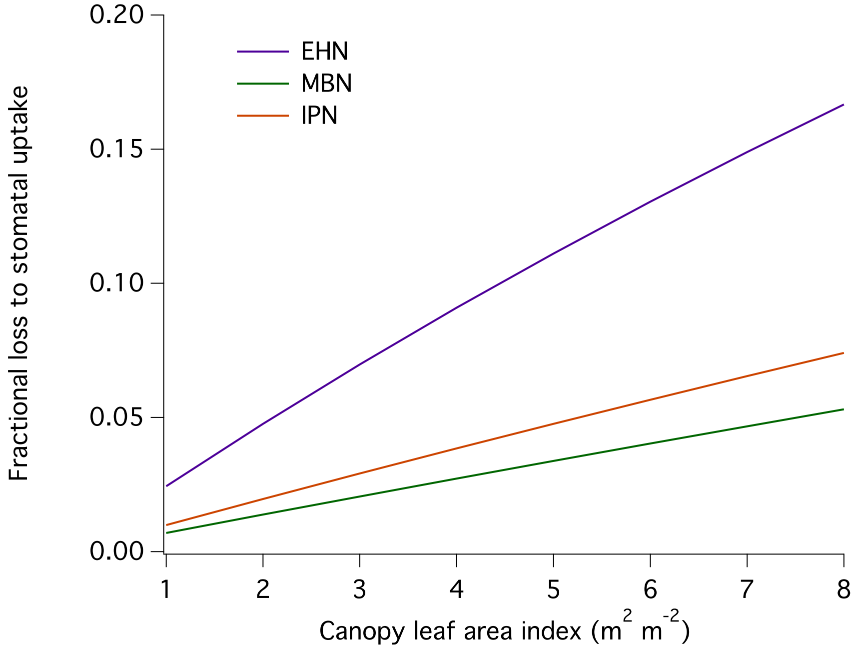

Figure 3.3: Fractional stomatal loss of IPN, MBN, EHN versus canopy leaf area index in the summertime with a boundary layer height of 1 km.

3.6 References

Abeleira, A., Sive, B., Swarthout, R. F., Fischer, E. V., Zhou, Y., and Farmer, D. K.: Seasonality, sources and sinks of C1–C5 alkyl nitrates in the Colorado Front Range, Elementa: Science of the Anthropocene, 6, https://doi.org/10.1525/elementa.299, URL https://doi.org/10.1525/elementa.299, 45, 2018.

Atlas, E.: Evidence for C_3 alkyl nitrates in rural and remote atmospheres, Nature, 331, 426–428, https://doi.org/10.1038/331426a0, 1988.

Baker, J. W. and Easty, D. M.: Hydrolysis of organic nitrates, Nature, 166, 156, https://doi.org/10.1038/166156a0, URL https://www.nature.com/articles/166156a0, 1950.

Blake, N. J., Blake, D. R., Sive, B. C., Katzenstein, A. S., Meinardi, S., Wingenter, O. W., Atlas, E. L., Flocke, F., Ridley, B. A., and Rowland, F. S.: The seasonal evolution of NMHCs and light alkyl nitrates at middle to high northern latitudes during TOPSE, Journal of Geophysical Research: Atmospheres, 108, https://doi.org/https://doi.org/10.1029/2001JD001467, URL https://agupubs.onlinelibrary.wiley.com/doi/abs/10.1029/2001JD001467, 2003.

Browne, E. C. and Cohen, R. C.: Effects of biogenic nitrate chemistry on the NO_x lifetime in remote continental regions, Atmospheric Chemistry and Physics, 12, 11 917–11 932, https://doi.org/10.5194/acp-12-11917-2012, URL https://acp.copernicus.org/articles/12/11917/2012/, 2012.

Darer, A. I., Cole-Filipiak, N. C., O'Connor, A. E., and Elrod, M. J.: Formation and Stability of Atmospherically Relevant Isoprene-Derived Organosulfates and Organonitrates, Environmental Science & Technology, 45, 1895–1902, https://doi.org/10.1021/es103797z, URL https://doi.org/10.1021/es103797z, pMID: 21291229, 2011.

Day, D. A., Wooldridge, P. J., Dillon, M. B., Thornton, J. A., and Cohen, R. C.: A thermal dissociation laser-induced fluorescence instrument for in situ detection of NO2, peroxy nitrates, alkyl nitrates, and HNO3, Journal of Geophysical Research: Atmospheres, 107, ACH 4–1–ACH 4–14, https://doi.org/https://doi.org/10.1029/2001JD000779, URL https://agupubs.onlinelibrary.wiley.com/doi/abs/10.1029/2001JD000779, 2002.

Delaria, E. R., Vieira, M., Cremieux, J., and Cohen, R. C.: Measurements of NO and NO_2 exchange between the atmosphere and *Quercus agrifolia*, Atmospheric Chemistry and Physics, 18, 14 161–14 173, https://doi.org/10.5194/acp-18-14161-2018, URL https://acp.copernicus.org/articles/18/14161/2018/, 2018.

Delaria, E. R., Place, B. K., Liu, A. X., and Cohen, R. C.: Laboratory measurements of stomatal NO_2 deposition to native California trees and the role of forests in the NO_x cycle, Atmospheric Chemistry and Physics, 20, 14 023–14 041, https://doi.org/10.5194/acp-20-14023-2020, URL https://acp.copernicus.org/articles/20/14023/2020/, 2020.

Finlayson-Pitts, B. J. and Pitts Jr., J. N.: Chemistry of the Upper and Lower Atmosphere, Academic Press, 2000.

Fisher, J. A., Jacob, D. J., Travis, K. R., Kim, P. S., Marais, E. A., Chan Miller, C., Yu, K., Zhu, L., Yantosca, R. M., Sulprizio, M. P., Mao, J., Wennberg, P. O., Crounse, J. D., Teng, A. P., Nguyen, T. B., St. Clair, J. M., Cohen, R. C., Romer, P., Nault, B. A., Wooldridge, P. J., Jimenez, J. L., Campuzano-Jost, P., Day, D. A., Hu, W., Shepson, P. B., Xiong, F., Blake, D. R., Goldstein, A. H., Misztal, P. K., Hanisco, T. F., Wolfe, G. M., Ryerson, T. B., Wisthaler, A., and Mikoviny, T.: Organic nitrate chemistry and its implications for nitrogen budgets in an isoprene- and monoterpene-rich atmosphere: constraints from aircraft ($SEAC^4RS$) and ground-based (SOAS) observations in the Southeast US, Atmospheric Chemistry and Physics, 16, 5969–5991, https://doi.org/10.5194/acp-16-5969-2016, URL https://acp.copernicus.org/articles/16/5969/2016/, 2016.

Hu, K. S., Darer, A. I., and Elrod, M. J.: Thermodynamics and kinetics of the hydrolysis of atmospherically relevant organonitrates and organosulfates, Atmospheric Chemistry and Physics, 11, 8307–8320, https://doi.org/10.5194/acp-11-8307-2011, URL https://acp.copernicus.org/articles/11/8307/2011/, 2011.

Kames, J. and Schurath, U.: Alkyl nitrates and bifunctional nitrates of atmospheric interest: Henry's law constants and their temperature dependencies, Journal of Atmospheric Chemistry, 15, 79–95, https://doi.org/10.1007/BF00053611, 1992.

Kames, J., Schweighoefer, S., and Schurath, U.: Henry's law constant and hydrolysis of peroxyacetyl nitrate (PAN), Journal of Atmospheric Chemistry, 12, 169–180, https://doi.org/10.1007/BF00115778, 1990.

Kastler, J., Jarman, W., and Ballschmiter, K.: Multifunctional organic nitrates as constituents in European and US urban photo-smog, Fresenius Journal of Analytical Chemistry, 368, 244–249, https://doi.org/10.1007/s002160000550, 2000.

Lockwood, A. L., Filley, T. R., Rhodes, D., and Shepson, P. B.: Foliar uptake of atmospheric organic nitrates, Geophysical Research Letters, 35, https://doi.org/https://doi.org/10.1029/2008GL034714, URL https://agupubs.onlinelibrary.wiley.com/doi/abs/10.1029/2008GL034714, 2008.

Nguyen, T. B., Crounse, J. D., Teng, A. P., St. Clair, J. M., Paulot, F., Wolfe, G. M., and Wennberg, P. O.: Rapid deposition of oxidized biogenic compounds to a temperate forest, Proceedings of the National Academy of Sciences, 112, E392–E401, https://doi.org/10.1073/pnas.1418702112, URL https://www.pnas.org/content/112/5/E392, 2015.

Perring, A. E., Pusede, S. E., and Cohen, R. C.: An observational perspective on the atmospheric impacts of alkyl and multifunctional nitrates on ozone and secondary organic aerosol, Chemical Reviews, 10, 5848–5870, https://doi.org/10.1021/cr300520x, 2013.

Place, B. K., Delaria, E. R., Liu, A. X., and Cohen, R. C.: Leaf Stomatal Control over Acyl Peroxynitrate Dry Deposition to Trees, ACS Earth and Space Chemistry, 4, 2162–2170, https://doi.org/10.1021/acsearthspacechem.0c00152, URL https://doi.org/10.1021/acsearthspacechem.0c00152, 2020.

Robertson, R. E., Koshy, K. M., Annessa, A., Ong, J. N., Scott, J. M. W., and Blandamer, M. J.: Kinetics of solvolysis in water of four secondary alkyl nitrates, Canadian Journal of Chemistry, 60, 1780–1785, https://doi.org/10.1139/v82-244, URL https://doi.org/10.1139/v82-244, 1982.

Romer, P. S., Duffey, K. C., Wooldridge, P. J., Allen, H. M., Ayres, B. R., Brown, S. S., Brune, W. H., Crounse, J. D., de Gouw, J., Draper, D. C., Feiner, P. A., Fry, J. L., Goldstein, A. H., Koss, A., Misztal, P. K., Nguyen, T. B., Olson, K., Teng, A. P., Wennberg, P. O., Wild, R. J., Zhang, L., and Cohen, R. C.: The lifetime of nitrogen oxides in an isoprene-dominated forest, Atmospheric Chemistry and Physics, 16, 7623–7637, https://doi.org/10.5194/acp-16-7623-2016, URL https://acp.copernicus.org/articles/16/7623/2016/, 2016.

Romer Present, P. S., Zare, A., and Cohen, R. C.: The changing role of organic nitrates in the removal and transport of NO_x, Atmospheric Chemistry and Physics, 20, 267–279, https://doi.org/10.5194/acp-20-267-2020, URL https://acp.copernicus.org/articles/20/267/2020/, 2020.

Rumble, J., ed.: Handbook of Chemistry and Physics, CRC, 2021.

Russo, R. S., Zhou, Y., Haase, K. B., Wingenter, O. W., Frinak, E. K., Mao, H., Talbot, R. W., and Sive, B. C.: Temporal variability, sources, and sinks of C_1-C_5 alkyl nitrates in coastal New England, Atmospheric Chemistry and Physics, 10, 1865–1883, https://doi.org/10.5194/acp-10-1865-2010, URL https://acp.copernicus.org/articles/10/1865/2010/, 2010.

Sander, R.: Compilation of Henry's law constants (version 4.0) for water as solvent, Atmospheric Chemistry and Physics, 15, 4399–4981, https://doi.org/10.5194/acp-15-4399-2015, URL https://acp.copernicus.org/articles/15/4399/2015/, 2015.

Sobanski, N., Thieser, J., Schuladen, J., Sauvage, C., Song, W., Williams, J., Lelieveld, J., and Crowley, J. N.: Day and night-time formation of organic nitrates at a forested mountain site in south-west Germany, Atmospheric Chemistry and Physics, 17, 4115–4130, https://doi.org/10.5194/acp-17-4115-2017, URL https://acp.copernicus.org/articles/17/4115/2017/, 2017.

Sparks, J. P., Roberts, J. M., and Monson, R. K.: The uptake of gaseous organic nitrogen by leaves: A significant global nitrogen transfer process, Geophysical Research Letters, 30, https://doi.org/https://doi.org/10.1029/2003GL018578, URL https://agupubs.onlinelibrary.wiley.com/doi/abs/10.1029/2003GL018578, 2003.

Wesely, M.: Parameterization of surface resistances to gaseous dry deposition in regional-scale numerical models, Atmospheric Environment, 23, 1293–1304, https://doi.org/10.1016/0004-6981(89)90153-4, 1989.

Zare, A., Romer, P. S., Nguyen, T., Keutsch, F. N., Skog, K., and Cohen, R. C.: A comprehensive organic nitrate chemistry: insights into the lifetime of atmospheric organic nitrates, Atmospheric Chemistry and Physics, 18, 15 419–15 436, https://doi.org/10.5194/acp-18-15419-2018, URL https://acp.copernicus.org/articles/18/15419/2018/, 2018.

3.7 Appendix

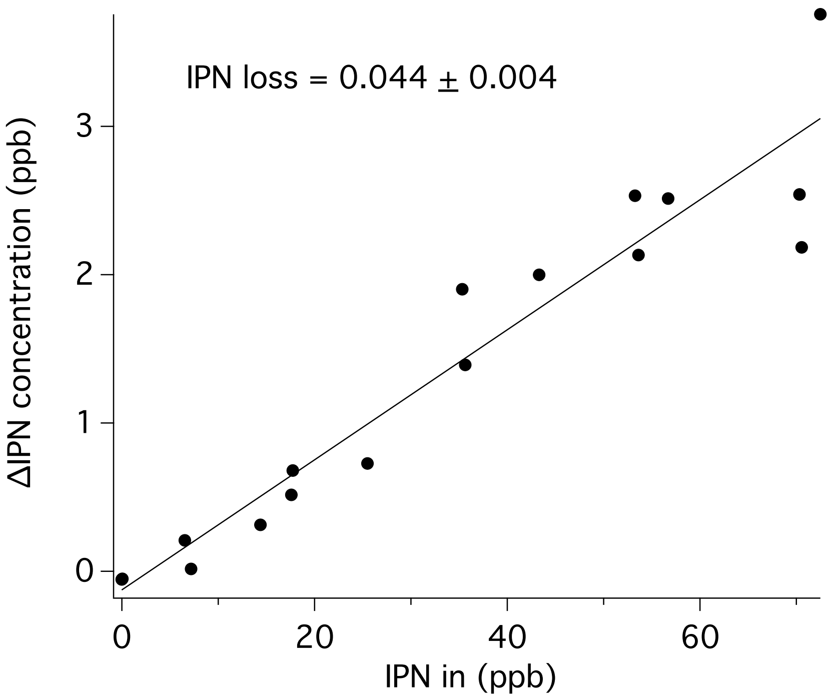

Figure 3.A1: The change in concentration of IPN plotted against the concentration of IPN entering the dynamic chamber. The slope of the line of best fit represents the wall losses of IPN to the experimental setup.

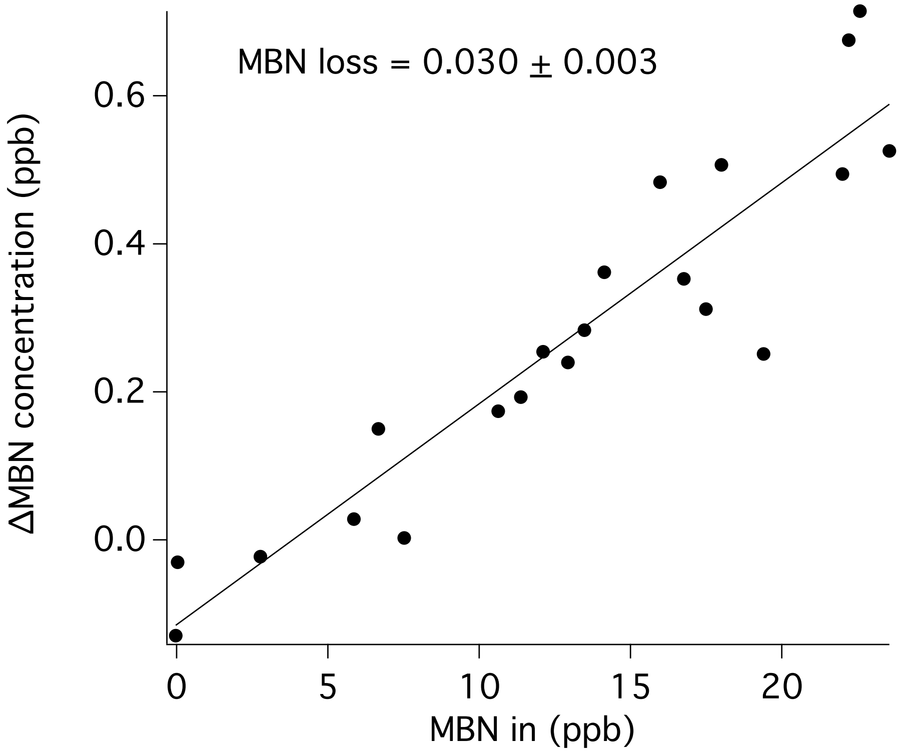

Figure 3.A2: The change in concentration of MBN plotted against the concentration of MBN entering the dynamic chamber. The slope of the line of best fit represents the wall losses of MBN to the experimental setup.

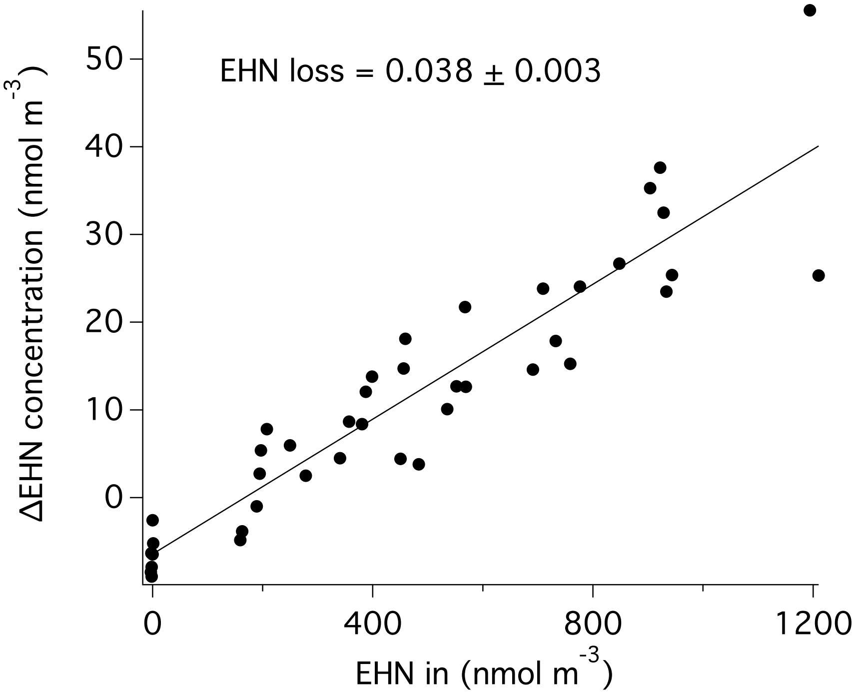

Figure 3.A3: The change in concentration of EHN plotted against the concentration of EHN entering the dynamic chamber. The slope of the line of best fit represents the wall losses of EHN to the experimental setup.

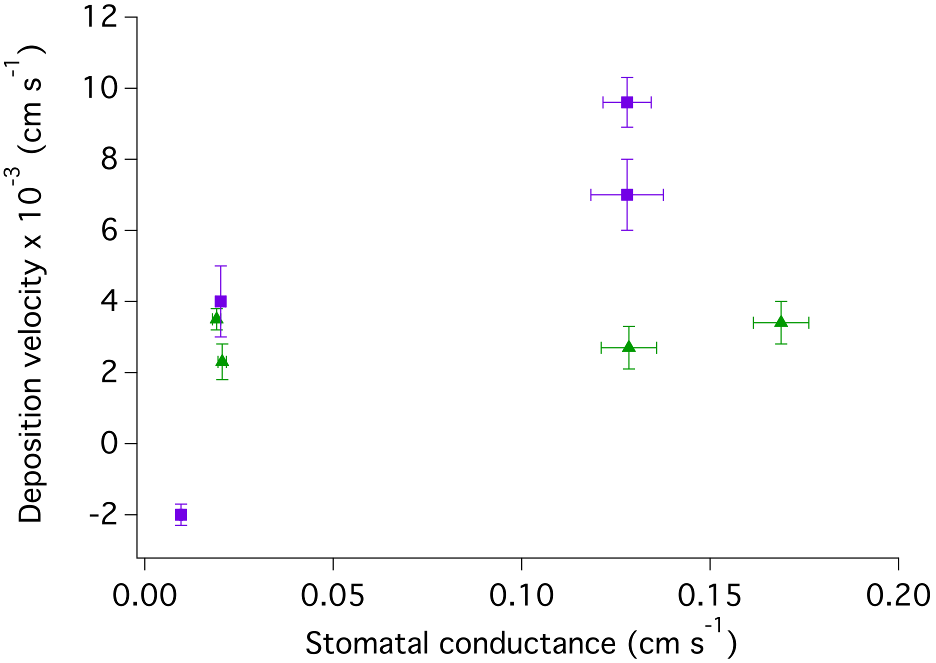

Figure 3.A4: Relationship between the observed deposition velocities of MBN (green traces) and EHN (purple traces) to *Quercus douglasii* and average measured leaf stomatal conductance across all experiments.

Chapter 4

Application of a canopy conductance model towards nitrogen oxide deposition

Adapted from B. K. Place and E. R. Delaria et al., Development of a solar induced fluorescence-canopy conductance model and its application to stomatal reactive nitrogen deposition, *ACS Earth Space Chem.*, accepted.

4.1 Abstract

The bi-directional exchange of gases between vegetation and the atmosphere is controlled by a variety of environmental factors and feedbacks that are entangled and difficult to quantify. As a result of this complexity, parameterizations of canopy conductance (G_c) in atmospheric models introduce large uncertainties and likely biases into representations of atmosphere-biosphere gas exchange. We present a novel representation of canopy conductance derived from measurements of solar-induced fluorescence (SIF) from the TROPOspheric Monitoring Instrument (TROPOMI). We show a strong linear correlation between GPP and G_c–calculated using Pennman-Monteith theory–across a variety of ecosystem types in the AmeriFlux network. We couple this G_c-GPP correlation to previous research showing a strong linear correlation between SIF and GPP and estimate G_c at a 500 m spatial resolution across the continental United States. We also combine our model with surface estimates of NO_2 and PAN from WRF-Chem to estimate stomatal deposition fluxes of these gases. Our results suggest that satellite measurements of solar-induced fluorescence can provide important constraints on model representations of stomatal activity and canopy gas exchange on regional and global scales.

4.2 Introduction

The exchange of gases between the atmosphere and biosphere plays a fundamental role in determining the composition of the atmosphere. At the same time, changes in atmospheric composition and climate provide important feedbacks that affect biological communities. This dynamic interaction between the atmosphere and biosphere is best exemplified by photosynthesis, which contributes one of the largest sinks of CO_2 for our atmosphere (IPCC, 2013). The simultaneous release of water vapor through transpiration also influences the water cycle and climate. Transpiration may return approximately 40% of incident precipitation back to the atmosphere, which in turn encourages later precipitation events (Schlesinger and Jasechko, 2014).

Transpiration takes place when water evaporates from the open stomata of leaves. This generally occurs in the presence of light to allow for the uptake of CO_2 during photosynthesis (Cowan, 1978; Green, 1993; Tuzet et al., 2003). Stomatal conductance thus plays a fundamental role in both the carbon and water cycles (Miner and Bauerle, 2017). During stomatal opening, other atmospheric gases–including ozone (O_3), reactive nitrogen (N_r) and volatile organic compounds (VOCs)–also diffuse in and out of plant leaves, affecting other chemical cycles (Delaria et al., 2020; Place et al., 2020; Guenther et al., 2012; Saunois et al., 2016; Huang et al., 2017; Emberson et al., 2000; Clifton et al., 2020). In particular, the canopy reduction of soil-emitted nitrogen has shown to have a major influence on the nitrogen cycle (Yienger and Levy, 1995; Lerdau et al., 2000; Delaria and Cohen, 2020).

Since the stomatal exchange of trace gases has a substantial impact on atmospheric composition, the accurate representation of the stomatal conductance (g_s) in atmospheric models is essential (Kavassalis and Murphy, 2017; Delaria and Cohen, 2020). However, stomatal conductance is influenced by a variety of environmental factors (e.g. vapor pressure, soil water potential, light availability, CO_2, O_3, and season), making it difficult to include a fully mechanistic description in models (Emberson et al., 2000; Delaria and Cohen, 2020; Tuzet et al., 2003; Gunderson et al., 2002; Altimir et al., 2004; Hardacre et al., 2015). This is further complicated by diverse species-specific responses to these environmental factors. As a result, model representations of g_s are very complex and heavily parameterized, leading to a large degree of variability in representations of atmosphere-biosphere exchange of trace gases (Altimir et al., 2004; Medlyn et al., 2011; Bonan et al., 2014). As stomatal emission and uptake is a major term in the budgets of many trace gases, this lack of clarity limits our understanding of atmospheric composition.

The canopy conductance (G_c) can be thought of as the integrated sum of the stomatal conductance over all the leaves in the canopy. In the last two decades, remote sensing has become a valuable tool for estimating both G_c and evapotranspiration fluxes over large spatial scales (Cleugh et al., 2007; Kalma et al., 2008; Moran and Jackson, 1991; Shan et al., 2019; Glenn et al., 2010, 2011a,b; Yebra et al., 2012; Barraza et al., 2015; Shan et al., 2021; Maes et al., 2020). For example, Yebra *et al.* (2012) found that the normalized difference vegetation index (NDVI), enhanced vegetation index (EVI), and normalized difference water index (NDWI) could explain 80 percent of the variance between the respective VI and G_c

at 16 FLUXNET sites (Yebra et al., 2012). More recent studies have shown that retrievals of solar-induced fluorescence (SIF) from GOME-2 and TROPOMI can be used as a strong predictor of site-level and ecosystem-level G_c (Shan et al., 2019, 2021; Maes et al., 2020). Maes *et al.* (2020)(Maes et al., 2020) demonstrate that the G_c-SIF response may be universal across most ecosystem types.

Here we present an empirical relationship between SIF retrievals from the TROPOspheric Monitoring Instrument (TROPOMI) and G_c determined from the AmeriFlux network. The TROPOMI SIF retrievals we use are at a 500 m resolution–the highest resolution SIF dataset available from satellite measurements. We show that a coupled SIF-GPP-G_c model can be used to estimate G_c across the continental United States (CONUS) during the 2018 growing season. A potential application of this model is to estimate the stomatal deposition of reactive nitrogen and the resulting impacts on the nitrogen cycle. Stomatal conductance has been shown to be the limiting factor in the deposition of NO_2 and peroxyacetyl nitrate (PAN). As such, the deposition of NO_2 and PAN scales linearly with stomatal conductance (Delaria et al., 2020; Place et al., 2020). Rates of deposition are rapid enough to affect the lifetimes of NO_x and PAN by more than 10%, making an accurate description of this pathway for removal essential to the understanding of tropospheric chemistry. With G_c inferred from remote sensing, the dry deposition flux of these important atmospheric trace gases can be constrained through measurements of their ambient concentrations and the canopy conductance (G_c). To assess spatial and temporal patterns in dry deposition of NO_x and PAN, we couple our SIF-GPP-G_c model with a chemical transport model to estimate the dry deposition of NO_2 and PAN over the continental United States.

4.3 Methods

4.3.1 CO_2 flux data

Half-hourly surface energy flux, meteorological, and CO_2 fluxes and products were collected from the AmeriFlux website (https://AmeriFlux.lbl.gov/data/download-data/). A total of 154 sites across the continental United States (CONUS) contained measurements of the variables needed to carry out the study (see Section 4.3.2). The final flux data set encompassed the following land cover classes - Deciduous broadleaf forests (DBF; 18 sites), Evergreen needleleaf forests (ENF; 34 sites), Mixed forests (MF; 7 sites), Croplands (CRO; 27 sites), Grasslands (GRA; 30 sites), Open and closed shrublands (SHR; 21 sites), and Wetlands (WET; 17 sites). Figure 4.1 shows the geographic distribution and land type of all the sites used.

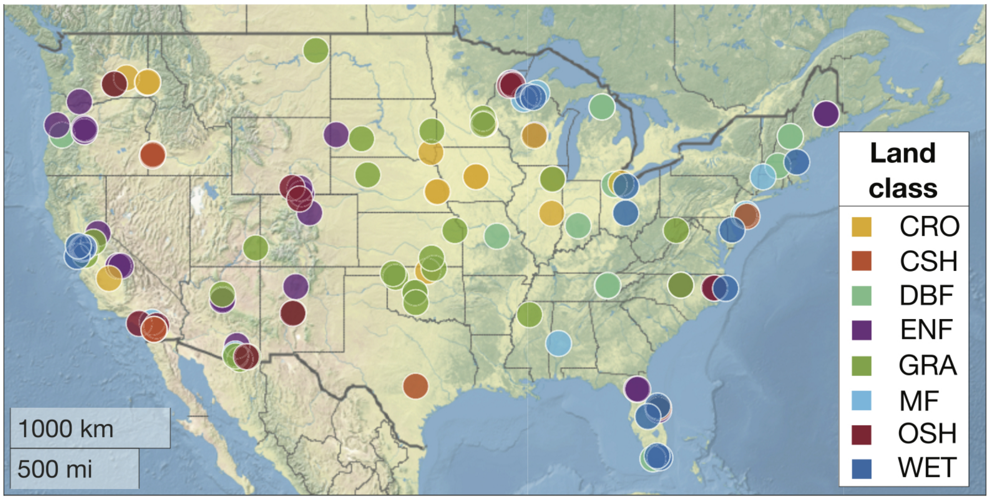

Figure 4.1: Location and IGBP land class of all the AmeriFlux sites across CONUS used to carry out the study.

4.3.2 Calculations of canopy conductance (G_c) and gross primary productivity (GPP)

Canopy conductance (G_c) was calculated at each site at the time of TROMOPI overpass (LT 13:30) using the inverted Penman-Monteith equation (Eq. 4.1), which uses a surface energy flux and mass balance approach to estimate surface conductance (Monteith, 1965). The Penman-Monteith equation estimates G_c using measurements or calculations of the net radiation flux (R_n), the soil heat flux (G), the latent energy flux (LE), air density (ρ_a), specific heat capacity of air (C_p), vapor pressure deficit (δ_e), conductivity of air (g_a), the slope of the saturated vapor pressure curve (Δ), and the psychometric constant (γ).

$$\frac{1}{G_c} = \frac{\Delta(R_n - G) + \rho_a C_p \delta_e g_a - \Delta LE - \gamma LE}{\gamma g_a LE} \tag{4.1}$$

Measurements of R_n, G and LE were provided directly from each of the sites. In instances where one of the three fluxes was not reported, the sensible heat flux (H) was used to calculate the missing flux through the surface flux balance relationship (Eq. 4.2). Measurements of temperature (T), pressure (P) and relative humidity (RH) were used to calculate ρ_a, γ, δ_e, and Δ via Equations 4.3 - 4.6.

$$R_n - G - H - LE = 0 \tag{4.2}$$

$$\rho_a = \frac{1000P}{287.058(T + 273.15)} \tag{4.3}$$

$$\gamma = 0.66P \tag{4.4}$$

$$\delta_e = (1 - RH)0.61121e^{(18.678 - \frac{T}{234.5})(\frac{T}{257.14+T})} \tag{4.5}$$

$$\Delta = \frac{\partial \delta_e}{\partial T} \tag{4.6}$$

Measurement height (z), displacement height (d), roughness length to momentum transfer (z_{om}), roughness length to heat transfer (z_{oh}), von Karman's constant (k) and wind speed (U) were used to determine g_a through equation 4.7.The values of d, $z_o m$, and $z_o h$ were estimated as 0.66h, 0.123h and 0.0123h, respectively, where h represents the canopy height. Stability corrections using measurements of air and surface temperature were also performed on equation 7 following recommended factors by Monteith (1973) and Hatfield et al. (1983)(Monteith, 1973; Liu et al., 2006). The stability corrected G_c values differed from the original G_c values on average by less than 2% (Figure 4.A1). Since the method showed low sensitivity to the calculation of g_a and only half of the total AMERIFLUX sites used in the analysis report surface temperature measurements, the calculation of G_c was carried forward without the use of stability corrected g_a values.

$$\frac{1}{g_a} = \frac{\ln\frac{z-d}{z_{om}} \ln\frac{z-d}{z_{oh}}}{k^2 U} \tag{4.7}$$

The Penman-Monteith derivation of G_c encompasses both transpiration and evaporation processes. We applied a precipitation filter to remove days where surface evaporation may have contributed measurably towards the total surface conductance. The filter removed any 7-day period where the amount of precipitation exceeded the 90th percentile of the data set on the first day of the screened period. An interquartile range outlier test was then applied to the screened G_c data set.

It should be noted that recent studies have suggested that the inverted Penman-Monteith derivation of G_c introduces uncertainties due to energy imbalance (i.e. $R_n - G - H - LE \neq 0$) (Leuning et al., 2012; Wehr and Saleska, 2021; Hu et al., 2021). However, Penman-Monteith is still the most commonly used method for deriving G_c from surface energy and water vapor fluxes (Shan et al., 2019, 2021; Maes et al., 2020; Damm et al., 2021). The effect of energy imbalance is also likely to be minimal in our work, as energy imbalance is lesser in the afternoon (during the time of TROPOMI overpass) (Hu et al., 2021).

Gross Primary Production (GPP) measurements were obtained directly from each site or calculated using measurements of Net Ecosystem Exchange (NEE) and Ecosystem Respiration (RECO). At sites that did not partition NEE to GPP and RECO, we estimated GPP by equating average nighttime CO_2 fluxes to RECO and subtracting this from daytime CO_2 fluxes: $\text{GPP} = \text{NEE} - \text{NEE}_{\text{night}}$ (Reichstein et al., 2005).

To correspond with TROPOMI's early afternoon overpass time, G_c and GPP were aggregated into daily midday estimates by taking the median values between 12:30 and 14:30 local time each day. Final smoothed data sets were produced by calculating a 14-day moving average of G_c and GPP.

4.3.3 Observations of solar-induced chlorophyll fluorescence from TROPOMI

We use observations of SIF from the TROPOMI instrument on the Sentinel-5P satellite (Veefkind et al., 2012). Briefly, TROPOMI is a nadir-viewing imaging spectrometer in a 16-day sun-synchronous orbit with bands in the UV, visible, and near-infrared. The TROPOMI ground swath is 2600 km across track and the nadir footprint size is 5.6 km along-track and 3.5 km across track. SIF retrievals are made over a small window in the far red at 740 nm. Köhler *et al.*(Köhler et al., 2018) developed the first retrievals of SIF from TROPOMI. We use the 500 m downscaled SIF data described by Turner *et al.*(Turner et al., 2020, 2021). Turner *et al.*(Turner et al., 2020, 2021) used data from multiple viewing geometries to obtain higher resolution than the native TROPOMI footprint size and then further downscaled the SIF using a sub-grid weighting based on high resolution observations of vegetation from the Moderate Resolution Imaging Spectroradiometer (MODIS). The end result is a 500-m daily estimate of SIF that represents a 16-day moving average. Turner *et al.*(Turner et al., 2020, 2021) also observed a linear relationship between early afternoon GPP data from AmeriFlux sites and coincident observations of SIF from TROPOMI.

4.3.4 Chemical Transport Model simulations

The Weather Research and Forecast Model coupled with chemistry (WRF-Chem) version 3.5.1 was used to simulate hourly surface NO_2 and PAN concentrations and meteorology. Simulations encompassed the CONUS domain with a horizontal resolution of 12x12 km and 29 vertical layers. The simulation period was February 2018 to February 2019. A customized version of the Regional Atmospheric Chemistry Mechanism version 2 (RACM2) was employed to model the chemistry, the details are described in Zare et al. (2018). The North American Regional Reanalysis (NARR) provides initial meteorological and boundary conditions and was nudged every 3 hours to constrain the meteorological fields. The chemical initial and boundary conditions were constrained by The Community Atmosphere Model with Chemistry (CAM-chem(Buchholz et al.; Emmons et al., 2020)). The Model of Emissions of Gases and Aerosols from Nature (MEGAN) was used to determine the biogenic emissions, and the National Emissions Inventory 2011 (NEI 11) was used to describe anthropogenic emissions. To account for the annual emission reduction, an additional scaling factor was applied to scale the total emission to the reported emission at model year from the United States Environmental Protection Agency (EPA, 2016).

We also use the GEOS-Chem chemical transport model (v12.7.0) to compare fluxes and deposition velocities of NO_2 and PAN. The GEOS-Chem model used is driven by the assimilated meteorological fields from the Goddard Earth Observation System Forward Processing products (GEOS-FP) at $0.25° \times 0.3125°$spatial resolution. We conduct nested GEOS-Chem simulations over North America (10°N – 70°N, 140°W - 40°W) for summer 2018. The boundary conditions are generated from a global simulation at $2° \times 2.5°$resolution with a 1-year spin-up. We use the standard tropospheric chemical scheme that includes detailed NO_x-

hydrocarbon-aerosol chemistry as described in Travis et al. (2016) and Fisher et al. (2016). The NEI2011 inventory is used for U.S. anthropogenic emissions, and scaled to 2018 level based on the national emission trends (EPA, 2018).

4.4 Development of a coupled G_c-GPP-SIF model

Previous works by Shan et al. (2019) and Maes et al. (2020) have shown that SIF retrievals from the GOME-2 instruments onboard the EUMETSAT's MetOp series satellites are strongly correlated with G_c (Shan et al., 2019; Maes et al., 2020). Retrievals from TROPOMI (Sentinel-5P satellite) were also used more recently to probe the G_c-SIF relationship (Shan et al., 2021). The authors of this study found a strong correlation between these variables across three different field sites (Shan et al., 2021). The goal of the current work is to build on these bodies of work and determine an empirical relationship between SIF retrievals from TROPOMI and G_c across a wide range of ecosystem types and locations. Initially, we explored a direct SIF-G_c relationship. However, limited measurements of the parameters necessary for calculation of G_c across the AmeriFlux network that coincided with TROPOMI's measurement period (2018-2020) made it difficult to accurately describe the relationship. In order to provide better spatial coverage and to better capture the SIF-G_c response in a variety of ecosystems, we correlated G_c and SIF (a proxy for GPP) indirectly through GPP with multi-year measurements across the AmeriFlux network. The validity of this approach is demonstrated in Figure 4.A2, which shows direct correlations of SIF and G_c, SIF and GPP, and GPP and G_c using the limited measurements from AmeriFlux sites that coincided with TROPOMI's active period.

The theory and methods behind the TROPOMI SIF-GPP relationship used in this work are provided in Turner et al. (2021). The focus of the current work is to establish a quantitative relationship between SIF and G_c from the linear correlations between SIF and GPP and GPP and G_c. The linear correlation between GPP and SIF has been discussed in a number of recent publications (Turner et al., 2020, 2021; Magney et al., 2019; He et al., 2020). There has, however, been some evidence that there is divergence between GPP and SIF at the leaf-level under low light intensities and certain environmental conditions (Marrs et al., 2020; Maguire et al., 2020). Recently, Magney et al. (2020) highlighted that a linear relationship between GPP and SIF is expected at high light levels under conditions of both stressed and non-stressed leaves and sunlit and shaded leaves. These high light levels are characteristic of the early afternoon during the time of TROPOMI overpass and SIF observations. This potentially explains why SIF and GPP are strongly correlated when using space-borne measurements, yet decouple at sub-diurnal scales using surface measurements.

4.4.1 Covariation of GPP and G_c at Ameriflux sites

Leaf-level studies have shown that stomatal conductance to water vapor and CO_2 assimilation are strongly correlated (Ball J. T., 1988; Leuning, 1990; Collatz et al., 1992; Leuning,

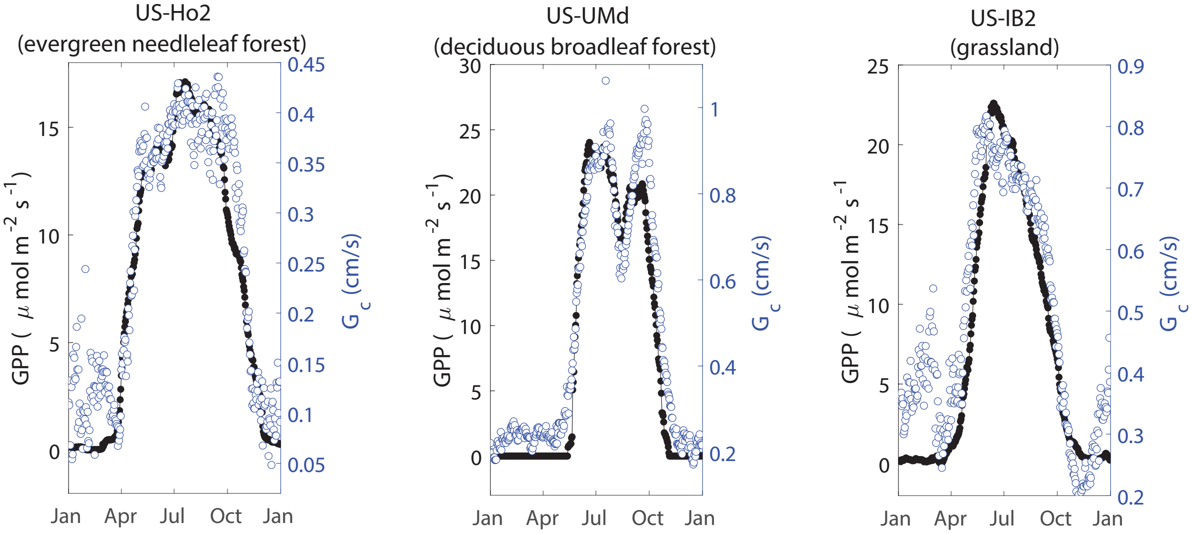

Figure 4.2: Gross primary productivity (GPP, black closed circles) and canopy conductance (G_c, open blue circles) averaged by day of year over the data record for three representative AmeriFlux sites

1995). This empirical relationship is typically described through the Ball-Berry (BB) model (Equation 4.8), where g_s is the stomatal conductance to water vapor, A^* is the CO_2 assimilation rate or leaf photosynthesis rate adjusted for environmental variables, m is the Ball-Berry parameter and slope of best fit, and g_0 is the minimum stomatal conductance intercept (Ball J. T., 1988).

$$g_s = mA^* + g_0 \tag{4.8}$$

Field measurements have shown that the Ball-Berry model may be extended to the canopy-level and can be used as a good predictor of canopy conductance and canopy CO_2 assimilation (Lai et al., 2000; Valentini et al., 1995; Wolf et al., 2006; Launiainen et al., 2011; Ono et al., 2013). Under the big leaf model framework (ie. treating a canopy as one big leaf), g_s and A^* may be replaced by G_c and GPP, respectively, in Eq. 4.8 assuming there is little contribution from canopy morphology and that the slope of the response is insensitive to changes in environmental variables (Sellers et al., 1992; Shan et al., 2019). Following these assumptions, one would anticipate a linear relationship between GPP and G_c.

Figure 4.2 shows a multi-year average time series of GPP and G_c for select evergreen needleleaf, decidous broadleaf and grassland AmeriFlux sites. This figure demonstrates that GPP and G_c correlate well (R = 0.68 - 0.81) with one another during the growing season (April—October) at the three sites. Subtle changes in CO_2 assimilation over the growing season, such as the average increase in GPP seen in June at US-Ho2 and the decrease in GPP during August at US-UMd, are captured in the G_c model. A higher degree of variability around zero GPP was observed during the winter months (November—March) at these sites and also across the entire Ameriflux network. The highly variable wintertime G_c calculations are likely artifacts and represent surface evaporation fluxes instead of transpiration fluxes during this time period. This hypothesis is supported by measurements of low leaf area indices across the AmeriFlux network during winter months (Fig. 4.A3). Subsequently, all site flux data was screened using a solar zenith angle of 35 degrees to eliminate contributions from the winter months in order to more accurately assess the GPP-G_c relationship during the growing season.

In general, we observe moderate-high linear correlations between GPP and G_c at individual AmeriFlux sites during the growing season (Fig. 4.3). The average correlation coefficient (R) across all sites was determined to be 0.7 ± 0.2. The strongest site-level GPP-G_c relationships and the lowest average variance was observed in cropland ecosystems ($R = 0.74 \pm 0.09$). The weakest correlations and highest average variance was observed at the wetland sites (average correlation $= 0.5 \pm 0.3$). The higher average correlations observed at the cropland sites may be a consequence of the Penman-Monteith G_c model being optimized for agricultural systems. The weaker GPP-G_c correlations determined at the wetland sites were likely driven by the contribution of evaporation fluxes to the estimated G_c fluxes.

The correlations we report are of the same magnitude as other studies (R = 0.68—0.94) that investigated correlations between canopy-scale g_s and A^* (Valentini et al., 1995; Ono et al., 2013; Launiainen et al., 2011). Observed correlations in the previous studies were typically higher because A^* values were adjusted using measurements of ambient [CO_2] and [H_2O] prior to the correlations in order to better represent the g_s-A^* relationship through the Ball-Berry model. It has also been recommended to adjust A^* by relative humidity, a CO_2 compensation point, vapor pressure deficit (VPD) and a stomatal optimization constant, to better capture the g_s-A^* relationship (Ball J. T., 1988; Leuning, 1990, 1995; Collatz et al., 1992; Medlyn et al., 2011). Adjustment of our model with measurements of VPD did lead to improvements in the correlation between GPP and G_c at most sites. However, for the purpose of our investigation we opted to not adjust the reported GPP-G_c model with VPD and other environmental variables to avoid further complexity in the model. Our unadjusted GPP-G_c model demonstrated reasonable efficacy across sites as GPP generally explained over 60% of the variability in G_c.

4.4.2 Ecosystem-level relationships between G_c and GPP

The strong linear correlations that we determined between the multi-year GPP and G_c data sets at the 154 AmeriFlux sites (Fig. 4.3) suggest that the GPP-G_c relationship can be sufficiently described using a linear relationship at the site-level. To test whether unique GPP-G_c relationships existed at the ecosystem-level, the sites were grouped by ecosystem type for further analysis. Mixed forest sites were not carried forward in the ecosystem-level analysis due to the limited number of mixed forest sites in the dataset (N=7) and the likelihood that the GPP-G_c relationship was captured in the analysis of other forested sites. Figure 4.4 shows the slopes of the lines of best fit forced through a zero intercept for the GPP-G_c relationship across all sites for each ecosystem type. The slopes determined

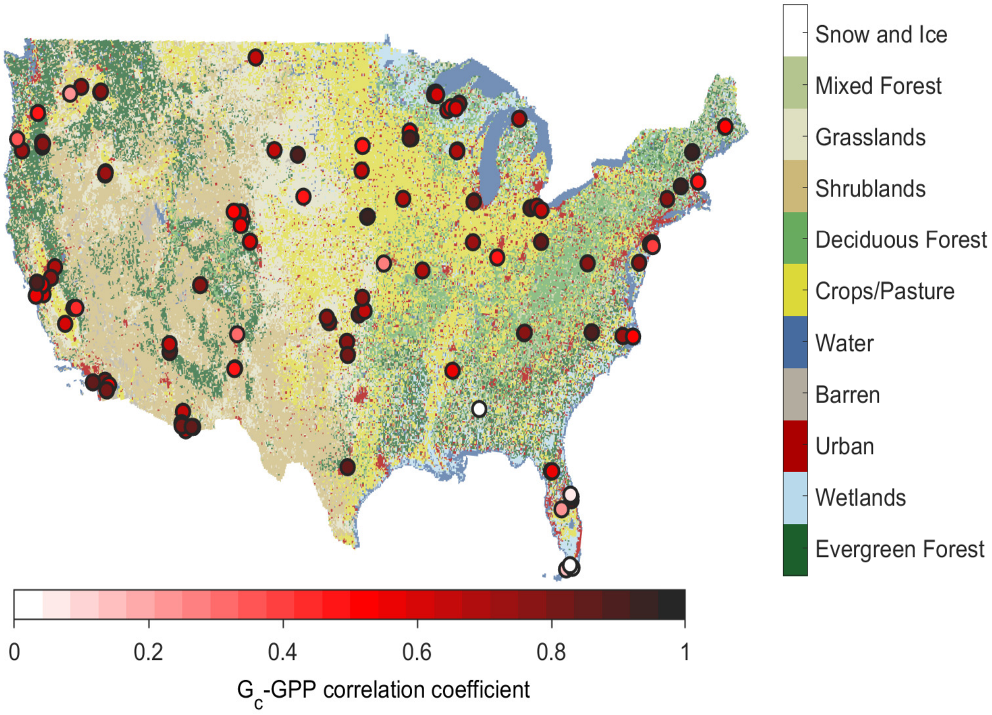

Figure 4.3: Landcover types over the continental United States from the National Land Cover Database (NLCD) and AmeriFlux site locations (circles). AmeriFlux sites are colored by the correlation coefficient for the canopy conductance (G_c)-gross primary productivity (GPP) relationship.

from these lines of best fit ranged from 0.026—0.047 [(cm s^{-1} H_2O)(μ mol^{-1} CO_2 m^2 s)] and correlations ranged from 0.48—0.86 between ecosystems. Wetland ecosystems had the highest slope and poorest correlation, which was likely driven by the influence of surface water evaporation. The GPP-G_c response was the smallest in the cropland ecosystems and the cropland sites seemed to exhibit a lower correlation at the ecosystem-level than at the site-level. The lower slope observed in the crop GPP-G_c relationship seems to be driven by sites that showed very high CO_2 assimilation. High levels of GPP could be indicative of an environment with elevated CO_2 levels, which have shown to cause deviations from linearity in the Ball-Berry relationship (Miner et al., 2017). A histogram showing the distribution of all GPP/G_c ratios that we calculated using our method can be found in Figure 4.A4. We did not identify any statistical evidence that the GPP-G_c relationship was distinct for different ecosystems. Figure 4.4 shows the line of best fit through all the GPP and G_c flux data. An overall slope of 0.036 [(cm s^{-1} H_2O)(μ mol^{-1} CO_2 m^2 s)] and a linear correlation of 0.76 was determined from the line of best fit through all ecosystem-level data.

Although the Ball-Berry model (Eq. 4.8) suggests a minimum conductance intercept (g_0), we conducted the ecosystem-level analysis under the assumption $g_0 = 0$. In practice,

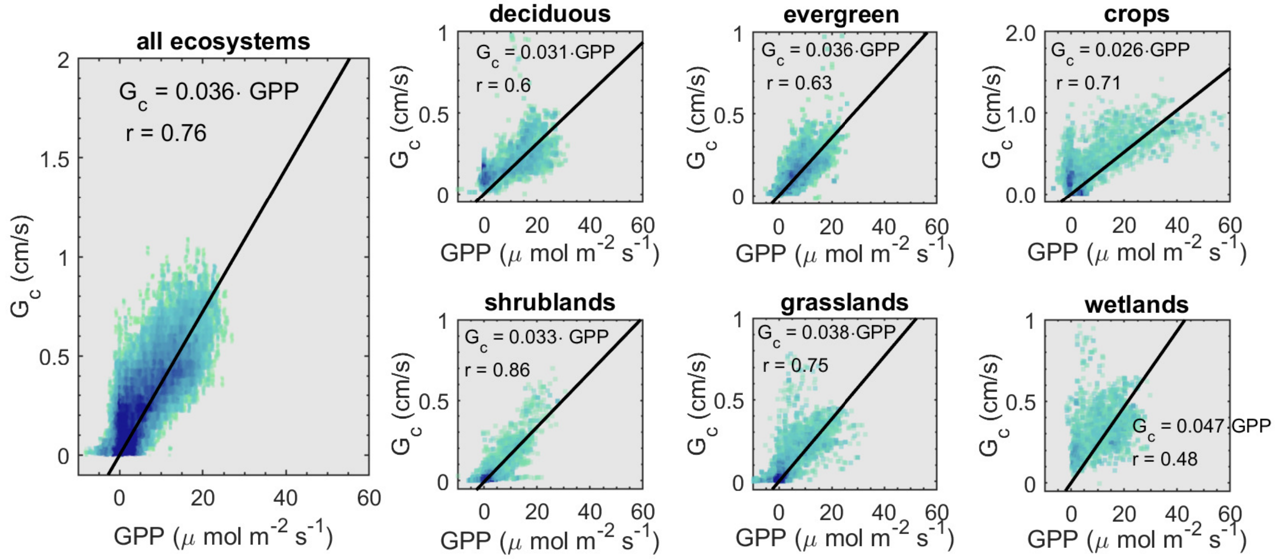

Figure 4.4: The canopy conductance-gross primary productivity (GPP) relationship for six ecosystem types and all sites combined as identified by the International Geosphere–Biosphere Programme (IGBP) classification. Open and closed shrublands are combined to one shrubland land type. IGBP classes (e.g. evergreen broadleaf, mixed forest, and woody savanna) were excluded if fewer than six sites of the class had available data. These sites were included in the plot for all ecosystems. Data are colored by density. Black lines show the linear G_c-GPP relationship fitted with a bisquare regression. Slopes and correlation coefficients are identified on each plot.

this was enforced through a linear regression with no intercept term. This assumption was justified by examining site-level fits of the G_c-GPP relationship using data from all months of the year. The solar zenith angle filter was not applied for this analysis, as some sites did not have sufficient variation in GPP after applying the filter to calculate a statistically significant intercept. The median intercepts (g_0) from all sites of a certain ecosystem type were substantially larger than the nighttime canopy conductance, when PAR and GPP are both zero (see Table 4.A1). We attribute a larger fitted intercept than the nighttime canopy conductance to a larger contribution from surface evaporation, rather than transpiration, during the wintertime. As such, the intercepts identified by the model are likely representative of stomatal and non-stomatal factors. This is particularly evident at sites such as US-UMd (Fig. 4.2), where there is a non-zero winter canopy conductance, despite this being a deciduous forest that would have a very low LAI during the winter. Further, the Ball-Berry parameters g_0 and m have been found to have a seasonal dependence in some species (Miner et al., 2017). The g_s-A^* relationship has also been shown to be non-linear at very low light intensities, resulting in differences between g_0 derived via linear regression and g_0 measured during the nighttime (Barnard and Bauerle, 2013). The SIF-GPP relationship is also known to have non-linearities at low light intensities (Magney et al., 2020). Our goal is to offer constraints on stomatal activity using satellite SIF measurements, which is likely to be more significant and more accurate at higher light levels and LAI, and we therefore prioritize prediction of G_c during the growing season. To support this claim we carried forward an ecosystem-wide intercept from the line of best fit in the calculation of NO_2 deposition fluxes (See sect 4.6.2 for additional details) for the months of January and June 2018 (Figures 4.A6 and 4.A7). These figures support the idea that NO_2 flux estimates would be elevated in areas of low leaf cover (LAI < 2 m^{-2} m^2), particularly in the wintertime, with the inclusion of an intercept. The estimated fluxes also exhibit little variation in fluxes ($<10\%$) in areas of high leaf area (LAI > 2 m^{-2} m^2) during the summertime when an intercept is considered in the model.

In a recent review of leaf-level studies exploring the g_s-A^* relationship, Miner *et al.* (2017) also describe that the Ball-Berry parameter (m) can vary under differing environmental conditions (eg. Drought-stress, elevated CO_2 levels) and that the Ball-Berry parameter has also been shown to differ across plant species. However, the ecosystem-level fits we present in Figure 4.4 show that on average the GPP-G_c relationship converges to a single slope across all ecosystems. Based on these findings we carried a scaling factor of 0.036 forward to describe the GPP-G_c relationship for all ecosystems.

4.5 Modeling G_c with TROPOMI SIF

Combining our observations that shows G_c scales linearly with GPP with previous research that show SIF scales linearly with GPP, we propose: $G_c \propto$ SIF. The final G_c-SIF relationship we determine is shown in Equation 4.9, where β is an ecosystem-specific scaling factor to convert SIF to GPP. β is derived from the SIF-GPP relationship inferred from comparison with AmeriFlux GPP, multiplied by the fraction of the grid cell represented by ecosystem type. The reader is directed to Turner et al. (2021) for a more complete description of β (Turner et al., 2021).

$$G_c = 0.036 * \beta * SIF \tag{4.9}$$

Equation 4.9 gives an estimate of G_c during TROPOMI's overpass time (approximately 13:30 local time). Monthly averaged 13:30 LT G_c values for the months of April, June and August 2018 across CONUS are presented in Figure 4.5 and the annual 2018 average can be found in the supplement (Fig. S5). The SIF-G_c model captures both the onset and decline of the growing season as the months progress from April to August. Biological activity (ie. G_c and GPP) was seen to be much higher in the east than the west. This general observation is consistent with other studies that have estimated G_c and GPP across CONUS (Yebra et al., 2012; Turner et al., 2021; Baker et al., 2010). Fine features such as the California Central Valley agricultural region and the Corn Belt in the Midwest can also be seen in Figure 4.5. A G_c range of 0—2 cm s^{-1} was determined by the SIF-G_c model across CONUS. These G_c predictions fell well within the range of observations across the AmeriFlux network.

To demonstrate the model's robustness we tested how the G_c model would respond to the use of a single scaling factor for all ecosystems versus ecosystem-specific scaling factors,

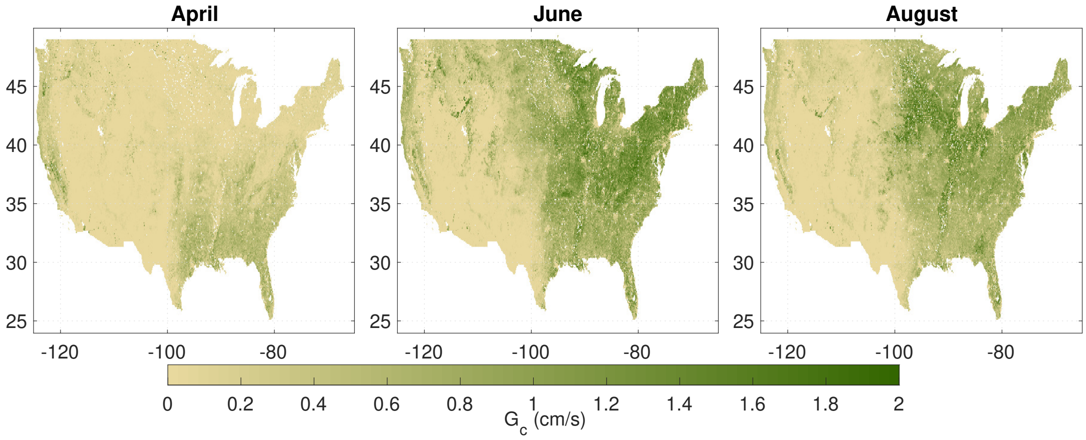

Figure 4.5: Monthly averaged canopy conductances (G_c) derived from TROPOMI SIF measurements for the months of April (left), June (middle) and August (right) of 2018. G_c averages are at time of TROPOMI overpass (13:30 LT).

and to an exponential vs linear model fit. An exponential fit was chosen for the sensitivity analysis to reflect the non-linearities that have been reported at high and low levels of GPP in the G_c-GPP relationship(Barnard and Bauerle, 2013; Miner et al., 2017). For the first sensitivity analysis we show the difference between 2018 averaged G_c across CONUS using a factor of 0.036 versus ecosystem-specific slopes determined from Figure 4.4 in Figure 4.A8. We observe approximately a 10% decrease in Gc and NO_2 fluxes (see section 4.6.2) in crop regions and an increase of approximately 20% in wetlands regions (Fig. 4.A8). The slopes for mixed forests, deciduous broadleaf forests, evergreen needleleaf forests, grasslands, and shrublands differ by less than 10%. For the second sensitivity test we show the difference between 2018 averaged G_c and calculated NO_2 fluxes when using an exponential fit in place of a linear fit in Figure 4.A9. Percentage changes in G_c of up to 20% were observed in some regions, however in regions of high leaf cover G_c was seen to vary by 10% or less. The percent changes in annual NO_2 estimated fluxes were also typically less than 10%. All of these variances from the linear model are small compared to the difference between our proposed model and the predominant models describing N fluxes (Fig. 4.6, 4.7, 4.A10).

Stomatal activity is typically modeled as a function of light intensity and temperature using the formulation of Wesely (1989) in many atmospheric chemical transport models (CTMs) (e.g. WRF-Chem, GEOS-Chem)wesely89. Additional considerations of vapor pressure deficit and soil water availability have been demonstrated to substantially improve estimates of ozone, carbon, and water atmosphere-biosphere exchange (Kavassalis and Murphy, 2017; Emberson et al., 2000; Knauer et al., 2015; Kennedy et al., 2019). However, these parameterizations fail to adequately represent the impact of drought on stomatal behavior. Approaches have also been described that represent stomatal conductance and transpiration by considering water use efficiency and water transport along the soil, plant, and atmosphere continuum (Bonan et al., 2014; Kennedy et al., 2019). These considerations have provided improved representations of stomatal behavior from a physiological and mechanistic perspective, but are typically heavily parameterized and require inputs of many plant, soil, and meteorological measurements. Another common approach to modeling stomatal conductance is through the coupling of the Farquhar photosynthesis model with the Ball-Berry model (Ball J. T., 1988). This approach requires knowledge of the maximum carboxylation rate and maximum electron transfer rate, which are also difficult to determine at the ecosystem level.

To overcome limitations in stomatal conductance models, some investigations have explored the use of space-borne measurements to represent G_c. Yebra et al. (2012) found that vegetation indices (VIs) derived from MODIS could be used to compute global canopy conductance (Yebra et al., 2012). The results we obtain for G_c over CONUS are very similar in magnitude and spatial distribution as the midday averages reported by Yebra et al. (2012) between 2001 and 2011. In our study, as well as in that of Yebra et al., maximum G_c occurs in the eastern United States, where yearly average midday G_c is 0.6 — 0.7 cm/s (Fig. 4.A5). We however report lower yearly average G_c ($\sim$0.4 cm/s compared to $\sim$0.8 cm/s) in the Pacific Northwest. This difference may in part be the result of a decline in forest productivity in western forests over the past decade (Mekonnen et al., 2016; Jiang et al., 2019). We also consider it likely that the use of vegetation indices by Yebra et al. (2012) may have resulted in an overestimation of yearly average G_c for the evergreen forests of the Pacific Northwest. The largest deviation in SIF and vegetation indices occurs for evergreen forests, with vegetation indices showing little seasonal variation for winter-dormant evergreen forests (Magney et al., 2019).

SIF has been shown to be a robust predictor of ecosystem transpiration (Maes et al., 2020; Damm et al., 2021; Jonard et al., 2020). Maes *et al.* (2020) demonstrated that SIF and transpiration are highly correlated, with SIF predicting transpiration more reliably than any other satellite product. This relationship is determined by temperature and water use efficiency (Maes et al., 2020). The value of SIF in directly determining G_c has also been previously demonstrated (Shan et al., 2019, 2021; Damm et al., 2021). Shan *et al.* (2019) show that SIF and G_c co-vary and that the strength of the relationship improves when the data is aggregated on longer timescales ($>$ 1 day). The authors propose that although their model is unable to provide information about dynamic changes in G_c, it reliably represents seasonal behavior. Similarly, our SIF-G_c model may not capture the dynamic response of G_c to environmental variables on daily and shorter timescales, but can reasonably represent weekly, monthly, seasonal, and yearly changes. Another limitation noted by Shan *et al.* (2019) is that their SIF-G_c model may not accurately capture changes in the Ball-Berry parameter (m). Our approach to aggregating data somewhat overcomes this limitation by deriving m using a large scale multi-year dataset, as opposed to prescribing a value for m based on previous ecosystem measurements. Shan *et al.* (2021) extended the findings of Shan *et al.* (2019) and developed an empirical model linking G_c, SIF and VPD at a deciduous broadleaf site and two wheat cropland locations. They show that the correlation between SIF and $G_c \times VPD^{0.5}$ is stronger than the link between G_c and SIF alone. Damm *et al.* (2021) also found a strong relationship between SIF and transpiration and suggest that this relationship covaries with biotic and abiotic drivers, especially R_n and LAI. We, however, chose to not include VPD, R_n or LAI, in our model, as this would also require accurate retrievals of temperature, relative humidity, and R_n over large spatial scales. Further, Shan *et al.* (2021) also show that the difference between the SIF-G_c and SIF-$G_c \times VPD^{0.5}$ correlations is minimal during the early afternoon, when SIF-G_c correlations are maximal. Although our approach does not represent non-linearities in the SIF-G_c relationship or changes in m with environmental conditions, it more adequately predicts average regional behavior with minimal parameters, making our approach especially applicable to large spatial and temporal scales.

The ability of SIF to represent G_c eliminates the need for modeling stomatal behavior with parameters for land type and meteorology, making SIF a powerful tool for predicting canopy conductance across large spatial regions. This has particular potential applications to the atmospheric lifetime and composition of depositing species, such as ozone, NO_2, and peroxy nitrates. We propose that consideration of SIF-derived G_c can offer improved constraints on stomatal deposition in global and regional CTMs. Further improvements of SIF-derived G_c across large spatial regions could be achieved with advancements in retrievals of additional environmental drivers (Damm et al., 2021; Jonard et al., 2020; Maes et al., 2020).

4.6 Application of TROPOMI SIF-derived G_c to stomatal N deposition over CONUS

While the wet deposition of reactive nitrogen (N_r) is monitored across North America through the US National Atmospheric Deposition Program (NADP) and the Canadian Air and Precipitation Monitorning Network (CAPMoN) (CAP; NAD), measurements of the air-surface exchange of N_r with vegetation remain scarce (Walker et al., 2019; Vet et al., 2013; Zhang et al., 2012, 2018). Wet deposition and throughfall measurements have provided estimates of the wet and dry deposition of N_r to vegetation surfaces (Du et al., 2014; Li et al., 2016). These measurements can be used to quantify the surface deposition of nitrogen oxide gases, such as HNO_3, but cannot capture the deposition of N_r through leaf stomata.

The current understanding of reactive nitrogen deposition to leaf stomata at a canopy and regional scale is based on an out-dated resistance model approach that is poorly constrained and heavily parameterized (Wesely, 1989). In the following sections, we demonstrate the potential application of our G_c-SIF model as a tool for improving quantitative assessments of the magnitude, spatial, and temporal patterns of the stomatal deposition of N_r. We first discuss the derivation of stomatal NO_2 and peroxyacetyl nitrate (PAN) fluxes across CONUS. We then offer an analysis of how stomatal deposition of NO_2 and PAN affects the atmospheric lifetime of these N_r species.

4.6.1 NO_2 and PAN deposition velocities

Controlled laboratory NO_2 and PAN deposition experiments to vegetation have found that the deposition of these N_r compounds mainly proceeds through stomatal uptake and that deposition scales directly with stomatal conductance (Sparks et al., 2003; Teklemariam and Sparks, 2004; Chaparro-Suarez et al., 2011; Delaria et al., 2020; Place et al., 2020). Surface deposition of these compounds has also been observed, but is suggested to be a minor deposition pathway. For example, Delaria *et al.* (2020) and Place *et al.* (2020) investigated NO_2 and PAN deposition to 14 tree species grown under a variety of conditions and report a consistent relationship between the deposition velocities (V_d) of these gases and stomatal conductance (g_s). NO_2 and PAN were found to have deposition velocities equal to $0.56g_s$ and $0.3g_s$, respectively, with uncertainties in the relationships of less than 10%. It is possible that non woody herbaceous plants (e.g. crops and grasses) and C4 plants may process reactive nitrogen in a different manner than the tree species examined by Delaria et al., 2020 and Place et al., 2020. We are not aware of a mechanistic reason to expect that this would be the case, but further studies are needed to understand the scale factors appropriate for crops and to confirm that stomatal uptake is the only important mechanism for crops and grasses. Using the relationships determined from these studies we estimate the canopy-level V_d's for NO_2 and PAN as $0.56G_c$ and $0.3G_c$, respectively, from the SIF-derived G_c measurements across CONUS. We provide a comparison of these predicted V_d values to those predicted by GEOS-Chem at a local time of 13:30 in Figures 4.6 and 4.7. Deposition in GEOS-Chem is described through the Wesely resistance model, which models deposition through an aerodynamic resistance term, boundary layer resistance term and a surface deposition resistance term. At an LT of 13:30, atmospheric conditions are expected to be largely unstable and the deposition rates of NO_2 and PAN are likely limited by surface deposition. Surface deposition in GEOS-Chem is heavily parameterized and encompasses both stomatal and non-stomatal pathways, and as such cannot offer a direct comparison with SIF derived G_c, but can be used to infer differences between the two approaches.

In general there is good agreement between the spatial distribution of V_d implied by GEOS-Chem and TROPOMI SIF for both PAN and NO_2 (Figs 4.6 and 4.7). The deposition rates for NO_2 and PAN predicted by GEOS-Chem, however, tend to be much higher (up to a factor of 2 for PAN) than those predicted by TROPOMI in most locations. The higher estimates in V_d rates by GEOS-Chem are likely due to the inclusion of considerable cuticular and surface deposition (eg. to soil, branch/cuticle surfaces) terms used in GEOS-Chem. Figure 4.6 also shows that GEOS-Chem seems to disproportionately overestimate NO_2 deposition in the western United States during the late summer compared to mid-summer. This effect could be driven by the way the Wesely model parameterizes stomatal deposition, which neglects the effects from drought stress on stomatal uptake caused by low soil and air moisture. Stomatal conductance models that are more heavily parameterized have been shown to reproduce stomatal rates more accurately (Delaria and Cohen, 2020). One key advantage of the SIF-G_c fitting model is that it is able to capture real-time changes in G_c induced by changing environmental and biological variables. We also see in figure 4.6

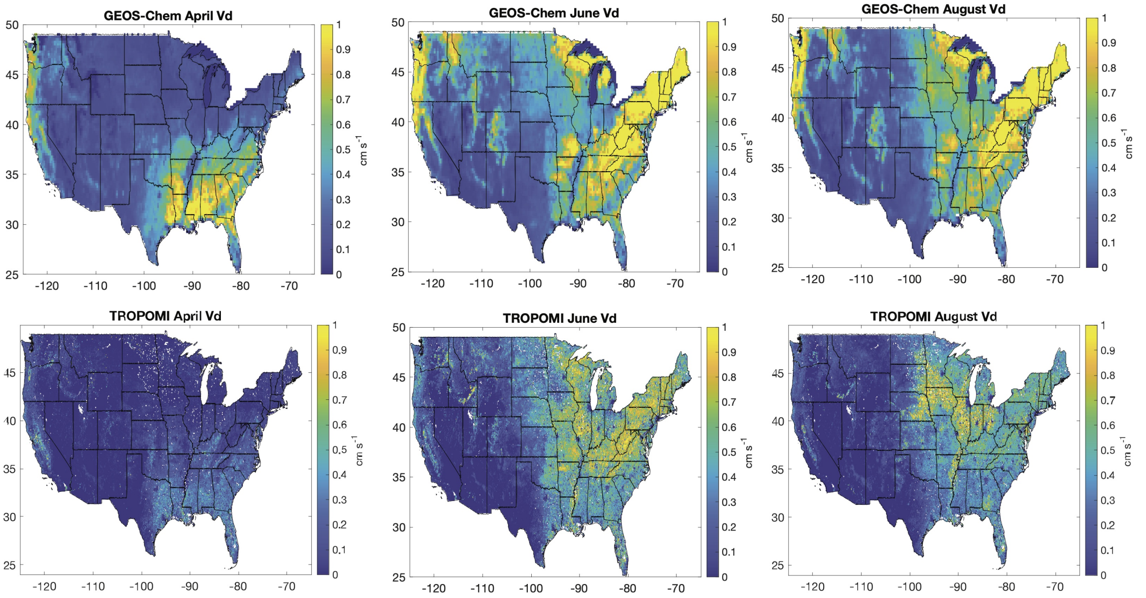

Figure 4.6: Average 2018 monthly NO_2 deposition velocities (V_d) as predicted by (top) GEOS-Chem and (bottom) TROPOMI SIF measurements at the time of TROPOMI's overpass (LT 13:30). It should be noted that GEOS-Chem deposition velocities include surface non-stomatal deposition.

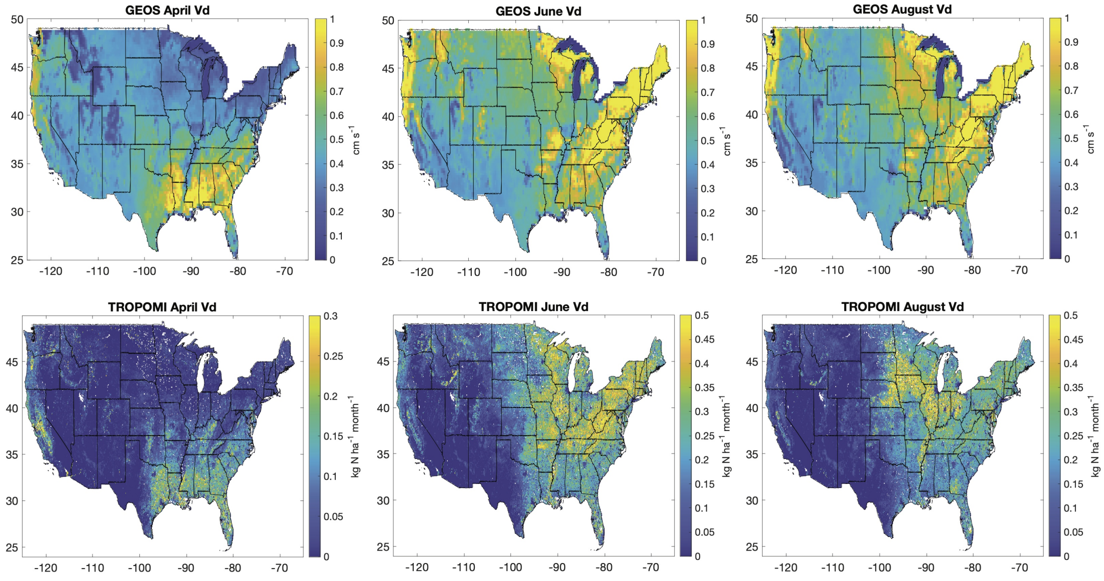

Figure 4.7: Average 2018 monthly PAN deposition velocities (V_d) as predicted by (top) GEOS-Chem and (bottom) TROPOMI SIF measurements at the time of TROPOMI's overpass (LT 13:30). It should be noted that GEOS-Chem deposition velocities include surface non-stomatal deposition.

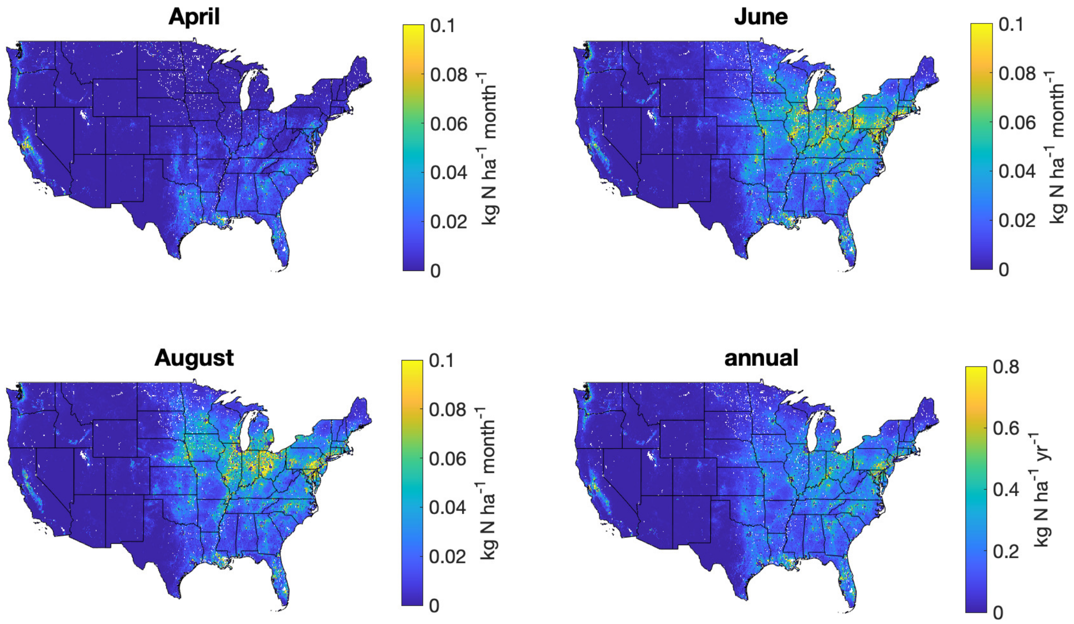

Figure 4.8: Estimated NO_2 stomatal fluxes over CONUS for the months of a) April, b) June, and c) August as well as the d) annual estimated NO_2 stomatal fluxes for 2018. Estimates were derived using TROPOMI SIF measurements and WRF-Chem NO_2 surface concentrations and meteorological outputs as described in Sect 4.6.1.

that GEOS-Chem may be underestimating NO_2 deposition in the corn belt of the Midwest and the California Central Valley, and is likely not capturing the full extent of the growing season in these crop regions.

4.6.2 NO_2 and PAN fluxes

We estimate the fluxes of NO_2 and PAN at the canopy-level via Eq. 4.10—4.11.

$$\text{Flux}_{NO_2} = 0.56 G_c [NO_2] \tag{4.10}$$

$$\text{Flux}_{PAN} = 0.3 G_c [PAN] \tag{4.11}$$

Figures 4.8 and 4.9 show estimates of the monthly integrated fluxes of NO_2 and PAN, respectively. Monthly fluxes were calculated by summing hourly fluxes during each day for a particular month. Hourly integrated fluxes were calculated by multiplying hourly NO_2 or PAN surface concentrations from WRF-Chem (see Section 4.3.4) with hourly calculated G_c. See Figure 4.A10 for midday fluxes calculated using different methods for estimating

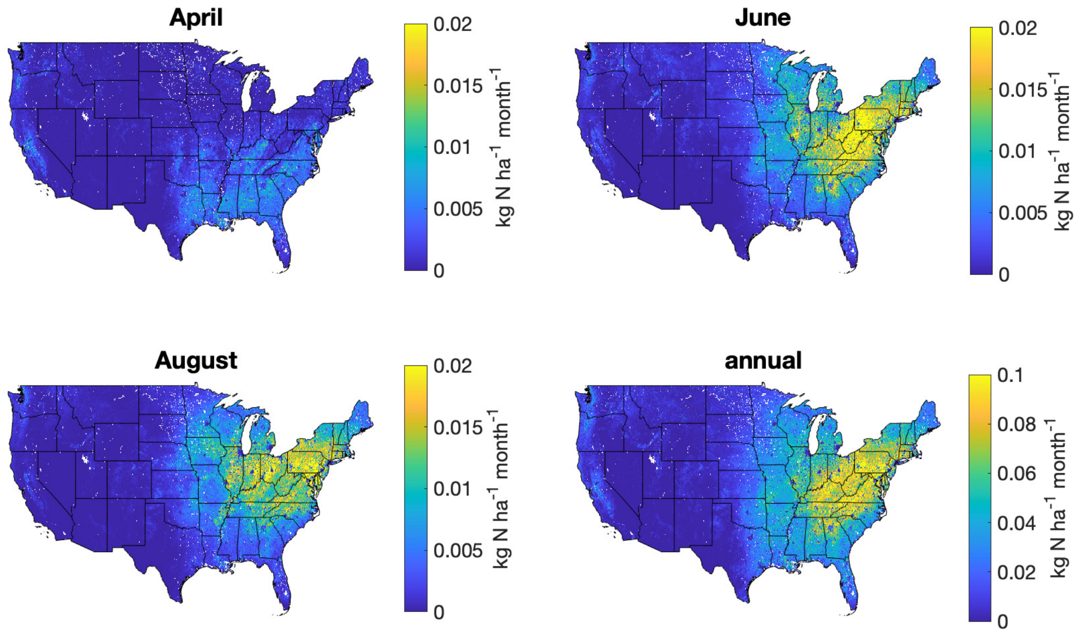

Figure 4.9: Estimated PAN stomatal fluxes over CONUS for the months of a) April, b) June, and c) August as well as the d) annual estimated NO_2 stomatal fluxes for 2018. Estimates were derived using TROPOMI SIF measurements and WRF-Chem PAN surface concentrations and meteorological outputs as described in Sect 4.6.1.

surface NO_2 concentrations (GEOS-Chem, WRF-Chem, TROPOMI NO_2). Hourly G_c was calculated by scaling the G_c at the time of TROPOMI's early afternoon overpass by the ratio of the light response parameter f_{light} at a particular time to f_{light} at the overpass time, where f_{light} is described by Eq. 4.12, derived from Emberson (2000)emberson00.

$$f_{light} = 1 - \exp(\alpha \times PPFD_0 \times \cos(SZA)) \tag{4.12}$$

$PPFD_0$ is the photosynthetic photon flux density at a solar zenith angle (SZA) of 0, approximately equal to 2200 μmol m^{-2} s^{-1} (Madronich and Flocke, 1999). The α parameter has been shown to vary from -0.01— -0.003 depending on the plant species (Büker et al., 2012). We set α equal to -0.005 to err on the side of underestimating G_c at lower daily light levels.

Our SIF and WRF derived fluxes of NO_2 show that the largest fluxes occur in agricultural and near-urban regions of the Midwest, and Eastern Seaboard during the late summer, with maximum fluxes of over 0.1 kgN ha^{-1} month^{-1} (Fig 4.8). Substantial NO_2 fluxes (0.1 kgN ha^{-1} month^{-1}) can also be observed in the agricultural regions of California's Central Valley and the Pacific Northwest from April—August. Maximum yearly NO_2 fluxes reach up to 0.8

kgN ha^{-1} year^{-1} in the Central Valley and near-urban regions of the eastern United States. PAN fluxes are largest during the summer inland of East Coast cities, with maximum fluxes up to 0.02 kgN ha^{-1} month^{-1} and 0.1 kgN ha^{-1} year^{-1} (Fig 4.9). PAN deposition primarily occurs in the Eastern half of CONUS, driven by higher estimated concentrations of PAN in this region. These observations are consistent with field measurements and previous model simulations of PAN across CONUS (Fischer et al., 2014).

In models, the limitation to the deposition rate introduced by turbulence and diffusion is represented as an aerodynamic resistance parameter. Aerodynamic resistances are typically 2-10 times less than the resistance associated with maximum stomatal diffusion of NO_2 and PAN during the daytime. Under the big-leaf model, which our approach resembles, aerodynamic resistances are typically less than 5 s cm^{-1}, with most daytime values falling below 1 s cm^{-1} in a variety of regions (Padro, 1996; Zhang et al., 2003; Schwede et al., 2011). Aerodynamic resistances are largest in forests (regions of higher LAI) and under low wind speeds, particularly during the nighttime when we do not consider stomatal deposition (Padro, 1996; Zhang et al., 2003; Schwede et al., 2011). The error introduced by neglecting turbulence and diffusion is likely to be greater at larger G_c. We estimate that neglecting aerodynamic resistances could result in an over estimation of NO_2 and PAN annual fluxes by up to 30% and 10%, respectively (Fig. 4.A11). In addition to stomatal behavior, aerodynamic resistance is one of the most uncertain attributes of dry deposition estimates, with different parameterisations resulting in large differences in nitrogen dry deposition estimates, particularly for species such as HNO_3 that have a very low surface resistance to deposition (Schwede et al., 2011).

The method we used to calculate monthly integrated G_c also assumes that the maximum canopy conductance occurs at the time of maximum light intensity. This assumption is likely to be accurate under most environmental conditions. However, in some semi-arid environments, such as many west coast forests, as soil and air moisture decline in the afternoon during the summer, stomata close in response, resulting in a daily maximum stomatal conductance occuring in the late morning, rather than early afternoon (Delaria and Cohen, 2020). Our method would result in an underestimation of deposition fluxes at locations with this behavior. Assuming maximum canopy conductance at the time of maximum photosynthetic photon flux density (PPFD) would likely capture reductions in deposition due to heat stress, as the time of daily maximum temperature is likely to correspond to the time of maximum PPFD. An overestimation of fluxes could result, however, in cases where stomatal closure results from cold temperatures in the morning and evening, though this effect is likely to be minor during the growing season.

Nighttime stomatal deposition was not considered in the monthly and annual flux calculations, which may lead to underestimates of fluxes since the uptake of nitrogen oxides by stomata during the night has been identified as an important deposition process (Delaria et al., 2020). The inclusion of winter months in the calculation of of PAN and NO_2 annual fluxes also introduces some uncertainty to the flux estimates as discussed in Section 4.4.2. However, the much lower predicted canopy conductances during these months make the uncertainty in winter months unlikely to contribute substantially to the absolute uncertainty in yearly fluxes.

To date there are very few direct measurements of reactive nitrogen (N_r) dry deposition across CONUS (Walker et al., 2019). As a result, regional estimates of N_r dry deposition are estimated either by coupling ambient measurements of N_r with inferential models or by running chemical transport models (Sickles II and Shadwick, 2015; Li et al., 2016; Schwede and Lear, 2014; Bowker et al., 2011). Differences in model parameterisations of atmosphere-canopy exchange processes have been shown to result in substantially different fluxes of reactive nitrogen (Walker et al., 2019; Schwede et al., 2011). Improved constraints on reactive nitrogen deposition fluxes are therefore needed. The National Atmospheric Deposition Program (NADP) through the Ammonia Monitoring Network (AMoN) and the Clean Air Status and Trends Network (CASTNET) monitor ambient concentrations and the wet deposition of nitrogen-containing compounds over CONUS and are frequently used for assessments of nitrogen deposition (Schwede and Lear, 2014). Measurements from these networks are coupled with the Community Multi-Scale Air Quality (CMAQ) model to estimate nitrogen wet and dry deposition as gaseous and particulate nitrate and ammonium, as well as the deposition of unmeasured gaseous species (e.g. NO_2, PAN, HONO, etc.)(Schwede and Lear, 2014).

In Figure 4.10 we compare our estimates of yearly PAN and NO_2 fluxes as a fraction of the unmeasured nitrogen deposition obtained from CASTNET CMAQ data and as a fraction of total nitrogen deposition. Our results indicate that deposition fluxes of NO_2 in particular may be up to 25—50% of unmeasured N_r deposition as predicted by CMAQ in regions of the United States with substantial vegetation coverage (Fig. 4.10). PAN is also found to constitute up to 10% of the total unmeasured nitrogen deposition in parts of the eastern United States. Near urban centers, and in certain agricultural valleys, like the Central Valley of California, NO_2 deposition can make up to 15% of the total nitrogen deposition as reported by CASTNET.

Our SIF-derived estimates of G_c, coupled with WRF estimates of NO_2 and PAN surface concentrations, represents a new method for constraining the fluxes of reactive nitrogen over large temporal and spatial scales. Such indirect measurements of G_c could potentially be combined with concentrations of NO_2 and PAN derived from other chemical transport models and observations (e.g. Fig. 4.A10). The analysis of residuals between the G_c-SIF model we present and other G_c models could also offer insights into the processes driving large-scale G_c, particularly as they relate to phenology. This method could also be easily extended to other depositing species shown to have deposition velocities that scale linearly with stomatal conductance.

4.6.3 NO_x and PAN lifetime to stomatal deposition

The lifetime of NO_x and PAN to stomatal uptake in the boundary layer can be estimated by dividing each species respective canopy conductance uptake rate by the planetary boundary layer (PBL) height. This approach to calculating a stomatal lifetime assumes that the stomatal uptake is rate limiting and that the aerodynamic and boundary layer resistance are

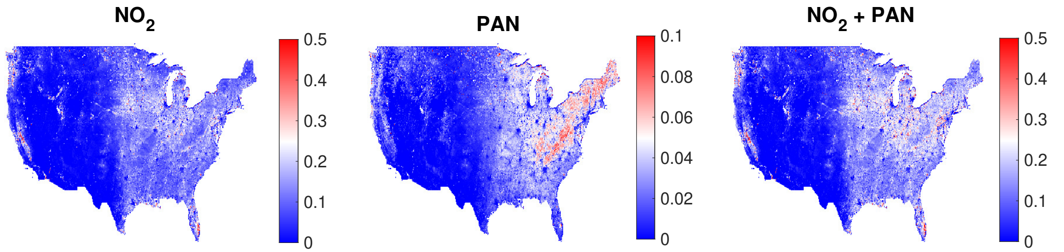

Fraction of unmeasured N deposition

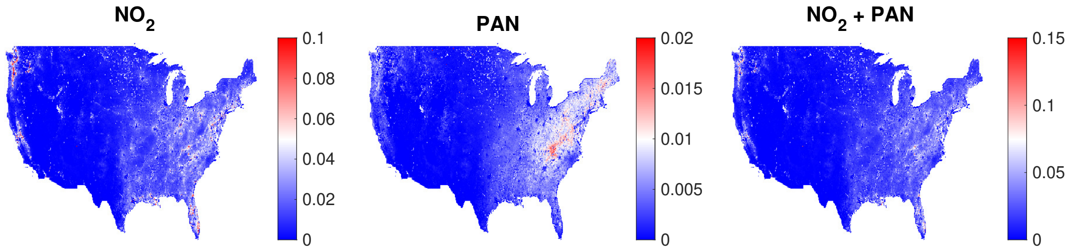

Fraction of total N deposition

Figure 4.10: Yearly SIF-estimated stomatal a) NO_2 fluxes, b) PAN fluxes, and c) NO_2 + PAN fluxes as a fraction of the CASTNET CMAQ modeled estimates of total unmeasured nitrogen deposition over CONUS. Yearly SIF-estimated stomatal d) NO_2 fluxes, e) PAN fluxes, and f) NO_2 + PAN fluxes as a fraction of the CASTNET estimates of total nitrogen deposition over CONUS.

negligible compared to the stomatal deposition rate. Figure 4.11 shows the average lifetimes of NO_x and PAN to stomatal deposition at 13:30 local time for the months of April, June and August 2018 across CONUS. Average monthly PBL heights for the months of April, June and August across CONUS were calculated in WRF-Chem. Figure 4.11 indicates that NO_x lifetimes to stomatal uptake range from as low as 20 hours to over 150 hours across CONUS. The lifetime of PAN in the boundary layer is much longer (50-300 hours) due to its lower stomatal uptake rate. The lifetimes of NO_x and PAN are typically shorter in areas of high biological activity (see Fig 4.5). However shorter lifetimes are also observed in coastal regions, such as the Pacific Northwest in the months of June and August, and this is due to the lower PBL heights in marine environments.

Satellite estimates of NO_x lifetime in major US cities have indicated that the lifetime of NO_x in urban environments ranges from ∼1—8 hours (Laughner and Cohen, 2019; Liu et al., 2016). This suggests that during the growing season the deposition of NO_x to vegetation may compete with the chemical loss of NO_x to nitric acid or organic nitrates in certain regions. The lifetime of NO_x in rural regions has been difficult to probe directly, but is estimated to be longer in these environments than urban environments. A study conducted by Romer *et al.* (2016) estimated that the photochemical lifetime of NO_x in an Alabama forest was 11 ± 5 hours (Romer et al., 2016). At this timescale and in a heavily forested environment, it is likely that deposition will be an important removal process of atmospheric

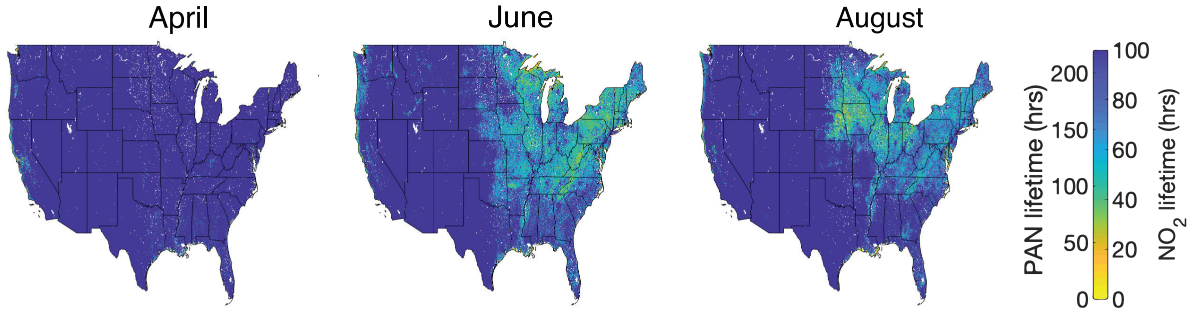

Figure 4.11: Average SIF-derived lifetimes of NO_2 and PAN to stomatal deposition over CONUS during a) April, b) June, and c) August 2018 at the time of TROPOMI's overpass (13:30 LT).

NO_x. The stomatal removal of PAN from the atmosphere is less likely to be competitive with its thermochemical loss, which occurs on the timescale of <10 hours during warmer months. Deposition could however play an influential role in PAN removal when air temperatures are low ($T < 20$ °C). A complete assessment of the role of stomatal uptake in NO_x and PAN lifetimes is beyond the scope of this current work but could be an interesting extension to this work in a future investigation.

4.7 Conclusions

We developed a coupled SIF-GPP-G_c model to estimate G_c at 500m spatial resolution across CONUS, and demonstrate that SIF and GPP can also be used as a proxy for G_c. We then show how SIF-derived G_c can be used to estimate fluxes of NO_2 and PAN over CONUS.

In developing the SIF-GPP-G_c model, we show that GPP and G_c are correlated at a majority of sites across the Ameriflux network. This observed co-variation between GPP and G_c is consistent with the Ball-Berry framework. Correlations between GPP and G_c are highest at crop sites and lowest at wetland sites. We attribute the lower correlations at wetland sites to interference from surface evaporation in our estimation of G_c. Our analysis shows that on average the GPP-G_c response can be described through a single slope of 0.036 $[(\text{cm s}^{-1}\ H_2O)(\mu\ \text{mol}^{-1}\ CO_2\ \text{m}^2\ \text{s})]$ for all ecosystem types.

By combining the empirical GPP-G_c relationship with the SIF-GPP model described by Turner *et al.* (2021), we were able to estimate G_c across CONUS using SIF retrievals from TROPOMI at the time of instrument overpass (13:30 LT). Key agricultural features such as the Central Valley in California and the Corn Belt in the Midwest are clearly discernible from space using the model. The monthly average G_c estimates we calculated were of comparable magnitude and spatial distribution to other midday estimates of G_c across CONUS during the growing season.

We combined our model with surface concentration estimates of NO_2 and PAN from WRF-Chem to estimate monthly and annual dry deposition fluxes of these species across CONUS for 2018. Using this method we estimated maximum stomatal fluxes of 0.8 kgN ha^{-1} yr^{-1} and 0.1 kgN ha^{-1} yr^{-1} over CONUS for NO_2 and PAN, respectively. A comparison of our estimates of N_r dry deposition with CASTNET CMAQ suggests that the dry deposition of NO_2 and PAN may represent a substantial portion of unmeasured N_r deposition.

This work shows promise for constraining G_c with measurements of SIF in global atmospheric models. We propose that this model can serve as a useful tool for constraining regional canopy transpiration fluxes and the stomatal atmosphere-biosphere exchange of gases.

4.8 References

Canadian Air and Precipitation Monitoring Network, URL http://data.ec.gc.ca/data/air/monitor/networks-and-studies/canadian-air-and-precipitation-monitoring-network-capmon/.

National Atmospheric Deposition Program, URL http://nadp.slh.wisc.edu/.

Altimir, N., Tuovinen, J.-P., Vesala, T., Kulmala, M., and Hari, P.: Measurements of ozone removal by Scots pine shoots: Calibration of a stomatal uptake model including the non-stomatal component, Atmospheric Environment, 38, 2387–2398, https://doi.org/10.1016/j.atmosenv.2003.09.077, 2004.

Baker, I. T., Scott Denning, A., and Stöckli, R.: North American gross primary productivity: regional characterization and interannual variability, 62B, 533–549, https://doi.org/10.1111/j.1600-0889.2010.00492.x, 2010.

Ball J. T., Woodrow I. E., B. J. A.: A model predicting stomatal conductance and its contribution to the control of photosynthesis under different environmental conditions, Martinus Nijhoff Publishers, Dordrecht, Netherlands, 1988.

Barnard, D. M. and Bauerle, W. L.: The implications of minimum stomatal conductance on modeling water flux in forest canopies, Journal of Geophysical Research: Biogeosciences, 118, 1322–1333, https://doi.org/https://doi.org/10.1002/jgrg.20112, URL https://agupubs.onlinelibrary.wiley.com/doi/abs/10.1002/jgrg.20112, 2013.

Barraza, V., Restrepo-Coupe, N., Huete, A., Grings, F., and Van Gorsel, E.: Passive microwave and optical index approaches for estimating surface conductance and evapotranspiration in forest ecosystems, Agricultural and Forest Meteorology, 213, 126–137, https://doi.org/10.1016/j.agrformet.2015.06.020, 2015.

Bonan, G., Williams, M., Fisher, R., and Oleson, K.: Modeling stomatal conductance in the Earth system: Linking leaf water-use efficiency and water transport along the soil-plant-atmosphere continuum, Geoscientific Model Development, 7, 2193–2222, https://doi.org/10.5194/gmd-7-2193-2014, 2014.

Bowker, G., Schwede, D., Lear, G., Warren-Hicks, W., and Finkelstein, P.: Quality Assurance Decisions with Air Models: A Case Study of Imputation of Missing Input Data Using EPA's Multi-layer Model, Water Air and Soil Pollution - WATER AIR SOIL POLLUT, 222, https://doi.org/10.1007/s11270-011-0832-7, 2011.

Buchholz, R. R., Emmons, L. K., Tilmes, S., and Team, T. C. D.: CESM2.1/CAM-chem Instantaneous Output for Boundary Conditions. UCAR/NCAR - Atmospheric Chemistry Observations and Modeling Laboratory, https://doi.org/https://doi.org/10.5065/NMP7-EP60.

Büker, P., Morrissey, T., Briolat, A., Falk, R., Simpson, D., Tuovinen, J.-P., Alonso, R., Barth, S., Baumgarten, M., Grulke, N., Karlsson, P. E., King, J., Lagergren, F., Matyssek, R., Nunn, A., Ogaya, R., Peñuelas, J., Rhea, L., Schaub, M., Uddling, J., Werner, W., and Emberson, L. D.: DO_3SE modelling of soil moisture to determine ozone flux to forest trees, Atmospheric Chemistry and Physics, 12, 5537–5562, https://doi.org/10.5194/acp-12-5537-2012, URL https://acp.copernicus.org/articles/12/5537/2012/, 2012.

Chaparro-Suarez, I., Meixner, F., and Kesselmeier, J.: Nitrogen dioxide (NO2) uptake by vegetation controlled by atmospheric concentrations and plant stomatal aperture, Atmospheric Environment, 45, 5742 – 5750, https://doi.org/https://doi.org/10.1016/j.atmosenv.2011.07.021, URL http://www.sciencedirect.com/science/article/pii/S1352231011007461, 2011.

Cleugh, H. A., Leuning, R., Mu, Q., and Running, S. W.: Regional evaporation estimates from flux tower and MODIS satellite data, Remote Sensing of Environment, 106, 285–304, https://doi.org/10.1016/j.rse.2006.07.007, 2007.

Clifton, O. E., Fiore, A. M., Massman, W. J., Baublitz, C. B., Coyle, M., Emberson, L., Fares, S., Farmer, D. K., Gentine, P., Gerosa, G., Guenther, A. B., Helmig, D., Lombardozzi, D. L., Munger, J. W., Patton, E. G., Pusede, S. E., Schwede, D. B., Silva, S. J., Sörgel, M., Steiner, A. L., and Tai, A. P. K.: Dry Deposition of Ozone Over Land: Processes, Measurement, and Modeling, Reviews of Geophysics, 58, e2019RG000 670, https://doi.org/https://doi.org/10.1029/2019RG000670, URL https://agupubs.onlinelibrary.wiley.com/doi/abs/10.1029/2019RG000670, e2019RG000670 2019RG000670, 2020.

Collatz, G. J., Ribas-Carbo, M., and Berry, J. A.: Coupled photosynthesis-stomatal conductance model for leaves of C_4 plants, Functional Plant Biology, 19, 519–538, https://doi.org/10.1071/PP9920519, 1992.

Cowan, I.: Stomatal Behaviour and Environment, vol. 4 of *Advances in Botanical Research*, pp. 117 – 228, Academic Press, https://doi.org/https://doi.org/10.1016/S0065-2296(08)60370-5, URL http://www.sciencedirect.com/science/article/pii/S0065229608603705, 1978.

Damm, A., Haghighi, E., Paul-Limoges, E., and van der Tol, C.: On the seasonal relation of sun-induced chlorophyll fluorescence and transpiration in a temperate mixed forest, Agricultural and Forest Meteorology, 304-305, 108 386, https://doi.org/https://doi.org/10.1016/j.agrformet.2021.108386, URL https://www.sciencedirect.com/science/article/pii/S0168192321000691, 2021.

Delaria, E. R. and Cohen, R. C.: A model-based analysis of foliar NOx deposition, Atmospheric Chemistry and Physics, 20, 2123–2141, https://doi.org/10.5194/acp-20-2123-2020, URL https://acp.copernicus.org/articles/20/2123/2020/, 2020.

Delaria, E. R., Place, B. K., Liu, A. X., and Cohen, R. C.: Laboratory measurements of stomatal NO2 deposition to native California trees and the role of forests in the NOx cycle, Atmospheric Chemistry and Physics Discussions, 2020, 1–32, https://doi.org/10.5194/acp-2020-240, URL https://www.atmos-chem-phys-discuss.net/acp-2020-240/, 2020.

Du, E., Vries, W., Galloway, J., Hu, X., and Fang, J.: Changes in wet nitrogen deposition in the United States between 1985 and 2012, Environmental Research Letters, 9, 095 004, https://doi.org/10.1088/1748-9326/9/9/095004, 2014.

Emberson, L., Wieser, G., and Ashmore, M.: Modelling of stomatal conductance and ozone flux of Norway spruce: comparison with field data, Environmental Pollution, 109, 393 – 402, https://doi.org/https://doi.org/10.1016/S0269-7491(00)00042-7, URL http://www.sciencedirect.com/science/article/pii/S0269749100000427, 2000.

Emmons, L. K., Schwantes, R. H., Orlando, J. J., Tyndall, G., Kinnison, D., Lamarque, J.-F., Marsh, D., Mills, M. J., Tilmes, S., Bardeen, C., Buchholz, R. R., Conley, A., Gettelman, A., Garcia, R., Simpson, I., Blake, D. R., Meinardi, S., and Patron, G.: The Chemistry Mechanism in the Community Earth System Model Version 2 (CESM2), Journal of Advances in Modeling Earth Systems, 12, e2019MS001 882, https://doi.org/https://doi.org/10.1029/2019MS001882, URL https://agupubs.onlinelibrary.wiley.com/doi/abs/10.1029/2019MS001882, e2019MS001882 2019MS001882, 2020.

EPA: Air Pollutant Emissions Trends Data, URL https://www.epa.gov/air-emissions-inventories/air-pollutant-emissions-trends-data, 2016.

Fischer, E. V., Jacob, D. J., Yantosca, R. M., Sulprizio, M. P., Millet, D. B., Mao, J., Paulot, F., Singh, H. B., Roiger, A., Ries, L., Talbot, R. W., Dzepina, K., and Pandey Deolal, S.:

Atmospheric peroxyacetyl nitrate (PAN): a global budget and source attribution, Atmospheric Chemistry and Physics, 14, 2679–2698, https://doi.org/10.5194/acp-14-2679-2014, URL https://acp.copernicus.org/articles/14/2679/2014/, 2014.

Glenn, E. P., Nagler, P. L., and Huete, A. R.: Vegetation index methods for estimating evapotranspiration by remote sensing, Surveys in Geophysics, 31, 531–555, https://doi.org/10.1007/s10712-010-9102, 2010.

Glenn, E. P., Doody, T. M., Guerschman, J. P., Huete, A. R., King, E. A., McVicar, T. R., Van Dijk, A. I. J. M., Van Niel, T. G., Yebra, M., and Zhang, Y.: Actual evapotranspiration estimation by ground and remote sensing methods: the Australian experience, Hydrological processes, 25, 4103–4116, https://doi.org/10.1002/hyp.8391, 2011a.

Glenn, E. P., Neale, C. M. U., Hunsaker, D. J., and Nagler, P. L.: Vegetation index-based crop coefficients to estimate evapotranspiration by remote sensing in agricultural and natural ecosystems, Hydrological processes, 25, 4050–4062, https://doi.org/10.1002/hyp.8392, 2011b.

Green, S.: Radiation balance, transpiration and photosynthesis of an isolated tree, Agricultural and Forest Meteorology, 64, 201 – 221, https://doi.org/https://doi.org/10.1016/0168-1923(93)90029-H, URL http://www.sciencedirect.com/science/article/pii/016819239390029H, 1993.

Guenther, A., Jiang, X., Heald, C., Sakulyanontvittaya, T., Duhl, T., Emmons, L., and Wang, X.: The Model of Emissions of Gases and Aerosols from Nature version 2.1 (MEGAN2.1): an extended and updated framework for modeling biogenic emissions, Geoscientific Model Development Discussions, 5, https://doi.org/10.5194/gmdd-5-1503-2012, 2012.

Gunderson, C., Sholtis, J., Wullschleger, S., Tissue, D., Hanson, P., and Norby, R.: Environmental and stomatal control of photosynthetic enhancement in the canopy of a sweetgum (Liquidambar styraciflua L.) plantation during 3 years of CO2 enrichment, Plant, Cell & Environment, 25, 379 – 393, https://doi.org/10.1046/j.0016-8025.2001.00816.x, 2002.

Hardacre, C., Wild, O., and Emberson, L.: An evaluation of ozone dry deposition in global scale chemistry climate models, Atmospheric Chemistry and Physics, 15, 6419–6436, https://doi.org/10.5194/acp-15-6419-2015, 2015.

He, L., Magney, T., Dutta, D., Yin, Y., Köhler, P., Grossmann, K., Stutz, J., Dold, C., Hatfield, J., Guan, K., Peng, B., and Frankenberg, C.: From the Ground to Space: Using Solar-Induced Chlorophyll Fluorescence to Estimate Crop Productivity, Geophysical Research Letters, 47, e2020GL087 474, https://doi.org/https://doi.org/10.1029/2020GL087474, URL https://agupubs.onlinelibrary.wiley.com/doi/abs/10.1029/2020GL087474, e2020GL087474 2020GL087474, 2020.

Hu, X., Shi, L., and Lin, G.: The data-driven solution of energy imbalance-induced structural error in evapotranspiration models, Journal of Hydrology, 597, 126 205, https://doi.org/https://doi.org/10.1016/j.jhydrol.2021.126205, URL https://www.sciencedirect.com/science/article/pii/S0022169421002523, 2021.

Huang, G., Brook, R., Crippa, M., Janssens-Maenhout, G., Schieberle, C., Dore, C., Guizzardi, D., Muntean, M., Schaaf, E., and Friedrich, R.: Speciation of anthropogenic emissions of non-methane volatile organic compounds: a global gridded data set for 1970–2012, Atmospheric Chemistry and Physics, 17, 7683–7701, https://doi.org/10.5194/acp-17-7683-2017, 2017.

IPCC: IPCC: Climate Change 2013: The Physical Science Basis. Contribution of Working Group I to the Fifth Assessment Report of the Intergovernmental Panel on Climate Change, Tech. rep., IPCC, 2013.

Jiang, Y., Still, C. J., Rastogi, B., Page, G. F. M., Wharton, S., Meinzer, F. C., Voelker, S., and Kim, J. B.: Trends and controls on water-use efficiency of an old-growth coniferous forest in the Pacific Northwest, Environmental Research Letters, 14, 074 029, https://doi.org/10.1088/1748-9326/ab2612, 2019.

Jonard, F., De Cannière, S., Brüggemann, N., Gentine, P., Short Gianotti, D., Lobet, G., Miralles, D., Montzka, C., Pagán, B., Rascher, U., and Vereecken, H.: Value of sun-induced chlorophyll fluorescence for quantifying hydrological states and fluxes: Current status and challenges, Agricultural and Forest Meteorology, 291, 108 088, https://doi.org/https://doi.org/10.1016/j.agrformet.2020.108088, URL https://www.sciencedirect.com/science/article/pii/S0168192320301908, 2020.

Kalma, J. D., McVicar, T. R., and McCabe, M. F.: Estimating land surface evaporation: a review of methods using remotely sensed surface temperature data, Surveys in Geophysics, 29, 421–469, https://doi.org/10.1007/s10712-008-9037-z, 2008.

Kavassalis, S. and Murphy, J.: Understanding ozone-meteorology correlations: A role for dry deposition, Geophysical Research Letters, 44, https://doi.org/10.1002/2016GL071791, 2017.

Kennedy, D., Swenson, S., Oleson, K., Fisher, R., Lawrence, D., da Costa, A., and Gentine, P.: Implementing Plant Hydraulics in the Community Land Model, Version 5, Journal of Advances in Modeling Earth Systems, https://doi.org/10.1029/2018MS001500, 2019.

Knauer, J., Werner, C., and Zaehle, S.: Evaluating stomatal models and their atmospheric drought response in a land surface scheme: A multi-biome analysis, Journal of Geophysical Research: Biogeosciences, 120, 1894–1911, https://doi.org/https://doi.org/10.1002/2015JG003114, URL https://agupubs.onlinelibrary.wiley.com/doi/abs/10.1002/2015JG003114, 2015.

Köhler, P., Frankenberg, C., Magney, T. S., Guanter, L., Joiner, J., and Landgraf, J.: Global Retrievals of Solar-Induced Chlorophyll Fluorescence With TROPOMI: First Results and Intersensor Comparison to OCO-2, Geophysical Research Letters, 45, 10,456–10,463, https://doi.org/https://doi.org/10.1029/2018GL079031, URL https://agupubs.onlinelibrary.wiley.com/doi/abs/10.1029/2018GL079031, 2018.

Lai, C.-T., Katul, G., Oren, R., Ellsworth, D., and Schäfer, K.: Modeling CO_2 and water vapor trubulent flux distributions within a forest canopy, Journal of Geophysical Research, 105, 26 333–26 351, 2000.

Laughner, J. L. and Cohen, R. C.: Direct observation of changing NOx lifetime in North American cities, Science, 366, 723–727, https://doi.org/10.1126/science.aax6832, URL https://science.sciencemag.org/content/366/6466/723, 2019.

Launiainen, S., Katul, G. G., Kolari, P., Vesala, T., and Hari, P.: Empirical and optimal stomatal controls on leaf and ecoysstem level CO_2 and H_2O exchange rates, Agricultural and Forest Meteorology, 151, 1672–1689, https://doi.org/10.1016/j.agrformet.2011.07.001, 2011.

Lerdau, M. T., Munger, J. W., and Jacob, D. J.: The NO2 Flux Conundrum, Science, 289, 2291–2293, https://doi.org/10.1126/science.289.5488.2291, 2000.

Leuning, R.: Modelling stomatal behaviour and photosynthesis of Eucalyptus grandis, Functional Plant Biology, 17, 159–175, https://doi.org/10.1071/PP9900159, 1990.

Leuning, R.: A critical appraisal of a combined stomatal-photosynthesis model for C_3 plants, Plant, Cell & Environment, 18, 339–355, https://doi.org/10.1111/j.1365-3040.1995.tb00370.x, 1995.

Leuning, R., van Gorsel, E., Massman, W. J., and Isaac, P. R.: Reflections on the surface energy imbalance problem, Agricultural and Forest Meteorology, 156, 65–74, https://doi.org/https://doi.org/10.1016/j.agrformet.2011.12.002, URL https://www.sciencedirect.com/science/article/pii/S016819231100339X, 2012.

Li, Y., Schichtel, B. A., Walker, J. T., Schwede, D. B., Chen, X., Lehmann, C. M. B., Puchalski, M. A., Gay, D. A., and Collett, J. L.: Increasing importance of deposition of reduced nitrogen in the United States, Proceedings of the National Academy of Sciences, 113, 5874–5879, https://doi.org/10.1073/pnas.1525736113, URL https://www.pnas.org/content/113/21/5874, 2016.

Liu, F., Beirle, S., Zhang, Q., Dörner, S., He, K., and Wagner, T.: NO_x lifetimes and emissions of cities and power plants in polluted background estimated by satellite observations, Atmospheric Chemistry and Physics, 16, 5283–5298, https://doi.org/10.5194/acp-16-5283-2016, URL https://acp.copernicus.org/articles/16/5283/2016/, 2016.

Liu, S., Mao, D., and Lu, L.: Measurement and estimation of the aerodynamic resistance, Hydrology and Earth System Sciences Discussions, 3, 681–705, URL https://hal.archives-ouvertes.fr/hal-00298684, 2006.

Madronich, S. and Flocke, S.: The Role of Solar Radiation in Atmospheric Chemistry, pp. 1–26, Springer Berlin Heidelberg, Berlin, Heidelberg, https://doi.org/10.1007/978-3-540-69044-3$_1$, $URLhttps : //doi.org/$10.1007/978 $-$ 3 $-$ 540 $-$ 69044 $-$ 3$_1$, 1999.

Maes, W. H., Pagán, B. R., Martens, B., Gentine, P., Guanter, L., Steppe, K., Verhoest, N. E., Dorigo, W., Li, X., Xiao, J., and Miralles, D. G.: Sun-induced fluorescence closely linked to ecosystem transpiration as evidenced by satellite data and radiative transfer models, Remote Sensing of Environment, 249, 112 030, https://doi.org/https://doi.org/10.1016/j.rse.2020.112030, URL https://www.sciencedirect.com/science/article/pii/S0034425720304004, 2020.

Magney, T. S., Bowling, D. R., Logan, B. A., Grossmann, K., Stutz, J., Blanken, P. D., Burns, S. P., Cheng, R., Garcia, M. A., Köhler, P., Lopez, S., Parazoo, N. C., Raczka, B., Schimel, D., and Frankenberg, C.: Mechanistic evidence for tracking the seasonality of photosynthesis with solar-induced fluorescence, Proceedings of the National Academy of Sciences, 116, 11 640–11 645, https://doi.org/10.1073/pnas.1900278116, URL https://www.pnas.org/content/116/24/11640, 2019.

Magney, T. S., Barnes, M. L., and Yang, X.: On the Covariation of Chlorophyll Fluorescence and Photosynthesis Across Scales, Geophysical Research Letters, 47, e2020GL091 098, https://doi.org/https://doi.org/10.1029/2020GL091098, URL https://agupubs.onlinelibrary.wiley.com/doi/abs/10.1029/2020GL091098, e2020GL091098 2020GL091098, 2020.

Maguire, A. J., Eitel, J. U. H., Griffin, K. L., Magney, T. S., Long, R. A., Vierling, L. A., Schmiege, S. C., Jennewein, J. S., Weygint, W. A., Boelman, N. T., and Bruner, S. G.: On the Functional Relationship Between Fluorescence and Photochemical Yields in Complex Evergreen Needleleaf Canopies, Geophysical Research Letters, 47, e2020GL087 858, https://doi.org/https://doi.org/10.1029/2020GL087858, URL https://agupubs.onlinelibrary.wiley.com/doi/abs/10.1029/2020GL087858, e2020GL087858 2020GL087858, 2020.

Marrs, J. K., Reblin, J. S., Logan, B. A., Allen, D. W., Reinmann, A. B., Bombard, D. M., Tabachnik, D., and Hutyra, L. R.: Solar-Induced Fluorescence Does Not Track Photosynthetic Carbon Assimilation Following Induced Stomatal Closure, Geophysical Research Letters, 47, e2020GL087 956, https://doi.org/https://doi.org/10.1029/2020GL087956, URL https://agupubs.onlinelibrary.wiley.com/doi/abs/10.1029/2020GL087956, e2020GL087956 2020GL087956, 2020.

Medlyn, B. E., Duursma, R. A., Eamus, D., Ellsworth, D. S., Colin Prentice, I., Barton, C. V. M., Crous, K. Y., De Angelis, P., Freeman, M., and Wingate, L.: Reconciling the optimal and empirical approaches to modelling stomatal conductance, Global Change Biology, 17, 2134–2144, https://doi.org/https://doi.org/10.1111/j.1365-2486.2010.02375.x, 2011.

Mekonnen, Z. A., Grant, R. F., and Schwalm, C.: Contrasting changes in gross primary productivity of different regions of North America as affected by warming in recent decades, Agricultural and Forest Meteorology, 218-219, 50 – 64, https://doi.org/https://doi.org/10.1016/j.agrformet.2015.11.016, URL http://www.sciencedirect.com/science/article/pii/S0168192315007820, 2016.

Miner, G. L. and Bauerle, W. L.: Seasonal variability of the parameters of the Ball–Berry model of stomatal conductance in maize (Zea mays L.) and sunflower (Helianthus annuus L.) under well-watered and water-stressed conditions, Plant, Cell & Environment, 40, 1874–1886, https://doi.org/https://doi.org/10.1111/pce.12990, URL https://onlinelibrary.wiley.com/doi/abs/10.1111/pce.12990, 2017.

Miner, G. L., Bauerle, W. L., and Baldocchi, D. D.: Estimating the sensitivity of stomatal conductance to photosynthesis, Plant, Cell and Environment, 40, 1214–1238, https://doi.org/10.1111/pce.12871, 2017.

Monteith, J.: Evaporation and environment, Symposia of the Society for Experimental Biology, 19, 205—234, URL http://europepmc.org/abstract/MED/5321565, 1965.

Monteith, J. L.: Principles of Environmental Physics, Edward Arnold Limited, 1973.

Moran, S. M. and Jackson, R. D.: Assessing the spatial distribution of evapotranspiration using remotely sensed inputs, Journal of Environmental Quality, 20, 725–737, 1991.

Myneni, R., Knyazikhin, Y., and Park, T.: MCD15A2H MODIS/Terra+Aqua Leaf Area Index/FPAR 8-day L4 Global 500m SIN Grid V006 [Data set].NASA EOSDIS Land Processes DAAC, https://doi.org/10.5067/MODIS/MCD15A2H.006, 2015.

Ono, K., Maruyama, A., Kuwagata, T., Mano, M., Takimoto, T., Hayashi, K., Hasegawa, T., and Miyata, A.: Canopy-scale relationships between stomatal conductance and photosynthesis in irrigated rice, Global Change Biology, 19, 2209–2220, https://doi.org/10.1111/gcb.12188, 2013.

Padro, J.: Summary of ozone dry deposition velocity measurements and model estimates over vineyard, cotton, grass and deciduous forest in summer, Atmospheric Environment, 30, 2363–2369, https://doi.org/10.1016/1352-2310(95)00352-5, 1996.

Place, B. K., Delaria, E. R., Liu, A. X., and Cohen, R. C.: Leaf Stomatal Control over Acyl Peroxynitrate Dry Deposition to Trees, ACS Earth and Space Chemistry, 4, 2162–2170, https://doi.org/10.1021/acsearthspacechem.0c00152, URL https://doi.org/10.1021/acsearthspacechem.0c00152, 2020.

Reichstein, M., Falge, E., Baldocchi, D., Papale, D., Aubinet, M., Berbigier, P., Bernhofer, C., Buchmann, N., Gilmanov, T., Granier, A., Grünwald, T., Havránková, K., Ilvesniemi, H., Janous, D., Knohl, A., Laurila, T., Lohila, A., Loustau, D., Matteucci, G., Meyers, T., Miglietta, F., Ourcival, J.-M., Pumpanen, J., Rambal, S., Rotenberg, E., Sanz, M., Tenhunen, J., Seufert, G., Vaccari, F., Vesala, T., Yakir, D., and Valentini, R.: On the separation of net ecosystem exchange into assimilation and ecosystem respiration: review and improved algorithm, Global Change Biology, 11, 1424–1439, https://doi.org/https://doi.org/10.1111/j.1365-2486.2005.001002.x, URL https://onlinelibrary.wiley.com/doi/abs/10.1111/j.1365-2486.2005.001002.x, 2005.

Romer, P. S., Duffey, K. C., Wooldridge, P. J., Allen, H. M., Ayres, B. R., Brown, S. S., Brune, W. H., Crounse, J. D., de Gouw, J., Draper, D. C., Feiner, P. A., Fry, J. L., Goldstein, A. H., Koss, A., Misztal, P. K., Nguyen, T. B., Olson, K., Teng, A. P., Wennberg, P. O., Wild, R. J., Zhang, L., and Cohen, R. C.: The lifetime of nitrogen oxides in an isoprene-dominated forest, Atmospheric Chemistry and Physics, 16, 7623–7637, https://doi.org/10.5194/acp-16-7623-2016, URL https://acp.copernicus.org/articles/16/7623/2016/, 2016.

Saunois, M., Bousquet, P., Poulter, B., Peregon, A., Ciais, P., Canadell, J., Dlugokencky, E., Etiope, G., Bastviken, D., Houweling, S., Janssens-Maenhout, G., Tubiello, F., Castaldi, S., Jackson, R., Alexe, M., Arora, V., Beerling, D., Bergamaschi, P., Blake, D., and Zhu, Q.: The Global Methane Budget: 2000–2012, Earth System Science Data Discussions, pp. 1–79, https://doi.org/10.5194/essd-2016-25, 2016.

Schlesinger, W. and Jasechko, S.: Transpiration in the global water cycle, Agricultural and Forest Meteorology, s 189–190, 115–117, https://doi.org/10.1016/j.agrformet.2014.01.011, 2014.

Schwede, D., Zhang, L., Vet, R., and Lear, G.: An intercomparison of the deposition models used in the CASTNET and CAPMoN networks, Atmospheric Environment, 45, 1337–1346, https://doi.org/10.1016/j.atmosenv.2010.11.050, 2011.

Schwede, D. B. and Lear, G. G.: A novel hybrid approach for estimating total deposition in the United States, Atmospheric Environment, 92, 207 – 220, https://doi.org/https://doi.org/10.1016/j.atmosenv.2014.04.008, URL http://www.sciencedirect.com/science/article/pii/S1352231014002805, 2014.

Sellers, P. J., Heiser, M. D., and Hall, F. G.: Relations between surface conductance and spectral vegetation indices and intermediate (100 m2 to 15 km2) length scales, Journal of Geophysical Research, 97, 19 033–19 059, 1992.

Shan, N., Ju, W., Migliavacca, M., Martini, D., Guanter, L., Chen, J., Goulas, Y., and Zhang, Y.: Modeling canopy conductance and transpiration from solar-induced chlorophyll fluorescence, Agricultural and Forest Meteorology, 268, 189–201, https://doi.org/10.1016/j.agrformet.2019.01.031, 2019.

Shan, N., Zhang, Y., Chen, J. M., Ju, W., Migliavacca, M., Peñuelas, J., Yang, X., Zhang, Z., Nelson, J. A., and Goulas, Y.: A model for estimating transpiration from remotely sensed solar-induced chlorophyll fluorescence, Remote Sensing of Environment, 252, 112 134, https://doi.org/https://doi.org/10.1016/j.rse.2020.112134, URL https://www.sciencedirect.com/science/article/pii/S0034425720305071, 2021.

Sickles II, J. E. and Shadwick, D. S.: Air quality and atmospheric deposition in the eastern US: 20 years of change, Atmospheric Chemistry and Physics, 15, 173–197, https://doi.org/10.5194/acp-15-173-2015, URL https://acp.copernicus.org/articles/15/173/2015/, 2015.

Sparks, J. P., Roberts, J. M., and Monson, R. K.: The uptake of gaseous organic nitrogen by leaves: A significant global nitrogen transfer process, Geophysical Research Letters, 30, https://doi.org/https://doi.org/10.1029/2003GL018578, URL https://agupubs.onlinelibrary.wiley.com/doi/abs/10.1029/2003GL018578, 2003.

Teklemariam, T. A. and Sparks, J. P.: Gaseous fluxes of peroxyacetyl nitrate (PAN) into plant leaves, Plant, Cell & Environment, 27, 1149–1158, https://doi.org/https://doi.org/10.1111/j.1365-3040.2004.01220.x, URL https://onlinelibrary.wiley.com/doi/abs/10.1111/j.1365-3040.2004.01220.x, 2004.

Turner, A. J., Köhler, P., Magney, T. S., Frankenberg, C., Fung, I., and Cohen, R. C.: A double peak in the seasonality of California's photosynthesis as observed from space, Biogeosciences, 17, 405–422, https://doi.org/10.5194/bg-17-405-2020, URL https://www.biogeosciences.net/17/405/2020/, 2020.

Turner, A. J., Köhler, P., Magney, T. S., Frankenberg, C., Fung, I., and Cohen, R. C.: Extreme events driving year-to-year differences in gross primary productivity across the US, Biogeosciences Discussions, 2021, 1–13, https://doi.org/10.5194/bg-2021-49, URL https://bg.copernicus.org/preprints/bg-2021-49/, 2021.

Tuzet, A., Perrier, A., and Leuning, R.: A coupled model of stomatal conductance, photosynthesis and transpiration, Plant, Cell & Environment, 26, 1097–1116, https://doi.org/https://doi.org/10.1046/j.1365-3040.2003.01035.x, URL https://onlinelibrary.wiley.com/doi/abs/10.1046/j.1365-3040.2003.01035.x, 2003.

Valentini, R., Gamon, J. A., and Field, C. B.: Ecosystem gas exchange in a California grassland: seasonal patterns and implications for scaling, Ecology, 76, 1940–1952, 1995.

Veefkind, J., Aben, I., McMullan, K., Förster, H., de Vries, J., Otter, G., Claas, J., Eskes, H., de Haan, J., Kleipool, Q., van Weele, M., Hasekamp, O., Hoogeveen, R., Landgraf, J., Snel, R., Tol, P., Ingmann, P., Voors, R., Kruizinga, B., Vink, R., Visser, H., and Levelt, P.: TROPOMI on the ESA Sentinel-5 Precursor: A GMES mission for global observations of the atmospheric composition for climate, air quality and ozone layer applications, Remote Sensing of Environment, 120, 70 – 83, https://doi.org/https://doi.org/10.1016/j.rse.2011.09.027, URL http://www.sciencedirect.com/science/article/pii/S0034425712000661, the Sentinel Missions - New Opportunities for Science, 2012.

Vet, R., Artz, Richard S.and Carou, S., Shaw, M., Ro, C.-U., Aas, W., Baker, A., Bowersox, V. C., Dentener, F., Galy-Lacaux, C., Hou, A., Pienaar, J. J., Gillett, R., Christina Forti, M., Gromov, S., Hara, H., Khodzher, T., Mahowald, N. M., Nickovic, S., Rao, P., and Reid, N. W.: A global assessment of precipitation chemistry and deposition of sulfur, nitrogen, sea salt, base cations, organic acids, acidity and pH, and phosphorus, Atmospheric Environment, 93, 3–100, https://doi.org/10.1016/j.atmosenv.2013.10.060, 2013.

Walker, J. T., Beachley, G., Zhang, L., Benedict, K. B., Sive, B. C., and Schwede, D. B.: A review of measurements of air-surface exchange of reactive nitrogen in natural ecosystems across North America, Science of the Total Environment, 698, 1–18, https://doi.org/10.1016/j.scitotenv.2019.10.133975, 2019.

Wehr, R. and Saleska, S. R.: Calculating canopy stomatal conductance from eddy covariance measurements, in light of the energy budget closure problem, Biogeosciences, 18, 13–24, https://doi.org/https://doi.org/10.5194/bg-18-13-2021, 2021.

Wesely, M.: Parameterization of surface resistances to gaseous dry deposition in regional-scale numerical models, Atmospheric Environment, 23, 1293–1304, https://doi.org/10.1016/0004-6981(89)90153-4, 1989.

Wolf, A., Akshalov, K., Saliendra, N., Johnson, D. A., and Laca, E. A.: Inverse estimation of Vc$_{m}ax$, leaf area index and the Ball-Berry parameter from carbon and energy fluxes, Journal of Geophysical Research, 111, 1–18, https://doi.org/10.1029/2005JD005927, 2006.

Yebra, M., Van Dijk, A., Leuning, R., Huete, A., and Guerschman, J. P.: Evaluation of optical remote sensing to estimate actual evapotranspiration and canopy conductance, Remote Sensing of Environment, 129, 250–261, https://doi.org/10.1016/j.rse.2012.11.004, 2012.

Yienger, J. J. and Levy, H.: Empirical model of global soil-biogenic NOx emissions, Journal of Geophysical Research: Atmospheres, 100, 11 447–11 464, https://doi.org/10.1029/95JD00370, 1995.

Zhang, L., Brook, J. R., and Vet, R.: A revised parameterization for gaseous dry deposition in air-quality models, Atmospheric Chemistry and Physics, 3, 2067–2082, https://doi.org/10.5194/acp-3-2067-2003, URL https://acp.copernicus.org/articles/3/2067/2003/, 2003.

Zhang, L., Jacob, D. J., Knipping, E. M., Kumar, N., Munger, J. W., Carouge, C. C., van Donkelaar, A., Wang, Y. X., and Chen, D.: Nitrogen deposition to the United States: distribution, sources, and processes, Atmospheric Chemistry and Physics, 12, 4539–4554, https://doi.org/10.5194/acp-12-4539-2012, URL https://acp.copernicus.org/articles/12/4539/2012/, 2012.

Zhang, Y., Mathur, R., Bash, J. O., Hogrefe, C., Xing, J., and Roselle, S. J.: Long-term trends in total inorganic nitrogen and sulfur deposition in the US from 1990 to 2010, Atmospheric Chemistry and Physics, 18, 9091–9106, https://doi.org/10.5194/acp-18-9091-2018, URL https://acp.copernicus.org/articles/18/9091/2018/, 2018.

4.9 Appendix

Table 4.A1: Intercept and slope statistics for the GPP-G_c relationship analyzed at the site and ecosystem level grouped following IGBP classification. In addition, the nightly averaged G_c at each site has been appended to the table for comparison.

Ecosystem	Med intercept[a]	Ecosystem intercept[b]	Ecosystem slope[b]	Med night G_c[c]
DBF	0.16 (0.05)	-0.03± 0.02	0.04± 0.01	0.02 (0.04)
ENF	0.1 (0.1)	0.052 ± 0.006	0.037± 0.006	0.01 (0.03)
CRO	0.2 (0.2)	0.20 ± 0.01	0.021± 0.006	0.07 (0.06)
SHR	0.03 (0.09)	0.012 ± 0.002	0.036± 0.004	0.01 (0.02)
GRA	0.1 (0.1)	0.080 ± 0.004	0.038± 0.004	0.03 (0.06)
WET	0.3 (0.2)	0.26 ± 0.01	0.037± 0.008	0.1 (0.2)
all	0.2 (0.2)	0.078 ± 0.002	0.035 ± 0.004	0.02 (0.06)

a. Median intercepts and interquartile ranges (IQR) from G_c-GPP relationship with data at time of TROPOMI overpass.
b. Intercepts and corresponding 95% confidence intervals calculated with all data of a given ecosystem type.
c. Median nighttime G_c during May—August and IQR.

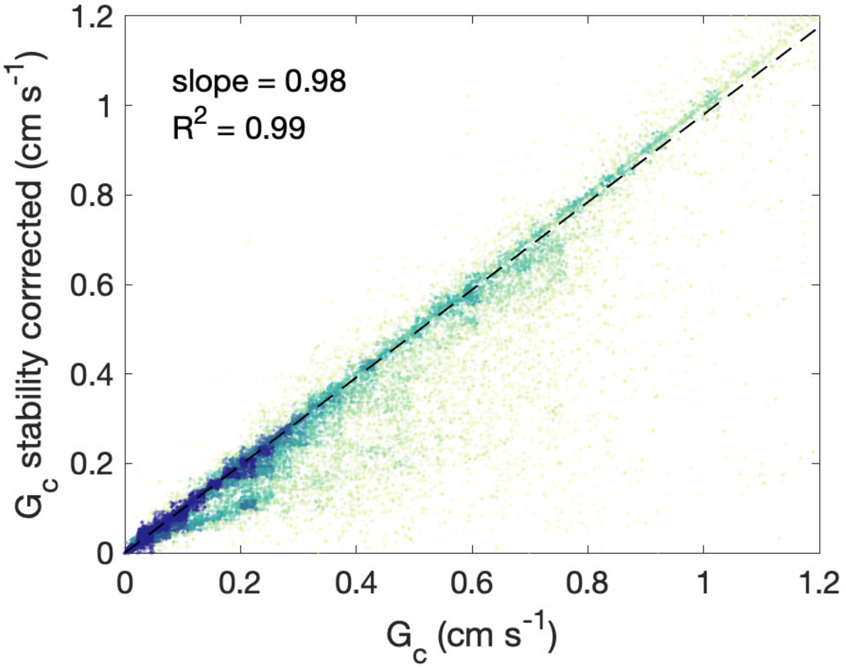

Figure 4.A1: Comparison of G_c values calculated with and without a correction factor for atmospheric stability conditions using measurements from 88 Ameriflux sites.

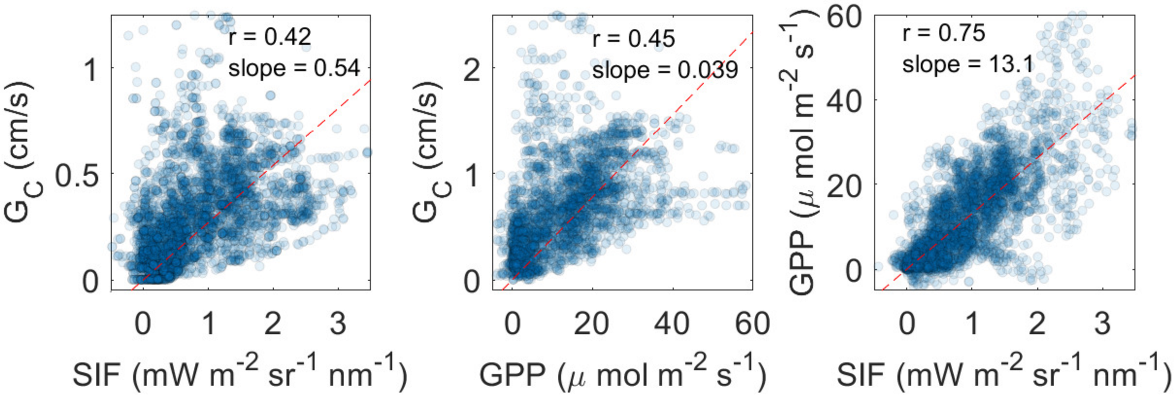

Figure 4.A2: Correlations between SIF and G_c (left), GPP and G_c (middle), and GPP and SIF (right) for all 39 AmeriFlux sites with available data during 2018-2019. Sites consisted of 9 evergreen needleleaf forests, 5 croplands, 8 wetlands, 9 grasslands, 5 shrublands, 2 deciduous broadleaf forests, and 1 mixed forest. The GPP-G_c relationship can be multiplied by the SIF-GPP relationship to obtain the SIF-G_c relationship.

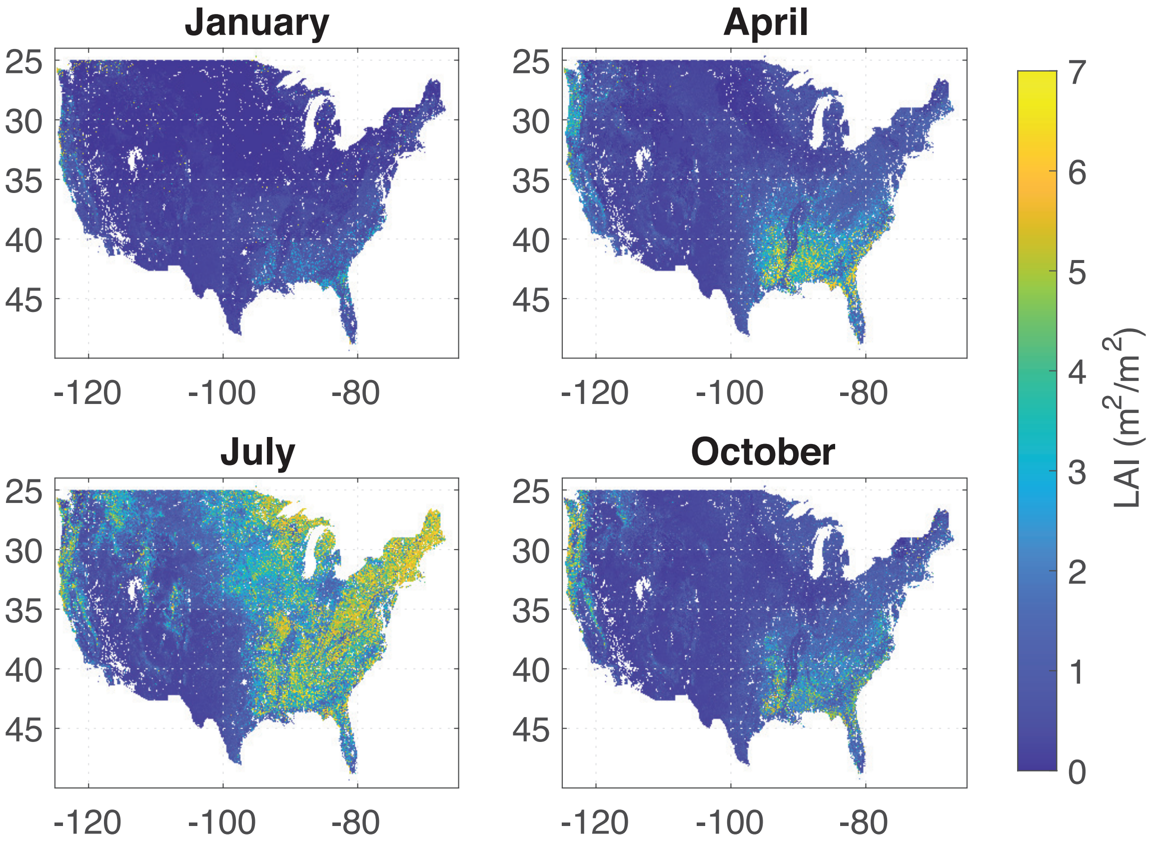

Figure 4.A3: Leaf area index (LAI) data for January, April, July, and October obtained from MCD15A2H Version 6 Moderate Resolution Imaging Spectroradiometer (MODIS) Level 4 product Myneni et al. (2015).

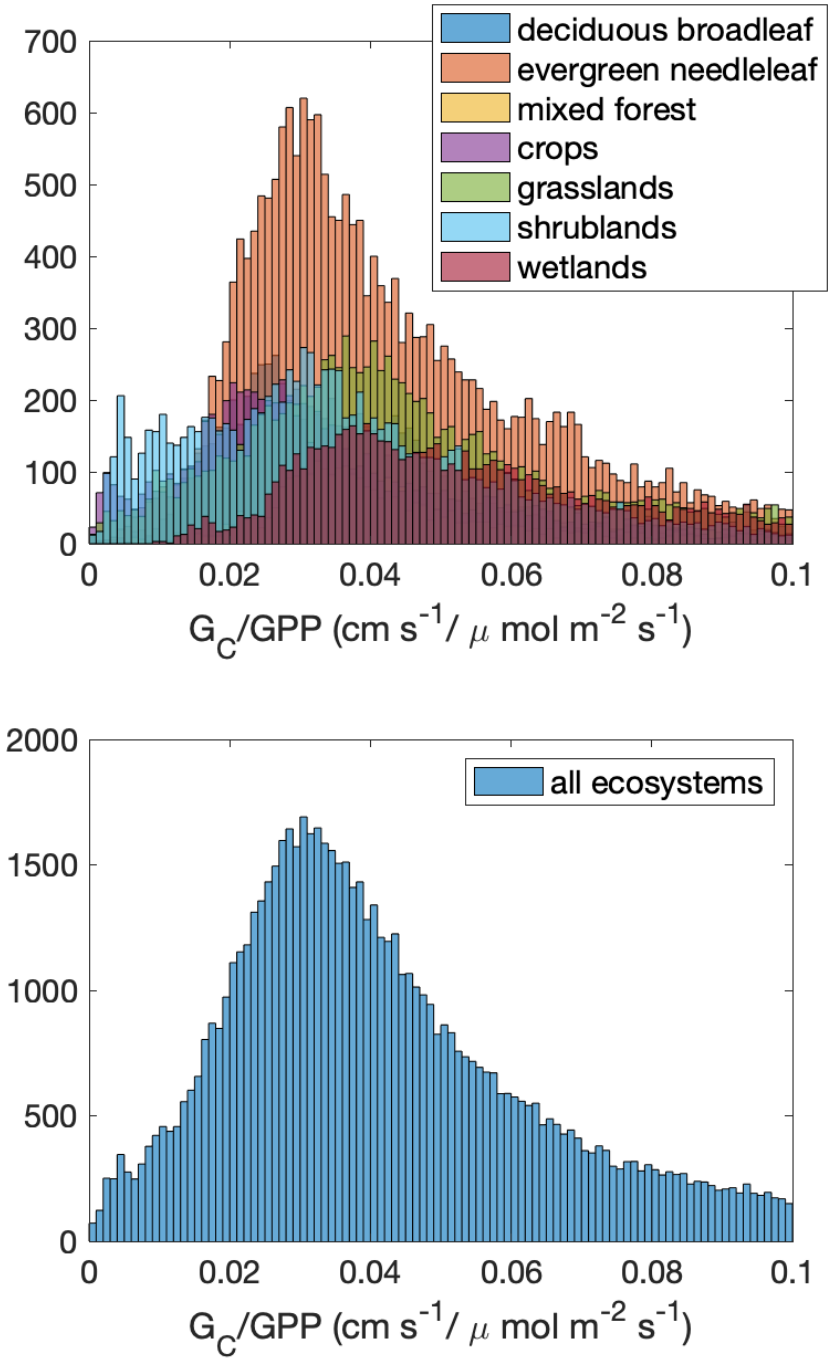

Figure 4.A4: Histogram of the distribution of G_c/GPP ratios by (top) ecosystem type and (bottom) all ecosystems.

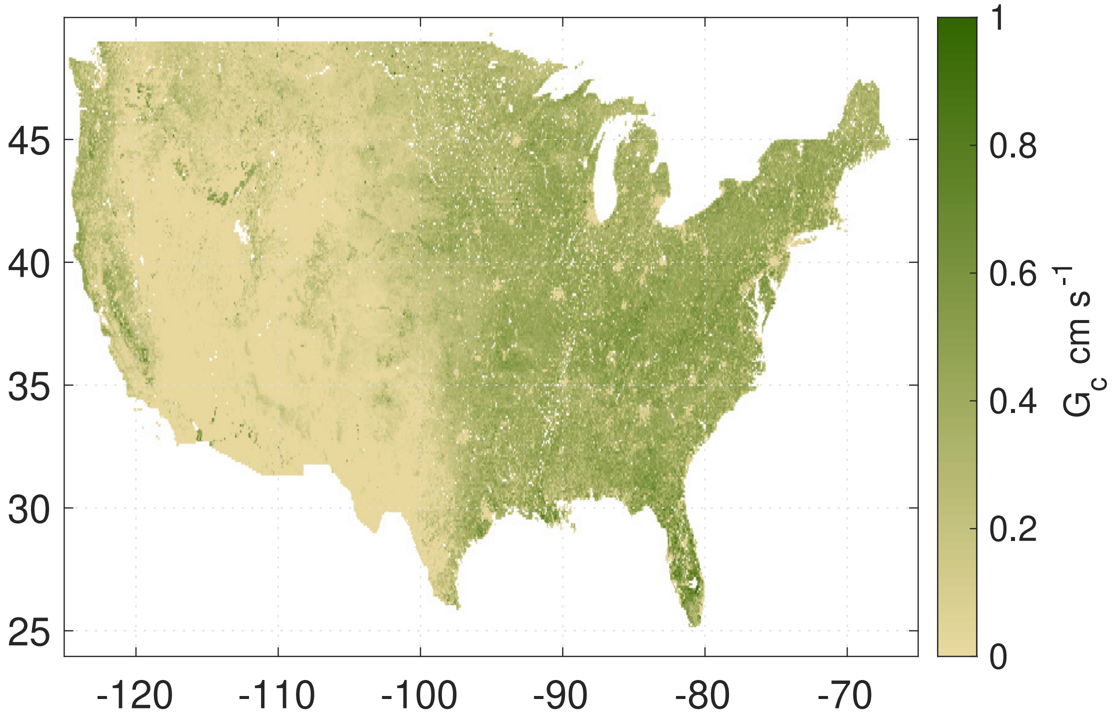

Figure 4.A5: Yearly averaged canopy conductance for 2018 over CONUS at the time of TROPOMI's overpass.

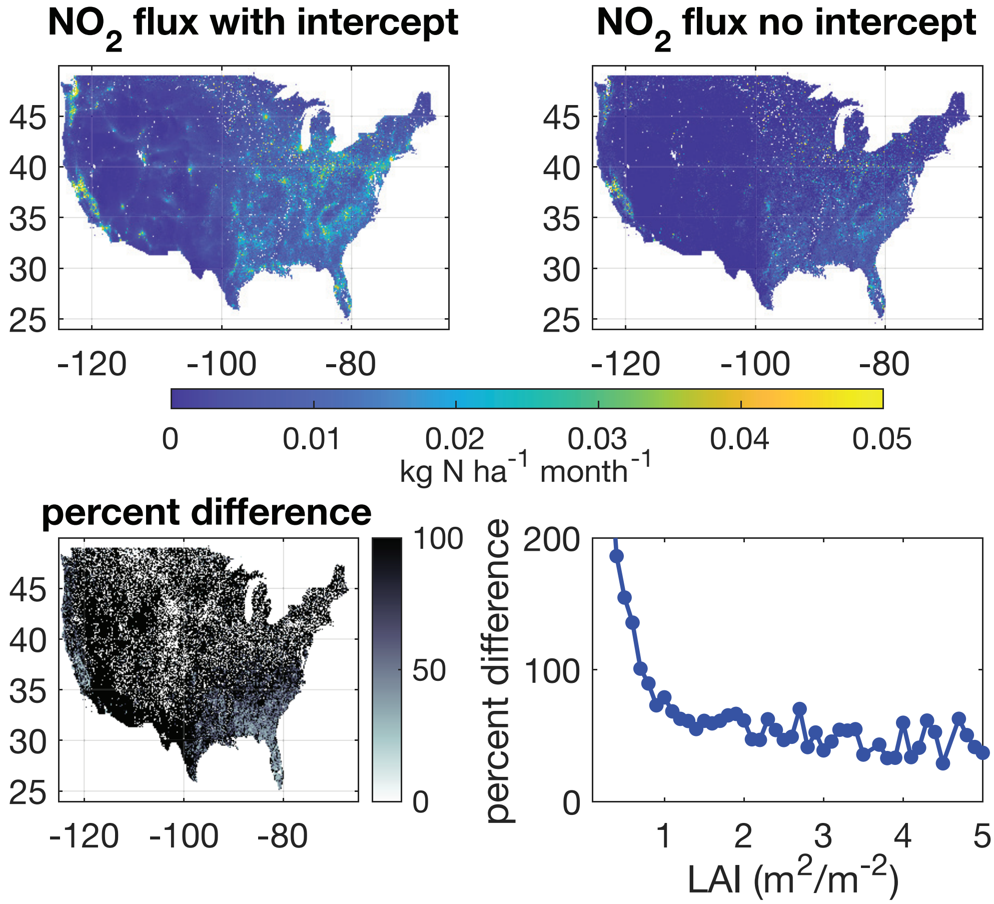

Figure 4.A6: (top) Estimated NO_2 fluxes for January 2018 with and without the use of an intercept in the G_c-SIF model. (bottom) Spatial distribution in the percentage difference between the top panels and percent difference as a function of leaf area index.

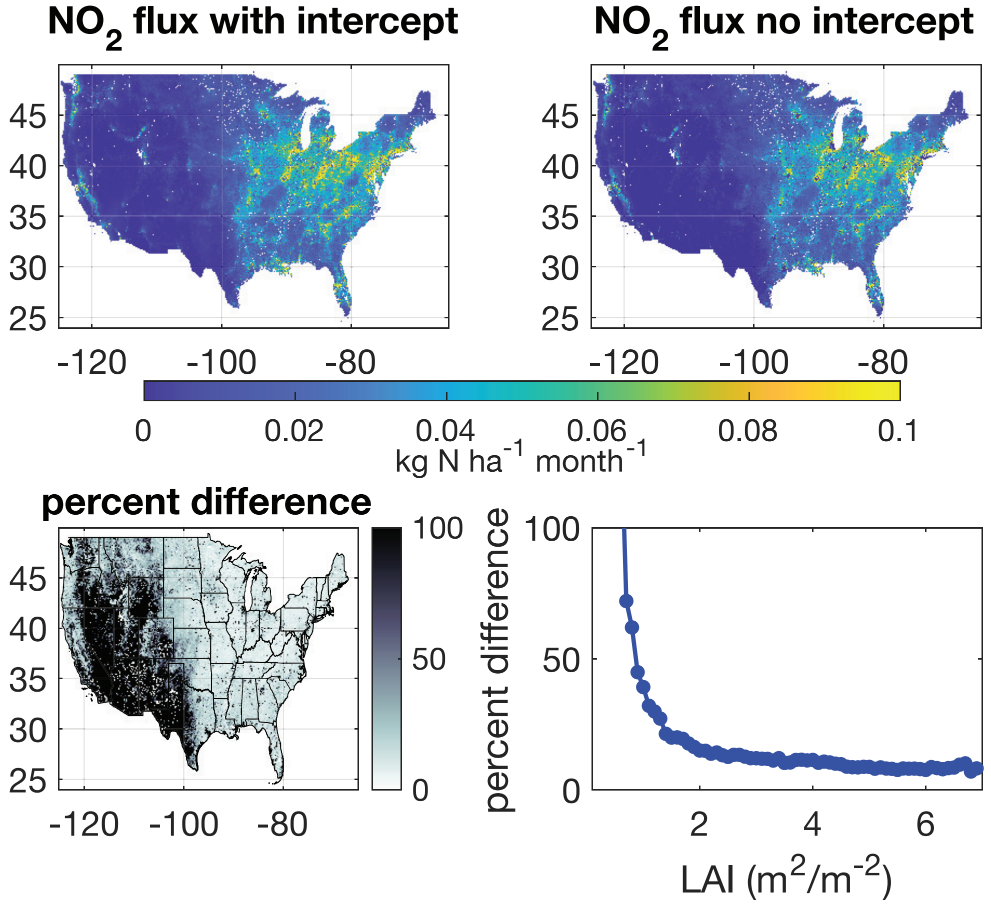

Figure 4.A7: (top) Estimated NO$_2$ fluxes for June 2018 with and without the use of an intercept in the G$_c$-SIF model. (bottom) Spatial distribution in the percentage difference between the top panels and percent difference as a function of leaf area index (bottom).

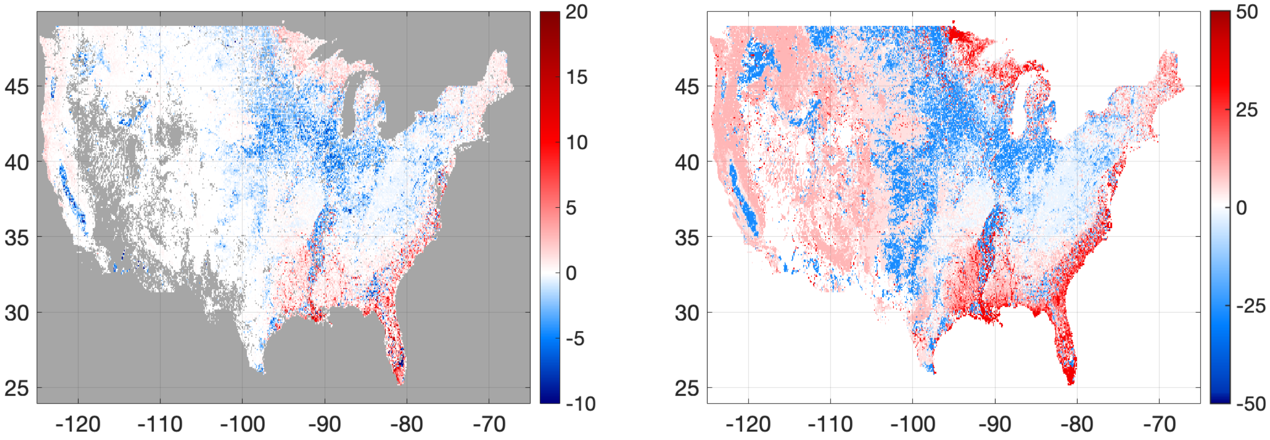

Figure 4.A8: Percent difference in yearly (left) NO_2 fluxes and (right) canopy conductance if ecosystem-specific G_c-GPP slopes are used rather than a uniform slope.

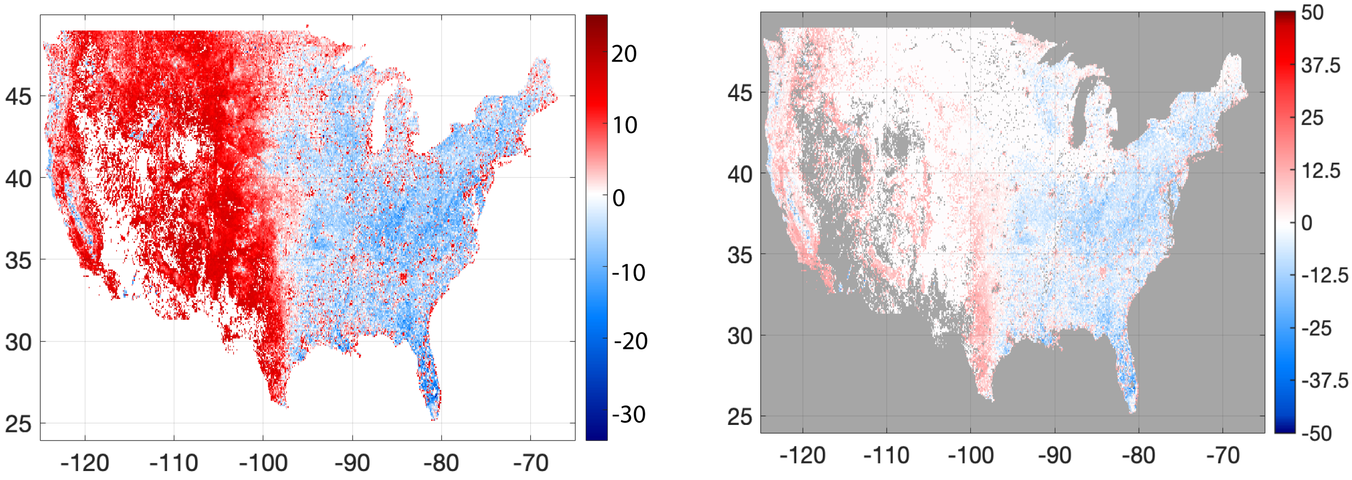

Figure 4.A9: Percent difference in annual (left) canopy conductance and (right) NO_2 fluxes if an exponential fit is used instead of a linear fit

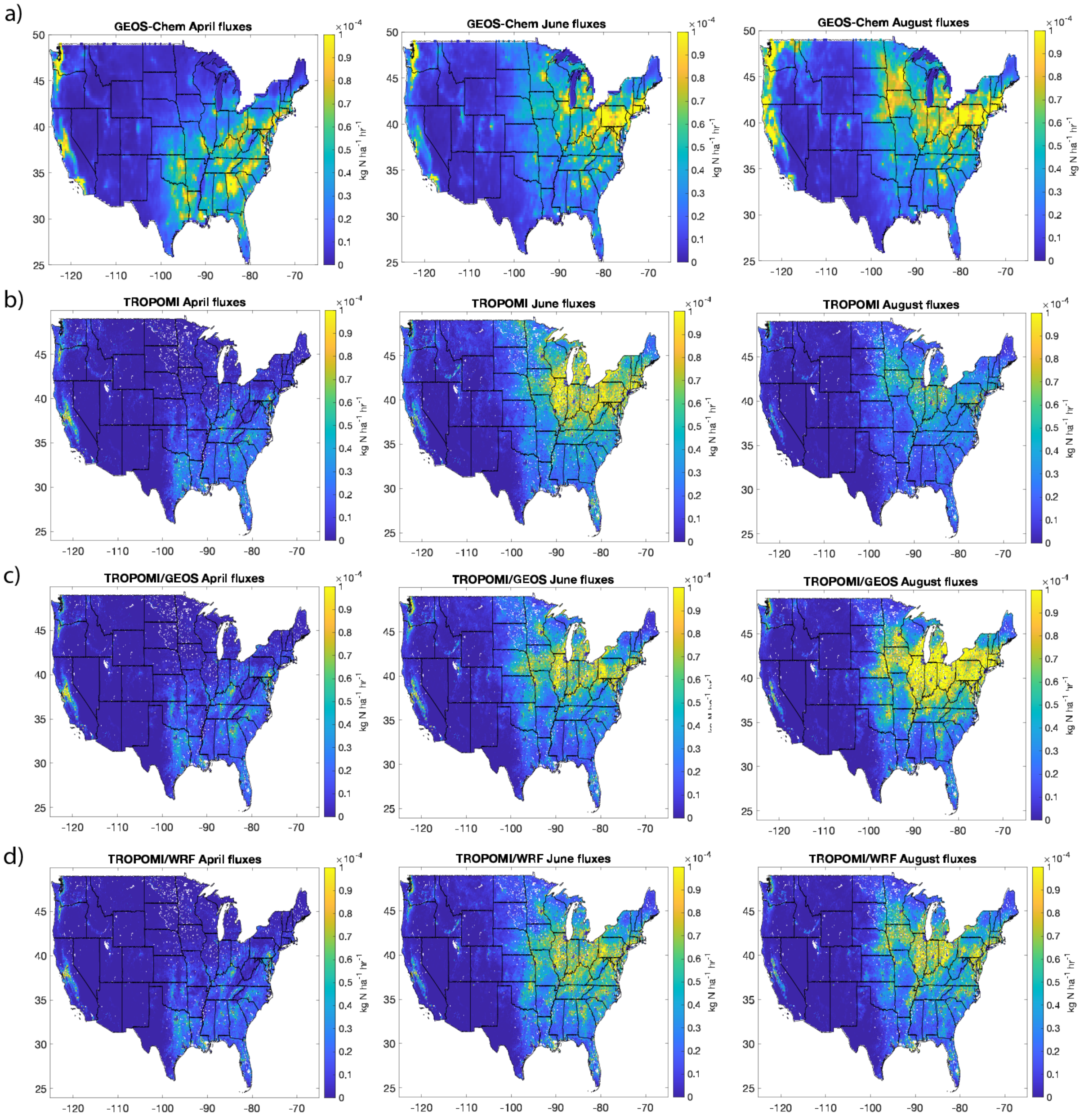

Figure 4.A10: Average 2018 monthly NO_2 fluxes as predicted by (a) GEOS-Chem; (b) using deposition velocities (V_d) and NO_2 from TROPOMI (NO_2 surface concentrations derived from GEOS-Chem profiles); (c) using deposition velocities (V_d) from TROPOMI SIF and NO_2 concentrations from GEOS-Chem; and (d) using deposition velocities (V_d) from TROPOMI SIF and NO_2 concentrations from WRF-Chem.

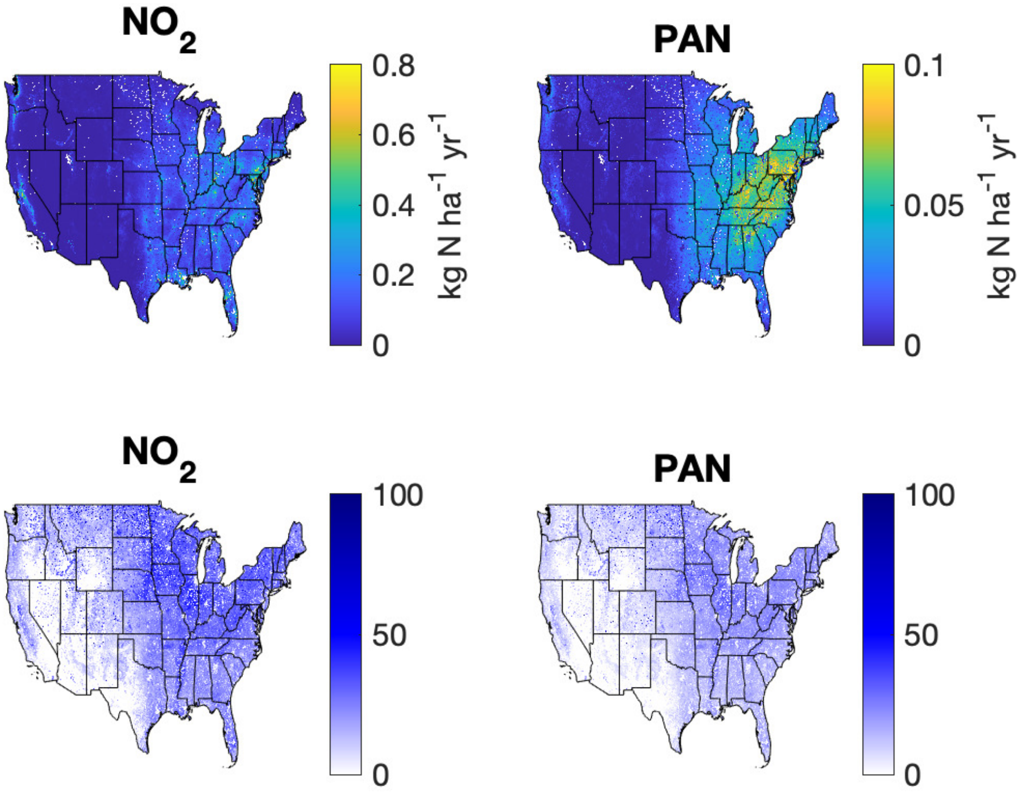

Figure 4.A11: (top) 2018 annual fluxes of NO_2 and PAN considering a uniform aerodynamic resistance (R_a) of 1 s cm^{-1}. (bottom) Percent decrease in annual NO_2 and PAN fluxes with a uniform aerodynamic resistance of 1 s cm^{-1}, compared to no aerodynamic resistance.

Chapter 5

Conclusions

5.1 Summary

Alkyl and multifunctional nitrates ($RONO_2$) and peroxynitrates (RO_2NO_2) modulate the oxidation capacity of the atmosphere through their role in either sequestering or recycling NO_x. The dry deposition of these gases leads to the permanent removal of NO_x from the atmosphere, while the photochemical and thermochemical reactions of these compounds have been shown to regenerate atmospheric NO_x. Greater attention has been devoted to studying the chemical losses of these organic nitrates from the atmosphere with less attention given to their depositional losses. To better understand the role $RONO_2$ and $RONO_2$ deposition plays in the NO_x cycle, laboratory measurements were used to investigate the leaf-level processes driving organic nitrate deposition to vegetation in this dissertation. These laboratory measurements, along with previous measurements of NO_x deposition to vegetation, were then incorporated into a novel regional remote sensing canopy conductance model to study the deposition of RO_2NO_2 and NO_x on a regional scale.

The study presented in chapter 2 elucidated some of the rates and mechanisms that govern RO_2NO_2 deposition to trees. This study showed that RO_2NO_2 deposition proceeded solely through a stomatal pathway, and that the rate of deposition scaled linearly with stomatal diffusion. The measured deposition rates of RO_2NO_2 did not change across the different tree species used in the study. This investigation presented the first controlled measurements of PPN deposition and showed that the stomatal scaling factors of PAN ($\approx$0.7) and PPN ($\approx$1) were different. It was inferred from these scaling factors that PAN deposition was influenced by the mesophyllic uptake rate, while PPN was not. By scaling deposition measurements from this study to represent a forest canopy, it was determined that dry deposition could compete with the thermochemical losses of RO_2NO_2 under colder ambient temperatures.

The first real-time branch-level deposition measurements of $RONO_2$ were presented in chapter 3. These measurements led to the conclusion that $RONO_2$ deposition also proceeded solely through a stomatal pathway. Observations of the stomatal uptake of IPN, MBN and EHN showed that the $RONO_2$ deposition rates were dependent upon the identity of the attached alkyl group. Deposition of all three of these alkyl nitrates was too fast to be described through a dissolution/hydrolysis mechanism, indicating an alternative mode of uptake. It was determined that the depositional loss of these three organic nitrates to vegetation was unlikely to compete with their photochemical losses from the atmosphere.

In chapter 4 a canopy conductance model was used to scale the stomatal deposition rates for RO_2NO_2 and NO_2 (determined from laboratory measurements) to estimate their deposition parameters across the continental USA. The model showed that satellite retrievals of solar-induced fluorescence could be used as a proxy for canopy conductance, and that canopy conductance rates could successfully represent RO_2NO_2 and NO_2 deposition. This was confirmed via the comparison of the newly developed model with commonly used chemical transport models. Finally the model was applied to estimate the lifetime of NO_x and RO_2NO_2 to deposition and indicated that in heavily forested areas, particularly along the coasts, deposition could be a competitive atmospheric loss process.

5.2 Remaining questions

The work presented in this dissertation contributes significantly to the growing body of knowledge surrounding the deposition of nitrogen oxides from the atmosphere. However, there are still many unanswered questions that remain. Recognized below are just a few of these research questions.

1. What are the mechanisms responsible for the mesophylic uptake of $RONO_2$ and RO_2NO_2? The deposition of both of these compounds is too fast to be explained by dissolution/hydrolysis or other proposed reactions (Kames et al., 1990). Are enzymes involved in the internal leaf processing of $RONO_2$ or RO_2NO_2?

2. Are the deposition rates presented in this dissertation generalizable to other tree species as well as crops and herbaceous plants? For example, previous work has shown that the mesophylic processing of RO_2NO_2 was slower in crop leaves than in tree leaves (Sparks et al., 2003). More studies of $RONO_2$ and RO_2NO_2 deposition to a variety of vegetation types are needed.

3. Should solar-induced fluorescence be used as a proxy for canopy conductance in large scale chemical transport models to model nitrogen oxide deposition? Canopy conductance is often parameterized through measurements of temperature, solar radiation and relative humidity, using the SIF-G_c model would greatly simplify model parameterizations (Wesely, 1989). In addition, the model would be able to accurately represent real-time deposition in response to changes in environmental variables within these large scale models.

5.3 References

Kames, J., Schweighoefer, S., and Schurath, U.: Henry's law constant and hydrolysis of peroxyacetyl nitrate (PAN), Journal of Atmospheric Chemistry, 12, 169–180, https://doi.org/10.1007/BF00115778, 1990.

Sparks, J. P., Roberts, J. M., and Monson, R. K.: The uptake of gaseous organic nitrogen by leaves: A significant global nitrogen transfer process, Geophysical Research Letters, 30, https://doi.org/https://doi.org/10.1029/2003GL018578, URL https://agupubs.onlinelibrary.wiley.com/doi/abs/10.1029/2003GL018578, 2003.

Wesely, M.: Parameterization of surface resistances to gaseous dry deposition in regional-scale numerical models, Atmospheric Environment, 23, 1293–1304, https://doi.org/10.1016/0004-6981(89)90153-4, 1989.